

**HOT DEFORMATION BEHAVIOR OF AN Fe-Al ALLOY STEEL
IN THE TWO PHASE REGION**

THE HOT DEFORMATION BEHAVIOR OF AN Fe-Al ALLOY STEEL
IN THE TWO PHASE REGION

By

Kenta Maeda, M. Eng.

A Thesis

Submitted to the School of Graduate Studies

in Partial Fulfillment of the Requirements

for the Degree

Masters of Applied Science

McMaster University

©Copyright by Kenta Maeda, July 2014

Masters of Applied Science (2014)
(Department of Materials Science and Engineering)

McMaster University
Hamilton, Ontario

TITLE: Hot Deformation Behavior of an Fe-Al Alloy Steel in the
Two Phase Region

AUTHOR: Kenta Maeda, M. Eng.

SUPERVISOR: Dr. Hatem S. Zurob

NUMBER OF PAGES: xiv, 116

Abstract

The Thin Slab Cast Direct Rolling (TSCDR) process offers several economic and environmental advantages. The elimination of slab reheating and roughing deformation, however, leave fewer opportunities for grain refinement and some large grains persist in the microstructure. To solve this problem, a new chemistry which leads to a two-phase mixture of ferrite and austenite over a wide temperature range was introduced by Zhou et al. The two phase mixture is highly resistant to grain coarsening leading to a small initial grain size compared with the grain size of conventional TSCDR slab. In addition, ferrite and austenite co-exist over wide range of temperature in many third generation steels, making it extremely important to understand the hot deformation behavior of these materials, which have traditionally received less attention in the literature.

In order to investigate the microstructure evolution of ferrite-austenite mixtures during thermomechanical processing, an Al containing model alloy, for which the two phases co-exist over a wide temperature range, was designed. Two types of experiments were carried out: the first involved single hit hot compression tests; and the second involved stress relaxation tests.

According to the microstructure observation the main change of austenite microstructure under deformation conditions was a decrease in the spacing of the austenite particles within the ferrite matrix. In other words the austenite phase behaved as hard particles inside a soft ferrite matrix. Hot deformation led to the static recrystallization of the ferrite

matrix. The most favourable nucleation sites were in the vicinity of the old grain boundaries and the around austenite particles.

The recovery and recrystallization kinetics of ferrite were analyzed using the stress relaxation test. Based on analysis of the stress relaxation tests, more than 95% of stored energy was consumed by recovery, while static recrystallization consumed less than 5% of the stored energy. The retardation of recrystallization in the model alloy is attributed to both the high rate of recovery in BCC materials and texture effects.

Acknowledgement

This thesis would not have been possible without the hard work and dedication of my supervisor Dr. Hatem S. Zurob. His encouragement, enthusiasm and immense knowledge bank were utilized heavily during this work. He always found time to answer questions or discuss concerns. For everything he has done for me, I will be forever grateful. I was lucky to have him as my supervisor, and cannot image accomplishing as much as I have without him.

A great deal of my experiment results would not have been available without the hard work of the Canmet Materials members, Dr. Fateh Fazeli, Tyler Smith, Marta Aniolek, and Michael Attard. They operated Gleeble[®]3800 system and DIL 805D (TA instrument Inc.).

The lab work would have been impossible without the aid given by Jim Garrett, Dr. Mike Bruhis, Doug Culley, Xiaogang Li, and Ed McCaffery. The SEM and EBSD analysis could not be completed without the kind help provided by Dr. Glynis de Silveria and Chris Butcher. I sincerely appreciate Mark Fraser for proof reading. I have to thank Fumiaki Hiura, and Dr. Yaping Lü for friendship. I surely enjoyed every talk, we have had, academic and non-academic. My thanks also go to the research group of which I am honored to be a part.

I gratefully acknowledge Nippon Steel and Sumitomo Metal Corporation, for providing the chance to study in such a splendid university and for their financial support.

Finally, I sincerely acknowledge my family, especially my wife, Naomi. Without her support and encouragement, I would not be able to complete my project in the foreign country, almost the opposite side of the earth from my home country.

Kenta Maeda

TABLE OF CONTENTS

Abstract	iii
Acknowledgement	v
List of Figures	x
List of Tables	xiv
Chapter 1. Introduction	1
1.1. The Overview of TSCDR Technology of Microalloyed Steels	1
1.1.1. The Thin Slab Casting Direct Rolling Process	1
1.1.2. The metallurgical differences between conventional process and TSCDR...3	
1.2. New Chemistry of Steel	5
1.3. Other Applications	7
1.4. Objective of This Study.....	8
Chapter 2. Literature Review	9
2.1. Relationship among stress, strain, dislocation density and stored energy.....	10
2.1.1. Stored energy of deformation	10
2.1.2. Stress-strain behavior and constitutive equation.....	12
2.2. Recovery.....	15
2.2.1. Mechanism of Recovery	15
2.2.2. Recovery kinetics model.....	17

2.3.	Recrystallization	23
2.3.1.	Mechanisms of Recrystallization	23
2.3.2.	Static recrystallization model	28
2.4.	Experimental Method	32
Chapter 3.	Experimental Work	36
3.1.	Materials	36
3.2.	Single hit deformation test.....	38
3.2.1.	Experimental Set-up.....	38
3.2.2.	Experimental Procedure	39
3.3.	Stress relaxation test.....	40
3.3.1.	Experimental Set-up.....	40
3.3.2.	Experimental Procedure	41
Chapter 4.	Results	43
4.1.	Single hit deformation test.....	43
4.1.1.	Stress-strain behavior	43
4.1.2.	Recovery and subgrain formation	50
4.1.3.	Interaction between Austenite and Ferrite on subgrain formation	57
4.1.4.	Recrystallization microstructure evolution	59
4.1.5.	Recrystallization kinetics	65

4.1.6.	Austenite microstructure evolution.....	67
4.2.	Stress relaxation test.....	69
4.2.1.	Microstructure observation.....	69
4.2.2.	The stress relaxation curves.....	73
4.2.3.	Recovery kinetics.....	78
4.2.4.	Recrystallization kinetics.....	81
Chapter 5.	Discussion.....	84
5.1.	Austenite microstructure evolution.....	84
5.2.	Ferrite Nucleation Mechanism.....	87
5.3.	Ferrite Static Recrystallization Nucleation Kinetics.....	89
5.4.	Ferrite Recovery Kinetics.....	93
5.5.	Ferrite Recrystallization Kinetics.....	96
Chapter 6.	Conclusion.....	104
Chapter 7.	Bibliography.....	107

List of Figures

Chapter 1

Figure 1.1 A typical layout of CSP type thin slab cast direct rolling production mill (Klinkenberg 2005)	1
Figure 1.2 Comparison of temperature evolution between conventional cold and hot charging, and direct charging (Cobo 2001).....	3
Figure 1.3 An example of austenite grains and those size distribution in the as-cast slab (Wang 2005).....	4
Figure 1.4 Grain size evolution after each stand corresponding to a final gauge of (a) 4mm, and (b) 10mm and a rolling start temperature of 1040°C.	5
Figure 1.5 The equilibrium phase diagram of new alloy proposed by Zhou calculated by means of Thermo calc with TCFE6 database (after Zhou 2013)	6
Figure 1.6 As-homogenized microstructure (at 1060°C for 60min)	7

Chapter 2

Figure 2.1 Representatives of stress-strain curves undergoing dynamic recovery and dynamic recrystallization	13
Figure 2.2 Various stages in the recovery of plastically deformed materials (Humphreys 2004).....	17
Figure 2.3 The schematic illustration of SIBM (Humphrey 2004) (a) SIBM of a boundary separating a grain of low stored energy (E_1) from one of higher energy (E_2), (b) dragging of the dislocation structure behind the migrating boundary, (c) the migrating boundary is free from the dislocation structure, (d) SIBM originating at single large grain.....	25

Figure 2.4 Schematic diagram showing the process of substructure formation and annihilation and the start of continuous dynamic recrystallization with deformation at different Z values (Gao 2000).....	28
Figure 2.5 The effect of annealing temperature on recrystallization kinetics of Fe-3.5%Si cold rolled 60% (data from Speich and Fisher 1966) (after Humphrey 2004)	30
Figure 2.6 A typical stress relaxation curve with three distinct stages (after Karjalainen 1996)	33
Figure 2.7 An example of the calculated recrystallized fraction (Karjalainen 1996)	35
<u>Chapter 3</u>	
Figure 3.1 The equilibrium volume fraction of γ as a function of temperature	37
Figure 3.2 The schematic image of machining of cylindrical specimen	38
Figure 3.3 Schematic process diagram for single hit deformation test	39
Figure 3.4 Schematic process diagram for stress relaxation test	41
<u>Chapter 4</u>	
Figure 4.1 Stress Strain Curves in different combination of temperature and strain rate..	44
Figure 4.2 Work hardening ratio during deformation.....	45
Figure 4.3 As-deformed structure in model alloy (at 800°C, $\epsilon=0.6$, $\dot{\epsilon} =10.0s^{-1}$, and 0sec holding time).....	50
Figure 4.4 Microstructure with different imaging method (at 800°C, $\epsilon=0.6$, $\dot{\epsilon} =10.0s^{-1}$, and 0sec holding time.)	52
Figure 4.5 DIC images as a function of Z parameter	53
Figure 4.6 Subgrain size distribution at strain rate of 10.0s-1 in different temperature	55

Figure 4.7 Dependence of subgrain size on flow stress	55
Figure 4.8 Subgrain size change with holding time	56
Figure 4.9 EBSD Band slope images with grain boundaries in different temperature, strain rate, and annealing time. High angle grain boundaries ($15^\circ \leq \theta$) and low angle grain boundaries ($1^\circ \leq \theta < 15^\circ$) are shown in black and red, respectively. (a) was obtained from stress relaxation test.	58
Figure 4.10 Microstructure evolution as a function of deformation temperature and holding time ($\varepsilon = 0.6$, $\dot{\varepsilon} = 10.0s^{-1}$)	60
Figure 4.11 Microstructure evolution as a function of deformation temperature and holding time ($\varepsilon = 0.6$, $\dot{\varepsilon} = 1.0s^{-1}$)	61
Figure 4.12 EBSD orientation maps as a function of deformation temperature and holding time ($\varepsilon = 0.6$, $\dot{\varepsilon} = 10.0s^{-1}$, (i): the Legend of IPF colors)	62
Figure 4.13 Recrystallized grain immediately after deformation at strain rate of $10.0s^{-1}$, and $800^\circ C$	64
Figure 4.14 Recrystallized fraction obtained from image analysis with Avrami fits.	66
Figure 4.15 Volume fraction change of austenite as a function of temperature (deformed condition: strain of 0.6 strain rate of $10.0s^{-1}$)	68
Figure 4.16 Distance change of austenite particles with deformation	69
Figure 4.17 Microstructure after isothermal annealing for low strain rate	71
Figure 4.18 Microstructure after isothermal annealing for high strain rate	72
Figure 4.19 Stress relaxation curves for strain rate of $1.0s^{-1}$	75
Figure 4.20 Stress relaxation curves for strain rate of $10.0s^{-1}$ at low temperature	75

Figure 4.21 Stress relaxation curves for strain rate of $10.0s^{-1}$ at high temperature	76
Figure 4.22 Temperature change by adiabatic heating	76
Figure 4.23 Temperature effect on stress relaxation behavior ($800^{\circ}C$, 0.6, $10.0s^{-1}$)	77
Figure 4.24 The machine effect on stress behavior ($800^{\circ}C$, 0.6, $10.0s^{-1}$).....	77
Figure 4.25 Comparison between experiment and the Verdier's model.....	79
Figure 4.26 Representatives of Verdier and Avrami model	83

Chapter 5

Figure 5.1 Austenite particle radius change as a function of time at different holding temperature (Zhou 2010)	86
Figure 5.2 Schematic illustration of the mechanism of austenite grain growth (Zhou 2010)	86
Figure 5.3 The comparison between the measured intragranular subgrain size and the estimated critical radius	91
Figure 5.4 Relationship among activation volume, temperature, initial flow stress, and strain rate.....	93
Figure 5.5 Recrystallized fraction by means of two different methods.....	97
Figure 5.6 Dependence of 50% recrystallization time $t_{0.5}$ on temperature	98
Figure 5.7 Dependence of Avrami exponent n on temperature	98
Figure 5.8 An example of the stress for the kinetics events during stress relaxation test ($800^{\circ}C$, 0.6, $10.0s^{-1}$)	101
Figure 5.9 Contribution of recovery and recrystallization on restoration during stress relaxation test for different temperature and strain rate.....	102

List of Tables

Chapter 1

Table 1.1 Various TSCDR route (Rodriguez-Ibabe 2007)	2
--	---

Chapter 4

Table 4.1 The calculated values of constants, β , n' , α and n at strain of 0.1-0.6.....	47
Table 4.2 The calculated activation energy of deformation at strain of 0.1-0.6	49
Table 4.3 The logarithmic mean subgrain size change with holding time.....	56
Table 4.4 Recrystallized fraction change of strain rate of $10.0s^{-1}$ as a function of time...	65
Table 4.5 Recrystallized fraction change of strain rate of $1.0s^{-1}$ as a function of time.....	65
Table 4.6 Values of n and $t_{0.5}$ from Figure 4.14	67
Table 4.7 Recrystallized fraction after isothermal annealing.....	73
Table 4.8 Fitted parameters for Recovery	80
Table 4.9 The value of constants employed for Verdier's model	80
Table 4.10 Avrami exponent and 50% recrystallization time form stress relaxation test.	83

Chapter 5

Table 5.1 Comparison of deformation conditions between current work and Smith's work (Smith 2004).....	96
--	----

Chapter 1. Introduction

1.1. The Overview of TSCDR Technology of Microalloyed Steels

The Thin Slab Casting Direct Rolling (TSCDR) Process has become one of the major hot strip production processes in the world due to its economic and environmental advantages. Driven by high market demand for high strength grade steels, a significant effort has been made to develop steels using TSCDR technology.

1.1.1. The Thin Slab Casting Direct Rolling Process

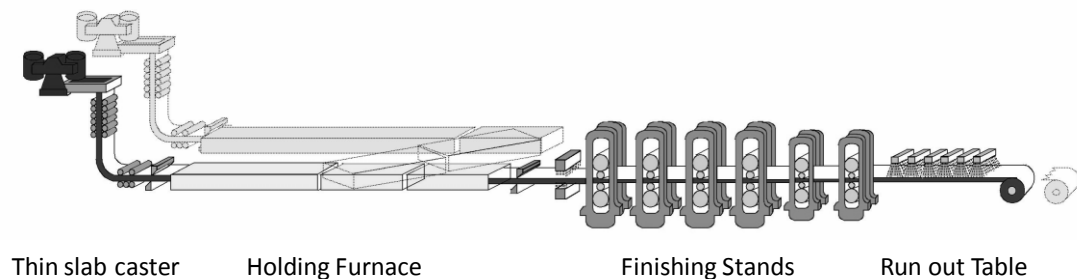


Figure 1.1 A typical layout of CSP type thin slab cast direct rolling production mill (Klinkenberg 2005)

Flat-rolled steel production was revolutionized by the direct linking of a thin-slab caster to a hot-rolling mill (Klinkenberg 2010, Reip 2005). A typical layout of the thin slab cast direct rolling process is shown in [Figure 1.1](#) (Klinkenberg 2005). This process is based on a novel funnel mould caster design that produces a thin slab of thickness of 50-70 mm instead of the conventional slab thickness of 200 to 250 mm. A holding furnace is placed

between the caster and finishing stands to prevent the thin slab from cooling while it grows to the appropriate length to roll. When the slab becomes long enough, the slab enters the finishing stands which consist of four to seven rolling stands and is rolled down to 1 mm-12 mm thickness followed by a laminar cooling section.

The advantages of direct linking include reduced capital, energy, labor and inventory costs (Priestner 1998, Muller 2005), as well as the ability to roll thinner strip compared to the traditional route of thick slab casting, reheating and hot rolling (Rodriguez-Ibabe 2005). Thanks to the economic benefits, the TSCDR process has been developed by many steel productions. Now it has various routes with combination of different technologies. The main characteristics of different TSCDR routes are listed in Table 1.1 (Rodriguez-Ibabe 2007).

Table 1.1 Various TSCDR route (Rodriguez-Ibabe 2007)

Process	Company	Mould type	Thickness (mm)	Furnace	Capacity (Mt/year)	Start-up
CSP	Nucor (USA)	Funnel	50-70	Tunnel	1.8	1989 & 1994
ISP	Arvedi (Italy)	Parallel	60-80	Inductive	0.8	1992
Conroll	Avesta (Sweden)	Parallel	75-125	Pusher type	0.8	1995
QST	Trico (USA)	Parallel	90-105	Tunnel	2.2	1996
ftSC	Algoma (Canada)	Lens-shaped	45-90	Inductive + tunnel	2.0	1997
DSP	Corus (Holland)	Funnel	70	Tunnel	1.3	1999

1.1.2. The metallurgical differences between conventional process and TSCDR

Due to its compact design of process, a TSCDR process offers limited capacity for thermomechanical processing and this introduces new challenges compared with conventional casting and hot rolling processes. The as-cast grain size of a thin slab is approximately $600\mu\text{m}$ (Figure 1.3 (a), Wang 2005) compared with $1000\mu\text{m}$ for thick slabs due to the faster cooling during solidification. Furthermore, the fast solidification rate and post-solidification cooling rate provide smaller segregations and smaller inclusion size than the conventional process. However, during soaking (typically for 30minutes), prior to hot deformation, the initial austenite grains grow to about $2000\mu\text{m}$ (Pottore 1999). Due to the elimination of the slab cooling and reheating cycle, the microstructure does not experience ferrite-austenite (during reheating) phase transformations, so that grain size cannot be refined prior to hot rolling (Figure 1.2, Cobo 2001).

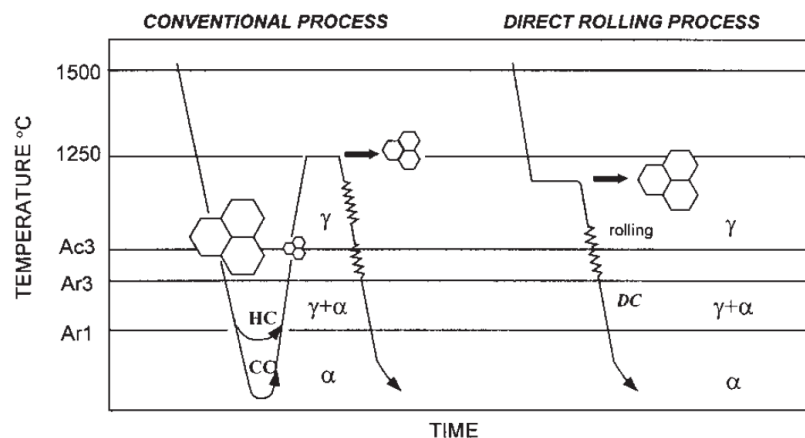
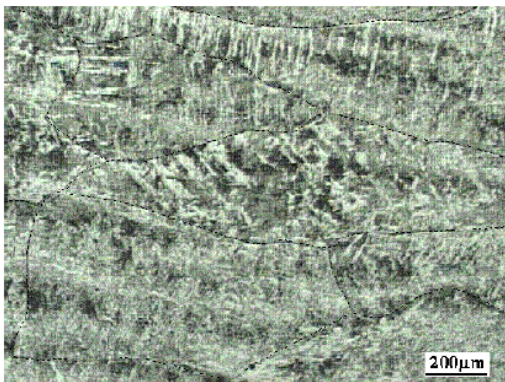
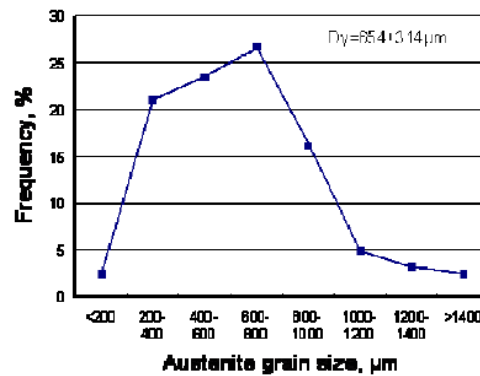


Figure 1.2 Comparison of temperature evolution between conventional cold and hot charging, and direct charging (Cobo 2001)

This large grain size imposes the necessity for heavy grain refinement during hot-rolling. However, due to the thin slab thickness, the maximum available total reduction is only 3.0, while it is about 10 for the conventional process. The large initial grain size combined with the small deformation reduction during thermomechanical processing result in a mixed-grain size and non-uniform microstructure as shown in [Figure 1.3 \(b\)](#) (Wang 2005).



a) Austenite grains at the quarter position



b) Austenite grain size distribution

Figure 1.3 An example of austenite grains and those size distribution in the as-cast slab (Wang 2005).

Uranga et al. examined the microstructure evolution by means of simulation of hot rolling (Uranga 2005). Hot deformation was carried out for 6 passes for two final thicknesses of 4mm and 10mm. The grain size was measured after inter-pass-time for each pass. The heterogeneity of the grain size was evaluated in terms of the parameter, ZD , which represents D_{max}/D_{mean} . According to [Figure 1.4](#), while the mean grain size decreased with

each deformation pass, the *ZD* parameter remained essentially constant meaning that the material inherits the heterogeneity of the as-cast microstructure.

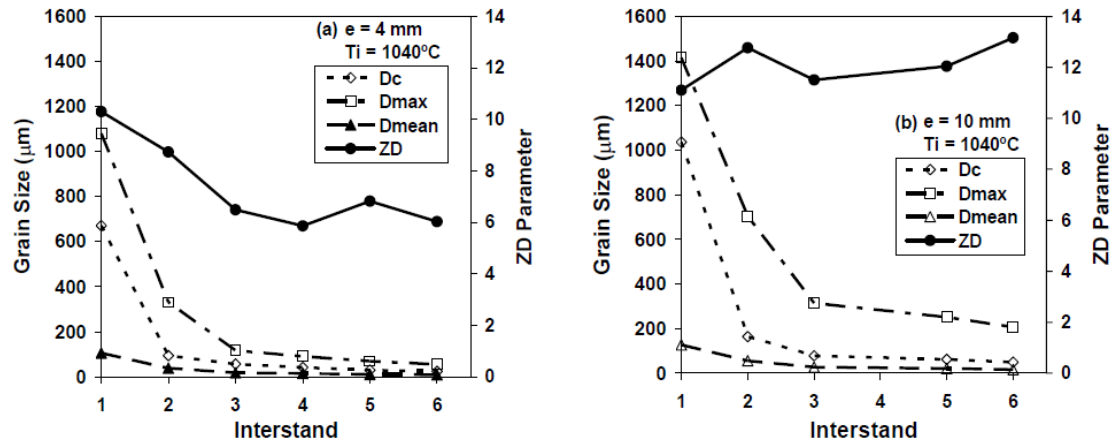


Figure 1.4 Grain size evolution after each stand corresponding to a final gauge of (a) 4mm, and (b) 10mm and a rolling start temperature of 1040°C.

It is widely accepted that the presence of large isolated grains, even in small volume fractions, is enough to impair the toughness and ductile brittle transition temperature of the steel, making it difficult to produce high grade steel by the TSCDR process.

1.2. New Chemistry of Steel

These large grains present prior to the thermomechanical processing for TSCDR were attributed to excessive grain growth that takes place prior to the onset of thermomechanical processing (Zhou 2010a, 2010b, 2011, 2013). Several methods have

been proposed to minimize grain-growth at high temperature and produce more favorable microstructures. The majority of these involve the precipitation of high temperature nitrides or the use of oxide dispersions to pin grain-growth at high temperatures (Gao 1998, Nagata 2002, Wang 2005, Suito 2006, Sha 2009). A different approach was proposed by Zhou et al (Zhou 2013), in which, the steel chemistry was modified in order to expand the temperature range over which the delta-ferrite and austenite phases co-exist (Figure 1.5). A wide range of chemistries could be used to generate a phase diagram of the type shown in Figure 1.5. As an example, Zhou et al. proposed a steel with a composition of Fe, 0.05wt% C, 1.5wt% Al, 1.0wt% Mn, and 0.4wt% Si (Zhou 2010).

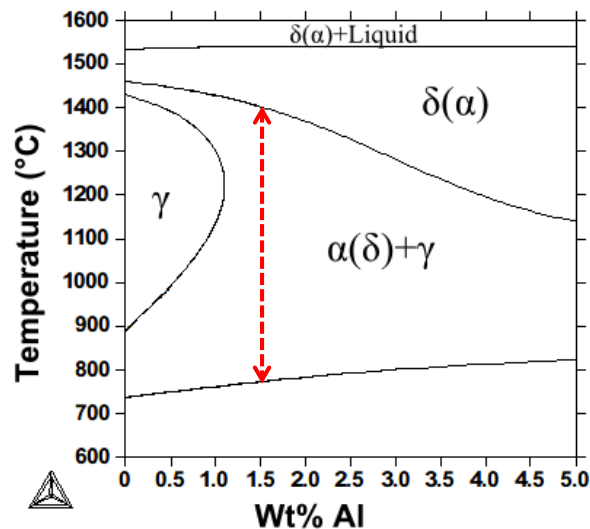


Figure 1.5 The equilibrium phase diagram of new alloy proposed by Zhou calculated by means of Thermo calc with TCFE6 database (after Zhou 2013)

Zhou et al studied the evolution of microstructures of the type shown in Figure 1.6 at temperatures up to $\sim 1300^{\circ}\text{C}$ (Zhou 2013). The minor phase (austenite) was found to

coarsen at a very slow rate which is controlled by the bulk diffusion of substitutional elements in the parent phase. Grain-growth within the predominant phase (delta-ferrite) was pinned by the minor phase (austenite). It was demonstrated that the new chemistry successfully prevented the development of excessively large grains during cooling from the caster to the tunnel furnace as well as during soaking within the tunnel furnace.

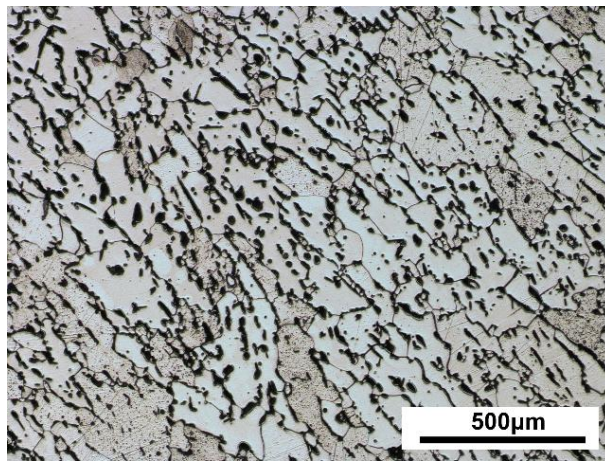


Figure 1.6 As-homogenized microstructure (at 1060°C for 60min)

However, the potential for grain refinement of this model alloy during hot deformation has not been investigated. The microstructure evolution and kinetics of this model alloy need to be investigated in order to design suitable hot rolling processes.

1.3. Other Applications

Low alloy steels which exhibit a wide ferrite/austenite co-existence region are potentially important for many applications besides TSCDR. In fact, ferrite and austenite co-exist

over wide range of temperatures in many third generation steels, making it extremely important to understand the hot deformation behavior of these materials. For example, a similar chemical composition is found in several new TRIP (transformation induced plasticity) steels (De Meyer 1999, Jacques 2001, Samek 2006, Aretxabaleta 2012). While conventional TRIP steel contains Fe, 0.2wt% C, 1.5wt% Mn, 1.5wt% Si, 1.2-1.5wt% Aluminum is substituted for Silicon in the new type of TRIP steel in order to improve galvanizing quality and ductility. Though the phase transformation and mechanical properties of those steels were extensively investigated, the kinetics of microstructure evolution during thermomechanical processing in these steels received less attention.

1.4. Objective of This Study

The final objective of this study is to clarify the optimum hot rolling schedule of the model alloy, which consists of a two-phase mixture of ferrite and austenite over a wide range of temperatures. In order to achieve this goal, the kinetics of microstructure evolution during hot deformation in the model alloy must be characterized. With this in mind, this thesis has focused on the microstructure evolution and its kinetics during single hit compression and following annealing assuming a single hot deformation stand and following inter-pass time. Hence, specific aspects of microstructural evolution were studied in detail: the microstructure change of austenite; the microstructure evolution of ferrite; and interaction between ferrite and austenite.

Chapter 2. Literature Review

The mechanical performance of a metal is a function of its microstructure. Phase transformation and thermomechanical processing have been used to produce steels with a wide range of microstructures and mechanical properties leading to a large number of applications in various fields of industry, such as, construction, automotive, and electrical appliances.

When a metal is plastically deformed, the majority of applied energy is dissipated as heat. A small fraction of the applied energy, on the order of a few percent, is stored in the material in terms of defects, such as vacancies and dislocations. This accumulated energy is called the stored energy of deformation. The deformed material can lower its energy by eliminating the defects created during deformation. This process is called restoration and it includes recovery, recrystallization and grain growth. Restoration processes are accelerated at high temperature due to the increased mobility of atoms. During hot deformation, the generation and storage of defects due to plastic deformation is partially offset by the rearrangement and annihilation of defects by dynamic restoration processes which take place while the material is being deformed as well as static restoration processes which take place after the end of deformation. In order to control the microstructure, it is crucial to identify the operating restoration mechanisms and quantify their kinetics.

The present project is focused on the microstructure evolution of hot deformed steel containing 1.5wt% Al. Under thermomechanical processing conditions, this steel has two

phases, ferrite and austenite. The first focus of this literature review is the deformed microstructure and stored energy developed during hot deformation (section 2.1). Secondly, recovery and its kinetics during and after hot deformation will be discussed in section 2.2. Furthermore, section 2.3 will cover recrystallization and its kinetics during and after deformation. Finally, section 2.4 will discuss experimental method to investigate recovery and recrystallization kinetics.

2.1. Relationship among stress, strain, dislocation density and stored energy

2.1.1. Stored energy of deformation

As mentioned above, most of the work applied during plastic deformation is dissipated as heat and a limited amount of energy is stored in the material as defects. The defects generated by plastic deformation include vacancies, interstitial atoms and dislocations. Generally, the mobility of point defects is relatively high, so that their contribution to the stored energy is low. Therefore, it is thought that the generation and accumulation of dislocations is the major form of stored energy.

The relationship between plastic deformation and dislocation motion is described in terms of the equation:

$$\varepsilon = \rho \mathbf{b} \bar{L} \quad (2.1)$$

where ε , ρ , \mathbf{b} , and \bar{L} are plastic strain, dislocation density, Burgers vector, and the mean distance of dislocation movement during hot deformation, respectively.

In polycrystalline materials, a dislocation generated within a grain moves inside the grain leading to plastic deformation. However, since dislocations cannot move across the grain boundaries, the dislocations must be accommodated at the grain boundaries. Furthermore, dislocations in the same grain interact and trap each other, so that the accumulation of dislocation is promoted. When the dislocation density is high, a higher stress is required for dislocation movement leading to the concept of work hardening. The relationship between dislocation density and flow stress is expressed as

$$\sigma = \sigma_0 + c_1 G b \sqrt{\rho} \quad (2.2)$$

where G is shear modulus and σ_0 is friction stress, c_1 is a constant of the order of 0.5 (Bailey 1960).

Next, one needs to estimate the stored energy due to the accumulation of dislocation during plastic deformation. Assuming isotropic elasticity, the energy per unit length of dislocation line can be described using the expression:

$$E_{dis} = c_2 G b^2 \quad (2.3)$$

where c_2 is constant of the order of 0.5. For a material containing a dislocation density ρ , the stored energy E_D can be given by (Humphreys 2004):

$$E_D = \rho E_{dis} = c_2 \rho G b^2 \quad (2.4)$$

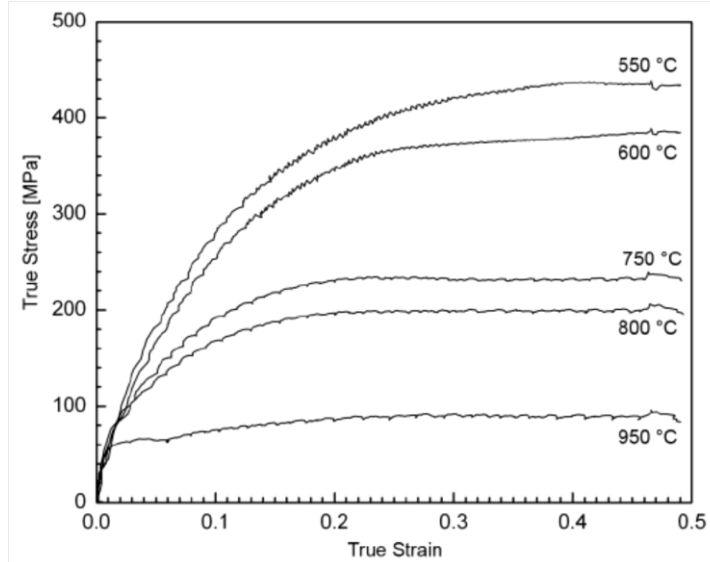
This becomes the driving force for recovery and recrystallization.

2.1.2. Stress-strain behavior and constitutive equation

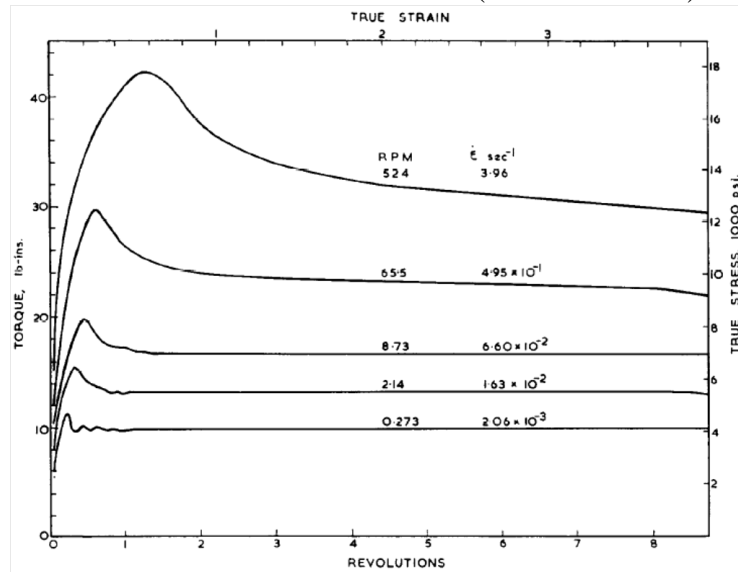
Due to the increased atomic mobility at high temperature, the restoration processes, such as recovery and recrystallization can occur during high temperature deformation. To emphasize the occurrence of recovery and recrystallization during deformation, the term “dynamic recovery” and “dynamic recrystallization” are used, respectively (Humphreys 2004). When dynamic recovery and dynamic recrystallization occur, the stress-strain curves show a saturation of stress or a decrease in stress with increasing strain. The typical shapes of the curves are shown in [Figure 2.1](#).

In the case of dynamic recovery, during the initial stage of deformation, the flow stress increases with the generation and storage of dislocations. As the dislocation density rises, the driving force of recovery increases and hence, recovery is promoted. At certain strain, the work hardening rate and recovery reach dynamic equilibrium. The value of stress in this dynamic equilibrium state is called the steady-state flow stress (Mehtonen 2013).

The stress-strain curve for dynamic recrystallization is characterized by the broad peak at a certain strain. Under low strain rate or high temperature conditions, multiple peaks may be observed at lower strains. As dynamic recrystallization and dislocation formation reach dynamic equilibrium, the stress-strain curve shows a steady state behavior (Luton 1969). Generally, in materials with low stacking fault energy, such as copper and austenitic steel, dynamic recrystallization may take place because climb and cross-slip of dislocations are retarded by the dissociation of dislocations.



(a) A representative dynamic recovery type stress-strain curve, 21wt% Cr ferritic stainless steel (Mehtonen 2013)



(b) A representative dynamic recrystallization type stress-strain curve, Pure Nickel deformed at 934 °C (Luton 1969)

Figure 2.1 Representatives of stress-strain curves undergoing dynamic recovery and dynamic recrystallization

Extensive works concerned with flow behavior in various materials has been carried out. It was revealed that the steady-state stress in the dynamic recovery type material and the peak stress in dynamically recrystallizing materials depend on the strain rate, and deformation temperature (Jonas 1969). The relation among temperature, strain rate, and flow stress can be expressed by equations (2.5) – (2.7), which are known as the hyperbolic sine law, power law, and exponential law, respectively.

$$\dot{\epsilon} = A [\sinh(\alpha\sigma)]^n \quad (2.5)$$

$$\dot{\epsilon} = A' \sigma^{n'} \quad (2.6)$$

$$\dot{\epsilon} = A'' \exp(\beta\sigma) \quad (2.7)$$

In these equations, A , A' , A'' , n , n' , α , and β are material constants. The Relationship among α , β , and n' can be expressed as:

$$\alpha \approx \frac{\beta}{n'} \quad (2.8)$$

Zener and Hollomon proposed the Zener-Hollomon Parameter (Z) (Zener 1944), which is a temperature compensated strain rate, defined as:

$$Z = \dot{\epsilon} \exp\left(\frac{U_{def}}{RT}\right) \quad (2.9)$$

where $\dot{\epsilon}$, T , R and U_{def} are the strain rate, the deformation temperature in Kelvin, the gas constant and the apparent activation energy of deformation, respectively, (Mehtonen 2013). The constitutive equation describing the flow stress in terms of strain rate and temperature can be expressed by using this parameter. Thus, the relation among

temperature, strain rate, and flow stress can be expressed by equation (2.10) - (2.12) which resemble equations (2.1) - (2.3).

$$Z = A [\sinh(\alpha\sigma)]^n \exp\left(-\frac{U_{def}}{RT}\right) \quad (2.10)$$

$$Z = A' \sigma^{n'} \exp\left(-\frac{U_{def}}{RT}\right) \quad (2.11)$$

$$\dot{\epsilon} = A'' \exp(\beta\sigma) \exp\left(-\frac{U_{def}}{RT}\right) \quad (2.12)$$

Many authors have worked on determining the values of the constants and apparent activation energy U_{def} in the above equations. The U_{def} values for ferritic steel given by other researchers in literature are scattered, i.e. 397kJ/mol for 21wt%Cr ferritic stainless steel (Mehtonen 2013), 375kJ/mol for AISI430 (0.0018wt%C, 16.65wt%Cr) in dual phase region (Hinton 2007), 372kJ/mol for Ti added interstitial steel in ferritic region, 334kJ/mol for Fe-2.8wt%Si alloy (Uvira 1968), and Fe-1.8wt%Al (Ouchi 1983). In high purity iron, the activation energy was reported as 280kJ/mol in the ferritic region (Glover 1973).

2.2. Recovery

2.2.1. Mechanism of Recovery

Recovery refers to the reduction of the stored energy in the deformed material by rearrangement and annihilation of dislocations. When a material which was deformed at room temperature is annealed, recovery occurs at relatively low temperature prior to

recrystallization. A schematic illustration of the recovery process is shown in Figure 2.2 (Humphrey 2004). Dislocations generated and tangled during deformation (Figure 2.2 (a)) form a cell structure (Figure 2.2 (b)). During annealing, dislocations within cells disappeared by annihilation. Lower energy configurations are formed through the rearrangement of dislocations (Figure 2.2 (c)). Subgrains are gradually formed as the misorientations between cells increase due to the accumulation of dislocations (Figure 2.2 (d)). Following subgrain formation, subgrains grow with time (Figure 2.2 (e)). Generally, recovery takes place continuously during plastic deformation.

During hot deformation, the rate of dynamic recovery increases because dislocation motion is thermally activated. Recovery processes are controlled by either glide, cross-slip, or climb of dislocations (Nes 1995). In low stacking fault energy material such as copper, silver and austenitic stainless steel, little recovery occurs prior to recrystallization because cross-slip and climb are difficult. On the other hand, in high stacking fault energy materials, such as aluminum and ferritic iron, significant recovery would occur because of rapid cross-slip and climb (Humphreys 2004, Jonas 1969).

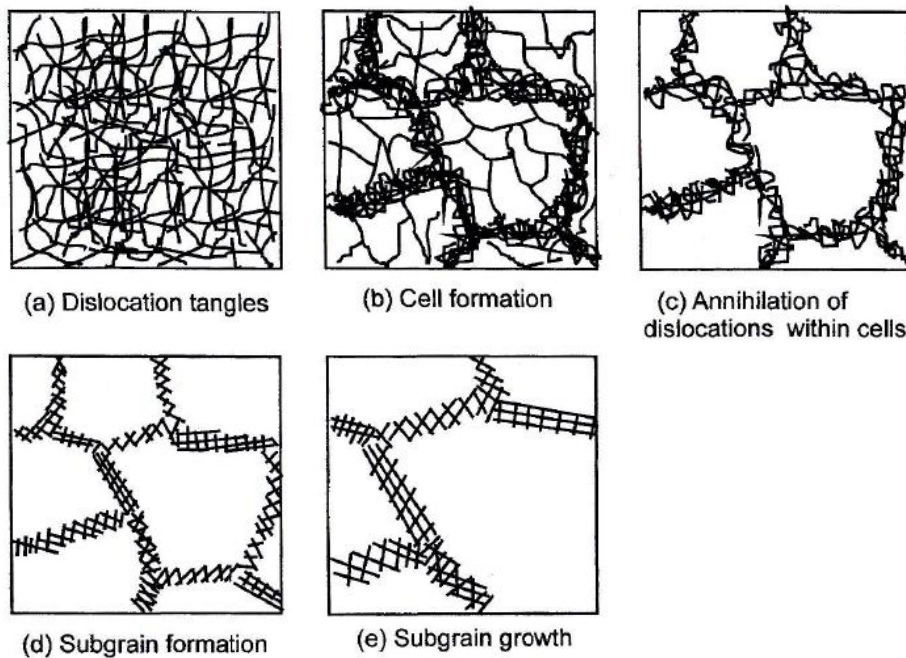


Figure 2.2 Various stages in the recovery of plastically deformed materials (Humphreys 2004)

2.2.2. Recovery kinetics model

Recovery kinetics has been studied by the changes in a parameter such as, heat evolution, resistivity, X-ray diffraction, flow stress, and hardness. Several different empirical relationships between fraction of recovery f_{RCV} and time t have been proposed to describe experimental results. The simplest approach to express recovery behavior is as follows:

$$\frac{df_{RCV}}{dt} = -\frac{A}{t} \quad (2.13)$$

where A is a constant. The integration of this equation leads to

$$f_{RCV} = B - A \ln t \quad (2.14)$$

where A and B are constant. This type of kinetic law is called a logarithmic or hyperbolic law. This relationship can be applied to a limited time range, because at early stages of recovery ($t \rightarrow 0$), f_{RCV} must be finite and must be zero at the end of recovery ($t \rightarrow \infty$) (Humphrey 2004, Byrne 1965)

Recovery is accomplished by the annihilation and rearrangement of dislocations. Since dislocation motion is controlled by glide, climb and cross-slip, in order to formulate a model for the physical based recovery behavior instead of an empirical relationship, it is necessary to clarify the mechanisms of recovery and their contributions. Extensive works have been conducted to establish physical based recovery models by many researchers (Friedel 1964, Nes 1995, Kuhlmann-Wilsdorf 2000, Humphreys and Hatherly 2004, Verdier 1999). There are two dominant classes of physical based recovery models exemplified by those of Verdier et al., and Nes et al. The first class of model initially suggested by Friedel, (Friedel 1964), and then developed by Verdier et al. (Verdier 1999) is based on the relaxation of internal stress as a result of the annihilation and reorganization of dislocations. In the stress relaxation process, the total strain ε_{total} can be described as the sum of elastic strain ε_e , and plastic strain ε_p .

$$\varepsilon_{total} = \varepsilon_e + \varepsilon_p = const. \quad (2.15)$$

Differentiation of equation (2.15) with respect to time leads to:

$$\frac{d\varepsilon_e}{dt} + \frac{d\varepsilon_p}{dt} = 0 \quad (2.16)$$

The elastic strain can be expressed as a function of the flow stress as:

$$\varepsilon_e = E\sigma \quad (2.17)$$

Substituting equation (2.17) into equation (2.16) leads to:

$$\frac{1}{E} \frac{d\sigma}{dt} + \frac{d\varepsilon_p}{dt} = 0 \quad (2.18)$$

The plastic strain change with time can be expressed as a function of dislocation density through the Orowan law:

$$\frac{d\varepsilon_p}{dt} = \frac{1}{M} \mathbf{b} \rho \bar{V} \quad (2.19)$$

where M is the Taylor factor, \mathbf{b} is the Burgers vector, ρ is the dislocation density and \bar{V} is the mean dislocation velocity. Assuming that the dislocation motion is thermally activated and the activation energy decreases with the internal stress, the mean dislocation velocity can be described as:

$$\bar{V} = v_D \mathbf{b} \exp\left(\frac{U_0 - \sigma v_a}{kT}\right) \quad (2.20)$$

where v_D is the Debye frequency, the value of which is the order of 1.0×10^{13} for steel, k is the Boltzmann constant, U_0 is the intrinsic activation energy, which is similar in value to the self diffusion activation energy, and v_a is the activation volume of the recovery process. Activation volume can be expressed as (Nes, 1998):

$$v_a = l_a \mathbf{b}^2 \quad (2.21)$$

where l_a is an activation length. The activation length is approximately equal to the special arrangement of the obstacles which control the rate of dislocation motion, for instance, the spacing of forest dislocations or jogs, or the spacing between solute atoms.

Thus, equation (2.19) can be expressed as:

$$\frac{d\varepsilon_p}{dt} = \frac{\rho \mathbf{b}^2 v_D}{M} \exp\left(-\frac{U_0}{kT}\right) \sinh\left(\frac{\sigma v_a}{kT}\right) \quad (2.22)$$

Substituting equation (2.22) into equation (2.18) results in the expression:

$$\frac{d\sigma}{dt} = -\frac{E\rho \mathbf{b}^2 v_D}{M} \exp\left(-\frac{U_0}{kT}\right) \sinh\left(\frac{\sigma v_a}{kT}\right) \quad (2.23)$$

Using the Taylor relation, a relationship between flow stress and dislocation density can be formulated as

$$\sigma_i = \alpha M G \mathbf{b} \sqrt{\rho} \quad (2.24)$$

where $\sigma_i = \sigma_y - \sigma_{y0}$, the quantities σ_y , and σ_{y0} are, respectively, the measured yield strength after isothermal annealing, and the yield stress of the after fully recovered microstructure. α is a constant that depends on the material, of the order of 0.2, and G is the elastic shear modulus, $G = 3/8 E$. By combining equation (2.23) and equation (2.24), the stress relaxation rate is obtained as:

$$\frac{d\sigma_i}{dt} = -\frac{64}{9M^3 \alpha^2} \frac{\sigma_i^2}{E} v_D \exp\left(-\frac{U_0}{kT}\right) \sinh\left(\frac{\sigma_i v_a}{kT}\right) \quad (2.25)$$

Using U_0 and v_a as fitting parameters, the model provided accurate agreement with experimental results of recovery softening of Al-Mg (Verdier 1999), 0.2wt%C, 1.5wt%Mn steel (Smith 2004), and cold rolled low carbon steel (Martinez-de-Guerenu 2004).

The second approach is established based on the evolution of two microstructural parameters, the average cell/subgrain size, $\delta(t)$, and dislocation density $\rho(t)$ (Nes 1995).

The equation is described as follows.

$$\sigma(t) = \sigma_0 + \alpha_1 M G b \sqrt{\rho(t)} + \alpha_2 M G b \frac{1}{\delta(t)} \quad (2.26)$$

where σ_0 is frictional stress, and α_1 and α_2 are constants the values of which are in the range of 0.3-0.5 and 2-3, respectively. This model was developed to correspond well to the recovery behavior of high purity ferritic iron, pure aluminum, and Al-Mg alloy (Nes 1995).

Nes' model provides an accurate description of recovery behavior, though the model is complex because additional assumptions and additional adjustable parameters are needed to distinguish the effect of flow stress evolution due to dislocation density and subgrain growth in experimental results. On the other hand, the advantage of Verdier's model is that it shows sufficient agreement with a wide variation of experimental conditions using only two fitting parameters, the activation energy and activation volume (Verdier 1997, Martínez-de-Guerenu 2004, Smith 2004).

To the best of the author's knowledge, the literature on recovery behavior of ferritic steel is very limited compared with that on the recrystallization behavior. Mukunthan and Howbolt (1996), Martínez -de-Guerenu et al. (2004), and Smith et al. (2004) carried out detailed studies on the recovery behavior of ferritic steel. Mukunthan and Howbolt investigated recovery kinetics of Ti-Nb stabilized interstitial free (IF) steel during isothermal annealing following 80% cold rolling by means of in-situ X-ray peak resolution measurements. The hyperbolic law was employed to describe recovery behavior. The relationship between the X-ray peak ratio, R_I , and time, t , were described as:

$$R_I = b - a \ln t \quad (2.27)$$

Recovery was studied at annealing temperatures of 500°C and 550°C in their work. They reported that the apparent activation energy of recovery increases with the progress of recovery. The range of apparent activation energy was from 173.1kJ/mol in the initial state to 312.1kJ/mol after isothermal annealing (Mukunthan 1996).

Martinez-de-Guerenu et al. studied recovery kinetics of low carbon steel in the low temperature region (300°C to 500°C) by means of in-situ coercive field measurement. The coercive field, H_c , is proportional to dislocation density, ρ , as $H_c \propto a\sqrt{\rho}$, where a is constant. Hence, the fraction of recovery, R_y , has been defined as:

$$1 - R_y = \frac{H_c}{H_c^{def}} \quad (2.28)$$

where H_c^{def} is the coercive field of the deformed state. Verdier's model was applied to express recovery kinetics. They reported the range of activation energy was from $29b^3$ for high stress condition to $36b^3$ for low stress conditions (Martínez -de-Guerenu 2004).

The recovery kinetics in the ferritic region of 0.2wt%C, 1.5wt%Mn steel were investigated in various combination of temperature, strain and strain rate by means of stress relaxation test by Smith et al (Smith 2004). Detail of stress relaxation will be discussed in section 2.1.6. Activation energy and activation volume were determined by fitting Verdier's model to experimental results. The ranges of activation energy and activation volume were reported, respectively, as 217kJ/mol to 236kJ/mol and $1.6 \times 10^{-28} m^3$ ($10.5b^3$) to $2.7 \times 10^{-28} m^3$ ($17.7b^3$).

Studies focused on the recovery behavior of steels were carried out at relatively low temperatures, approximately from 300°C to 600°C because of occurrence of ferrite-austenite transformation. Few studies have focused on the recovery behavior of ferritic steels which have experienced hot deformation in the high temperature region (700°C to 1000°C).

2.3. Recrystallization

2.3.1. Mechanisms of Recrystallization

Recrystallization refers to the process in which high angle grain boundaries (HAGB) migrate into the deformed or recovered structure and leave behind a region with lower dislocation content. The recrystallized grains can be distinguished from the deformed

matrix, and the recrystallized fraction can often be calculated from optical images. Generally, the kinetics of recrystallization is sigmoidal. An incubation time is observed during recrystallization, meaning that there is a delay between the end of deformation and the onset of recrystallization. As nucleation and growth begin, the recrystallization rate increases. A decrease in the recrystallization rate is observed during the late stages of recrystallization due to the impingement of the neighboring recrystallized grains (Humphreys 2004).

The nucleation of static recrystallization is thought to have three mechanisms. The first is the classical nucleation and growth, which, in this context, refers to the formation, within the deformed material, of a new dislocation free grain surrounded by a HAGB. This mechanism is thought to take place in the vicinity of grain boundaries, and second phase particles and within deformation bands (e.g. shear bands, and mechanical twin boundaries).

The next mechanism is the strain induced grain boundary migration (SIBM), which is the bulging of a part of pre-existed HAGB. SIBM occurs when there is a significant difference in stored energy across the grain boundary. A schematic illustration of SIBM is shown in [Figure 2.3](#). HAGB bulges out from one grain to another with growth of single or multiple subgrains. The new grains by SIBM have similar orientations to the old grains from which they bulged. SIBM is observed under low strain conditions where conventional nucleation of recrystallization is less likely to occur (Humphreys 2004, Leslie 1981).

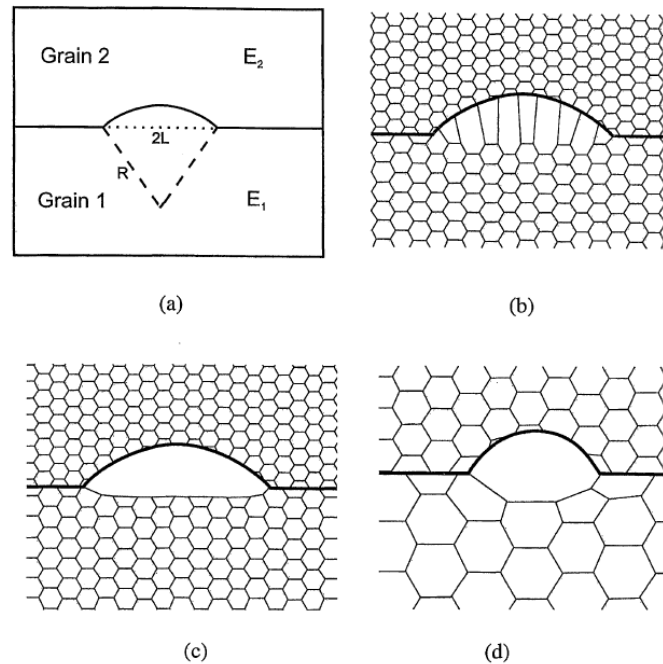


Figure 2.3 The schematic illustration of SIBM (Humphrey 2004)

(a) SIBM of a boundary separating a grain of low stored energy (E_1) from one of higher energy (E_2), (b) dragging of the dislocation structure behind the migrating boundary, (c) the migrating boundary is free from the dislocation structure, (d) SIBM originating at single large grain.

The third recrystallization nucleation mechanism is the coalescence of subgrains (Hu 1962, Li 1962). Two adjacent subgrains rotate during annealing. When the orientation of the two grains becomes the same, the subgrain boundary between them is eliminated. Repeated coalescence events eventually lead to the formation of a high angle grain boundary and the nucleation of recrystallization. The first two of these recrystallization mechanisms are similar because they are both caused by boundary migration. For iron, many research results indicate that the migration of pre-existing grain boundaries is the most common mechanism to generate new strain-free grains (Leslie 1981).

As for dynamic recrystallization, three mechanisms are discussed in the literature: discontinuous dynamic recrystallization (DDRX), continuous dynamic recrystallization (CDRX) and geometric dynamic recrystallization (GDRX) (Gourdet 2000, Humphreys 2004). Discontinuous dynamic recrystallization has been considered to occur only in low stacking fault energy materials, such as copper, and austenitic iron. In high stacking fault energy materials, such as aluminum and ferritic iron, much of the stored energy is lost due to recovery which is promoted by cross-slip or climb during deformation, so that discontinuous dynamic recrystallization has been regarded not to occur. However, thanks to extensive efforts, the dynamic recrystallization of high stacking fault energy materials has been observed to take place at very large strains. Yamagata et al. confirmed the occurrence of dynamic recrystallization in high purity aluminum by means of in-situ X-ray diffraction analysis (Yamagata, 1992a, 1992b, 1992c, 1994). Dynamic recrystallization of high purity α -iron was characterized, by Glover and Sellars, by means of high temperature torsion tests where oscillation behavior in stress-strain curves and a substructure containing dynamically recrystallized grains were observed (Glover 1973).

Discontinuous dynamic recrystallization (DDRX) is similar to static recrystallization, in that it consists of nucleation and grain growth. New grains of DCRX start nucleation at the old grain boundaries when the applied strain is above a critical strain. In the case of dynamic recrystallization, the dislocation density in the new grains increases due to ongoing deformation and the driving pressure for grain growth of new grains decreases. Therefore, dynamic recrystallized grains stop growing. If more deformation is applied, the further new grains recrystallize at the grain boundaries of former recrystallized grains.

Tsuji et al. shows the evidence of occurrence of DDRX in interstitial free steel in the high temperature range (873-1123K) by means of TEM (transmission electron microscope) Kikuchi line analysis and SEM (scanning electron microscopy) EBSD (electron backscattered diffraction) analysis. The results suggest that the deformation conditions of lower Zener-Hollomon (Z) parameter and higher strain are more favorable for DDRX in ferrite (Tsuji 1997, 1998a).

Continuous dynamic recrystallization (CDRX) and geometric dynamic recrystallization (GDRX) are variants of the same general mechanism. GDRX requires a very high strain level, e.g. $\epsilon > 3.0$ for high purity Aluminum, where the old grains are mechanically broken into new grains during deformation (Kassner 1989). On the other hand, CDRX is initiated by dislocation accumulation in subgrain boundaries, and occurs at a somewhat lower strain level ($\epsilon \sim 0.8$). The schematic illustration of CDRX proposed by Gao et al (Gao 2000) is shown in [Figure 2.4](#). In high strain rate and low temperature condition, subgrains cannot easily form, and consequently, CDRX does not occur. With decreases of the Z parameter, subgrain boundary and HAGB were formed accompany with dislocation accumulation. Occurrence of CDRX has been characterized by the evolution of the fraction of HAGB and low angle grain boundary (LAGB) with strain by some authors (Schmidt 1981, Gourdet 2000, Mehtonen 2013), but other authors suggest that the increase of HAGBs is attributed to GDRX. Therefore, the mechanism of CDRX is still controversial (Gourdet 2000).

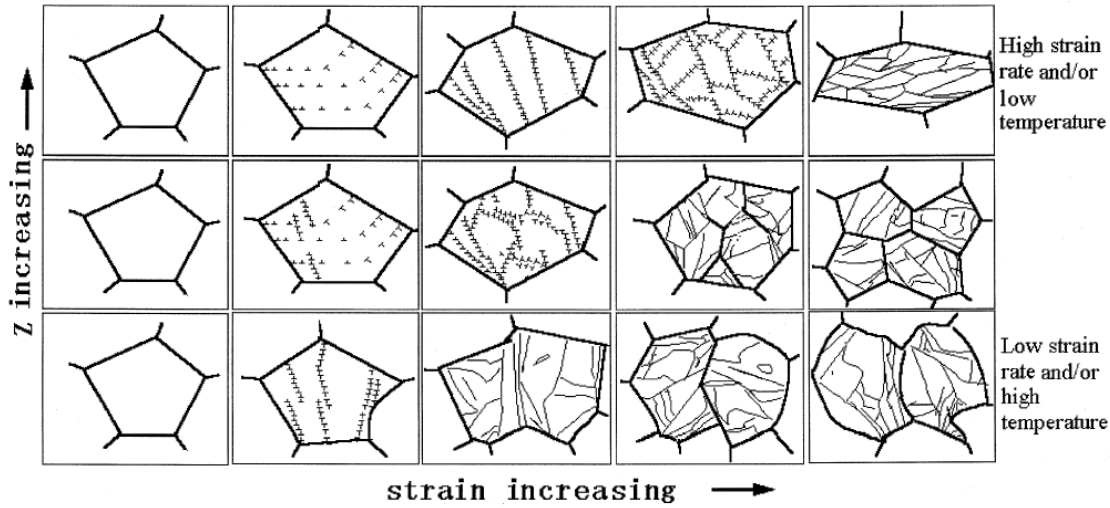


Figure 2.4 Schematic diagram showing the process of substructure formation and annihilation and the start of continuous dynamic recrystallization with deformation at different Z values (Gao 2000)

2.3.2. Static recrystallization model

The model which is most widely accepted to describe the evolution of recrystallization fraction f_{REX} is the Johnson-Mehl-Avrami-Kolomogorov (JMAK) model. While the JMAK model was originally established to describe phase transformation, Burke and Turnbull applied it to recrystallization (Burke 1952). The driving force for recrystallization is the stored energy in the deformed metal, and its kinetics is the function of the nucleation rate \dot{N} , and the growth rate \dot{G} . When it is assumed that nucleation rate is constant, and growth rate is constant and isotropic, the recrystallized fraction can be formulated as:

$$f_{REX} = 1 - \exp(-Bt^n) \quad (2.29)$$

Where t is annealing time, the exponent n is referred to the Avrami exponent with the value of 4, and the constant B is described as:

$$B = \frac{\pi}{4} \dot{N} \dot{G}^3 \quad (2.30)$$

In the limiting case when all nuclei are activated at an initial stage of recrystallization, the number of nucleation site N is employed instead of the nucleation rate \dot{N} , and B in equation (2.29) is given by

$$B = \frac{3\pi}{4} N \dot{G}^3 \quad (2.31)$$

In this case, the Avrami exponent n is 3. This is termed site saturation. The value of the Avrami exponent is in the range between 3 and 4 for a general decreasing nucleation rate (Humphrey 2004).

However, Avrami exponent larger than 3 is rarely observed. Experimentally, a typical value of Avrami exponent is approximately 2 and in some case even less than 1. This is due to the stiff and the idealized assumptions of the JMAK theory. Most cases of real materials have a non-uniform growth rate or inhomogeneous nucleation site distribution (Karjalainen 1995, 1996, Perttula, 1998, Luo 2004).

Due to the difficulty of verification of the nucleation rate and the growth rate from the experiment, the Avrami type empirical equation is also widely employed to recrystallization kinetics (Laasraoui 1991, Karjalainen 1996, Maccagno 1996, Luo 2004).

The recrystallized fraction can be formulated as:

$$f_{REX} = 1 - \exp \left\{ -\ln(1-F) \cdot \left(\frac{t}{t_F} \right)^n \right\} \quad (2.32)$$

where F is the fractional measure of interest, t_F is the time reaching the fractional measure of interest, and n is the Avrami exponent, once again. Usually, $F=0.5$, so that t_F becomes $t_{0.5}$, and the time for 50% recrystallization. Hence, equation (2.32) can be expressed as:

$$f_{REX} = 1 - \exp \left\{ -0.693 \cdot \left(\frac{t}{t_{0.5}} \right)^n \right\} \quad (2.33)$$

As shown in [Figure 2.5](#) (a), the recrystallization kinetics is influenced by the annealing temperature.

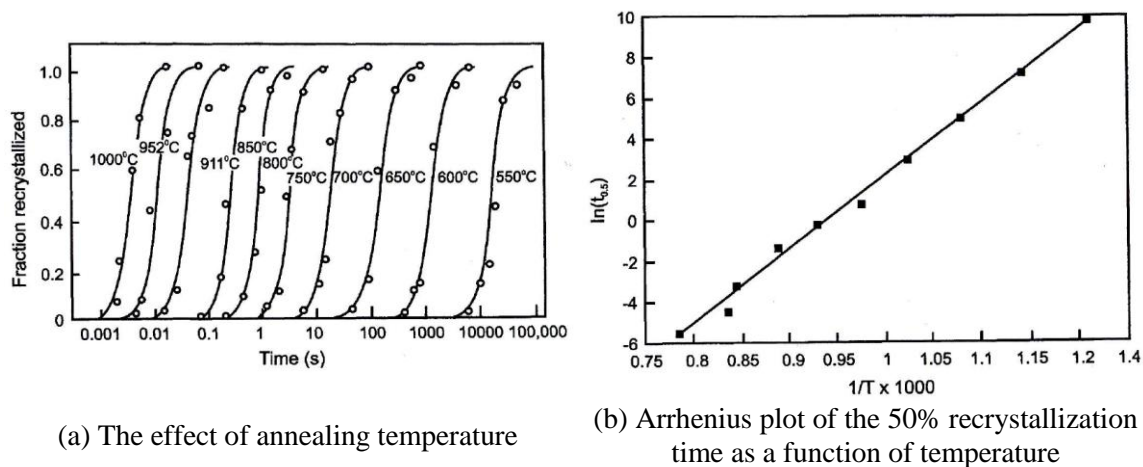


Figure 2.5 The effect of annealing temperature on recrystallization kinetics of Fe-3.5%Si cold rolled 60% (data from Speich and Fisher 1966) (after Humphrey 2004)

The relationship the between 50% recrystallization time and temperature can be formulated as (Humphrey 2004):

$$t_{0.5} = K \exp\left(\frac{U_{REX}}{RT}\right) \quad (2.34)$$

Where K is constant, R is the gas constant, T is temperature, and U_{REX} is the apparent activation energy of recrystallization. The apparent activation energy U_{REX} can be obtained from the Arrhenius plot of $\ln(t_{0.5})$ vs. $1/T$. In the case of [Figure 2.5 \(b\)](#), the value of apparent activation energy is 290kJ/mol (Humphreys 2004).

The recrystallization kinetics in hot deformed and isothermally annealed metals are influenced not only by temperature, but also other conditions of hot deformation, such as strain, initial grain diameter, and the Z parameter. The empirical relationship between hot deformation conditions and recrystallization kinetics were determined as the pre-exponent term K by many authors (Sellars 1979, Li 1996, Humphreys 2004). The pre-exponent term can be expressed as:

$$K = AD_0^\zeta \varepsilon^{-\xi} Z^{-\zeta} \quad (2.35)$$

Where D_0 is initial grain diameter, ε is strain, Z is the Zener-Hollomon parameter, and A , ζ , ξ , and ζ are constants.

The value of apparent activation energy of recrystallization in various steels has been reported as 280kJ/mol for pure iron in ferrite region (Glover 1973), 272-300kJ/mol for C-Mn Steel in austenite region (Sellars 1980), 252kJ/mol for low C steel in austenite region, and 221kJ/mol for 21wt% Cr stainless steel (Mehtonen 2013).

2.4. Experimental Method

There are many options of experimental method to investigate restoration behavior during isothermal annealing after hot deformation. Observation of the microstructure in quenched materials by means of optical microscopy, SEM, or EBSD are the most direct ways to determine the recrystallized fraction of the material. In carbon steels, however, it is difficult to distinguish the recrystallized grain from the phase transformed grains due to the austenite-ferrite phase transformation. Additionally, the observation area is too narrow in micrographs, especially in SEM or TEM to determine the softening kinetics in whole specimens. Hence, it is time-consuming to cover a wide area in a specimen.

The interrupted double hit compression (or twist in torsion) test is widely employed by many authors to evaluate the restored fraction in a material quantitatively (Laasraoui 1991, Roucoules 1994, Li 1996, Yanagida 2008). In this method, the measured softening fraction includes effects of both recovery and recrystallization, and it is difficult to distinguish these two effects. Furthermore, the experiment must be repeated with various interval times to obtain the whole restoration curve by means of this method. Therefore, this method is still time-consuming.

Liu and Jonas demonstrated the occurrence of precipitation in austenite by means of stress relaxation test (Liu 1988). The research group of Karjalainen demonstrated the feasibility and efficiency of the stress relaxation test for modeling the kinetics of recrystallization in hot deformed steel (Karjalainen 1995, 1996, Perttula 1998). They found three distinct stages in the true stress vs. log time curves. In the first stage, stress

decreases logarithmically due to recovery, so that stress follows equation (2.14). In the second stage, stress drops rapidly. This is attributed to recrystallization. Finally, the stress once again becomes logarithmic, suggesting that recrystallization is completed, and recovery (or creep) becomes the dominant softening process again.

An example of a stress relaxation curve in carbon steel by Karjalainen and Perttula is shown in [Figure 2.6](#) (Karjalainen 1996).

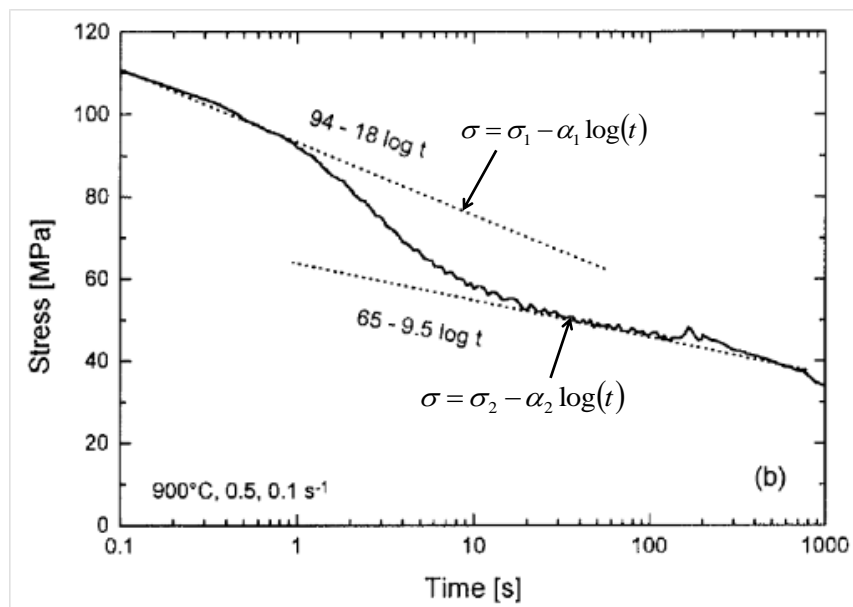


Figure 2.6 A typical stress relaxation curve with three distinct stages (after Karjalainen 1996)

In the first and third stage the stress behavior can be described by

$$\sigma = \sigma_1 - \alpha_1 \log(t) \quad (2.36)$$

$$\sigma = \sigma_2 - \alpha_2 \log(t) \quad (2.37)$$

where σ_1 , and σ_2 are the values of initial stress in the first and third stage, and α_1 , and α_2 are constants.

In the second stage, the partially recrystallized material consists of work hardened grains and recrystallized grains. Karjalainen proposed the mixture rule which can be applied to estimate the flow stress in the partially recrystallized microstructure (Karjalainen 1995):

$$\sigma_{flow} = (1 - f_{REX}) [\sigma_1 - \alpha_1 \log(t)] + f_{REX} [\sigma_2 - \alpha_2 \log(t)] \quad (2.38)$$

where f_{REX} is the recrystallized fraction, and subscripts 1 and 2 refer to the first stage and the third stage of the softening behavior. Rearranging equation (2.38) the recrystallized fraction can be derived as:

$$f_{REX} = \frac{[\sigma_1 - \alpha_1 \log(t)] - \sigma_{flow}}{[\sigma_1 - \alpha_1 \log(t)] - [\sigma_2 - \alpha_2 \log(t)]} \quad (2.39)$$

An example of the calculated recrystallized fraction obtained from stress relaxation data are shown in [Figure 2.7](#).

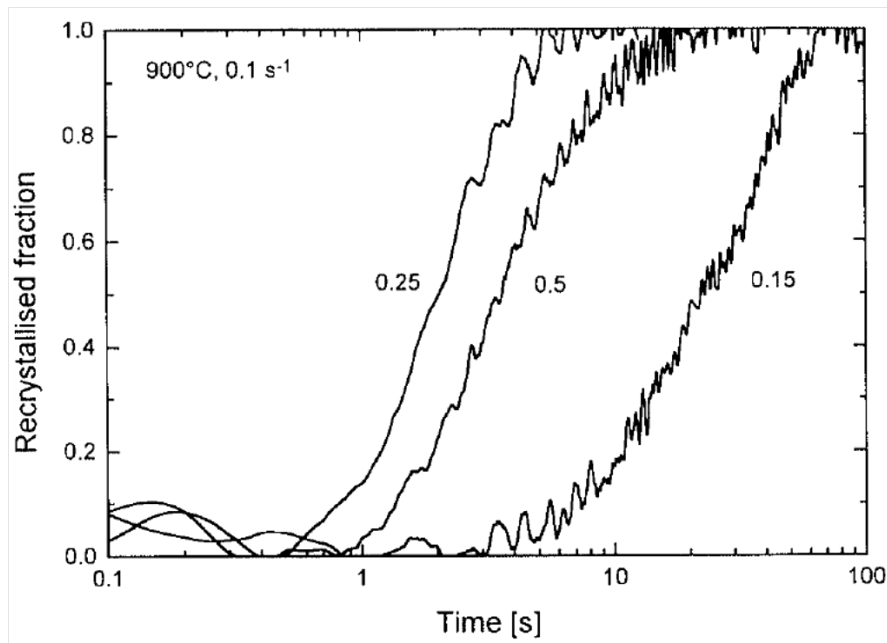


Figure 2.7 An example of the calculated recrystallized fraction (Karjalainen 1996)

The stress relaxation method allows the restoration behavior to be monitored continuously. Thanks to this, sufficient data to determine the restoration behavior under given conditions can be obtained by a single trial. Therefore, it is more advantageous compared to conventional methods (Liu 2012).

Concerning the application of the stress relaxation test in the work related to steel, in many cases, the method is applied to austenitic steels. Although the work focusing on the recovery kinetics of ferritic steel was carried out by Smith et al. (Smith 2004), to the author's best knowledge, few researches have focused on the recrystallization kinetics of ferritic steel.

Chapter 3. Experimental Work

In this chapter, the details of the experimental work will be introduced. To examine the microstructure evolution and its kinetics, two types of experiments were performed. Section 3.1 will introduce the material which was used in the experimental work. Section 3.2 will cover the single hit deformation test, and section 3.3 will introduce the stress relaxation test.

3.1. Materials

The model alloy was designed based on phase equilibrium calculations employing the TCFE6 database of Thermocalc. The chemical composition of this alloy is Fe, 0.05wt% C, 1.5wt% Al, 1.0 wt% Mn, and 0.4wt% Si. Al and Si were added as a ferrite stabilizer and Mn was added as an austenite stabilizer. According to the isopleths shown in [Figure 1.5](#), the two phase region (ferrite and austenite) of this steel covers the temperature range from 1400°C down to 750°C, which encompasses typical slab soaking furnace and hot rolling temperature.

The equilibrium volume fraction of austenite as a function of temperature is shown in [Figure 3.1](#). Three different types of equilibrium calculation, full-equilibrium, local-equilibrium-no-partitioning (LENP), and para-equilibrium, were carried out to simulate the volume fraction change with temperature. To confirm simulation results, isothermal holding experiments were carried out. The LENP calculation and the experimental result showed reasonable agreement of behavior of volume fraction change. According to this result, the volume fraction of austenite phase ranged from 10 to 20% between 800°C and

1300°C. The microstructure homogenized at 1060°C for 60 minutes is shown in [Figure 1.6](#). It consists of approximately 15% martensite (dark phase) which is distributed within ferrite (light phase). The martensite formed as a result of the transformation of high temperature austenite during quenching. This model alloy steel was prepared by induction melting (40kg) at CANMET Materials (Hamilton, ON). It was hot rolled to a plate of 15mm thickness. The material was machined into appropriate shapes suitable for each experimental work.

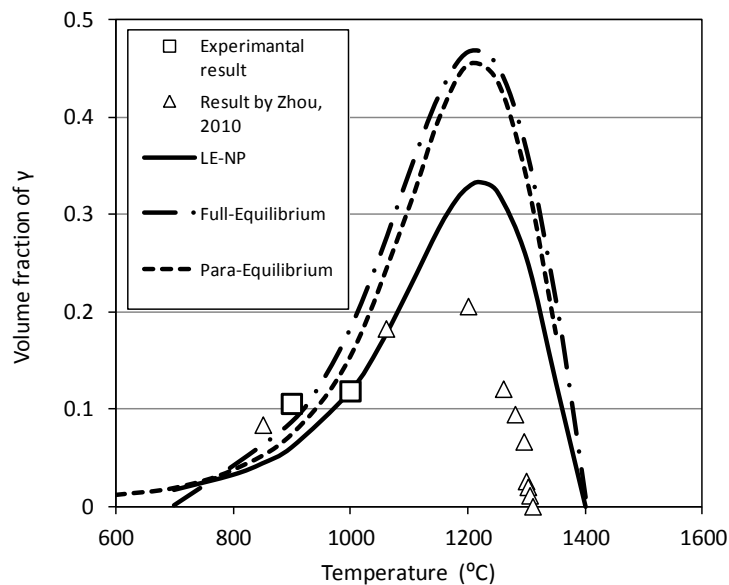


Figure 3.1 The equilibrium volume fraction of γ as a function of temperature

3.2. Single hit deformation test

The purpose of the single hit deformation test is to observe the microstructure evolution and examine the recovery and recrystallization kinetics in the model alloy during deformation and following isothermal annealing.

3.2.1. Experimental Set-up

The cylindrical compression specimens with a diameter of 10mm and a height of 15mm were machined from the hot rolled plate as shown in [Figure 3.2](#). The hot deformation simulations were carried out at CANMET Materials (Hamilton, ON) using the Gleeble[®] 3800 thermomechanical simulator.

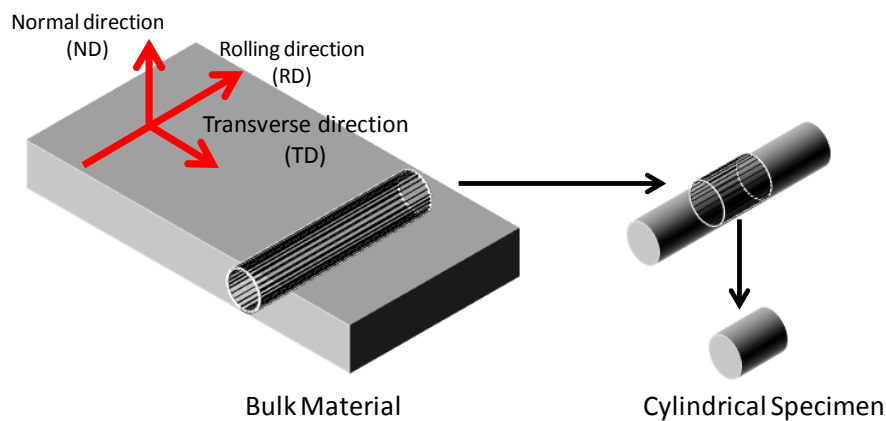


Figure 3.2 The schematic image of machining of cylindrical specimen

3.2.2. Experimental Procedure

The schematic experimental process diagram is shown in [Figure 3.3](#). The cylindrical specimens were homogenized at 1060°C for 60min under vacuum and quenched prior to hot deformation simulation. The hot deformation simulations consist of a 5min soaking at different target temperature of 800°C, 900°C and 1000°C, followed by the true uniaxial compression to a strain of 0.6 at a strain rate of 1.0s⁻¹ and 10.0s⁻¹. The specimens were gas-jet quenched after isothermal holding times of 0, 60 and 300sec. The initial cooling rate was approximately 30°C/sec.

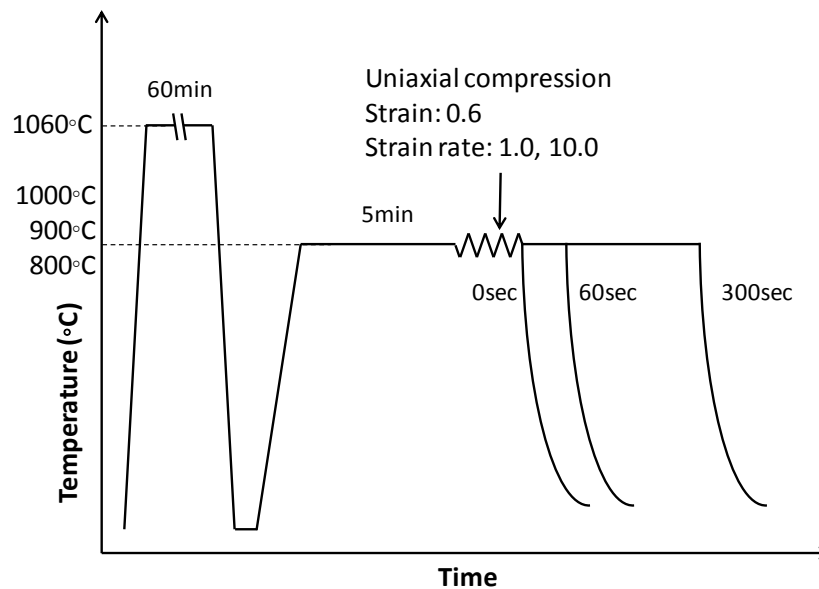


Figure 3.3 Schematic process diagram for single hit deformation test

The specimens were cut along the compression direction and ferrite grain boundaries, subgrain boundaries in ferrite grains, and martensite grains were observed by optical microscopy in specimens etched by 2% nitric acid in ethanol (2% Nital). The optical microscopy images were obtained using the Nikon Eclipse LV100 system and NIS Elements ver.4.0 software. Subgrains and recrystallized grains were observed by Differential Interference Contrast (DIC) image and subgrain size was measured by the line intercept method from DIC images. The EBSD analysis for subgrain and recrystallized grain observation was made on a JEOL JSM-7000F FEG-SEM with a CCD detector. An accelerating voltage of 20kV, a working distance of 18.4mm and a tilt angle of 70° were used for EBSD analysis. A step size of 0.2 μ m, and a grid of 1000 x 750 were employed for subgrain observation, and a step size of 0.5 μ m and a grid of 1263 x 946 were employed for recrystallization observation.

3.3. Stress relaxation test

The purpose of the stress relaxation test is to study recovery and recrystallization behavior continuously in the model alloy by means of thermomechanical processes.

3.3.1. Experimental Set-up

This experimental work was carried out using a Gleeble[®] 3800 thermomechanical simulator for high strain rate condition, and DIL 805D (TA instrument Inc.) deformation dilatometer for low strain rate condition. All tests were carried out at CANMET Materials (Hamilton, ON). The dimensions of high strain rate specimens were the same as those

used for the single hit deformation tests described earlier. Cylindrical specimens with a diameter of 5mm and a height of 10mm were used for the low strain rate condition.

3.3.2. Experimental Procedure

The schematic experimental process diagram is shown in [Figure 3.4](#). The cylindrical specimens were homogenized under vacuum at 1060°C for 60min and quenched. Prior to testing, the specimens were soaked at 1000°C for 5min and then cooled down to a target temperature followed by uniaxial compression to strains of 0.12 and 0.6, using strain rates of 1.0s⁻¹ and 10.0s⁻¹. For the high strain rate tests (10.0s⁻¹), target temperatures of 700°C, 750°C, 800°C, and 900°C, were employed. The low strain rate tests (1.0s⁻¹) were carried out at 800°C, and 900°C. After deformation, the specimen was isothermally held under constant displacement for 600sec followed by gas-jet quenching. The applied force was measured during the isothermal holding time.

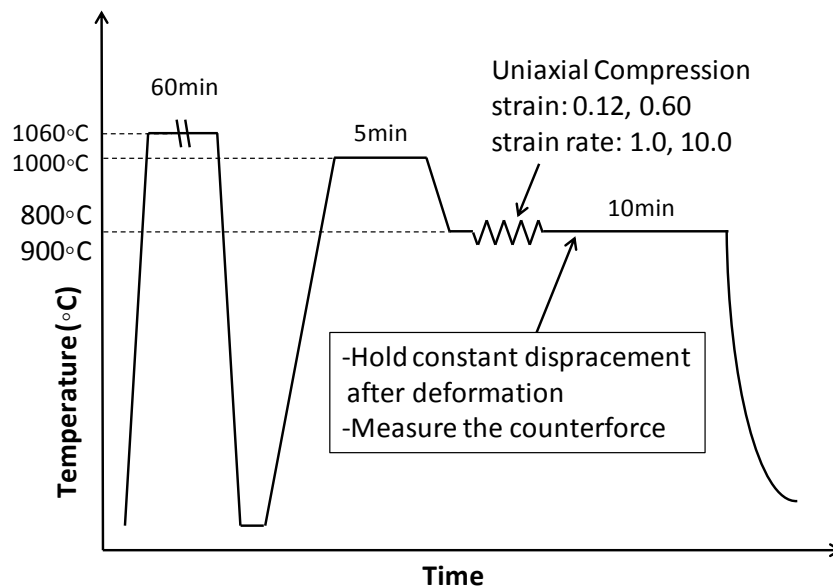


Figure 3.4 Schematic process diagram for stress relaxation test

To observe the final microstructure, the specimens were cut along the compression direction and ferrite grain boundaries, subgrain boundaries within ferrite grains, and martensite grains were revealed by using 2% Nital. The optical microscopy images were obtained on a Nikon Eclipse LV100 system and NIS Elements ver.4.0 software. To distinguish recrystallized grains from non-recrystallized grains, the microstructure was observed by DIC.

Chapter 4. Results

In this chapter, experimental results on microstructure evolution and kinetics in single hit deformation will be summarized in section 4.1. Results on the stress relaxation test for the kinetics of ferrite microstructure evolution is presented in section 4.2.

4.1. Single hit deformation test

The purpose of single hit deformation test is to observe microstructure evolution in single pass of hot deformation. The specimens were deformed under various combinations of temperatures and strain rates. The flow stress behavior, and work hardening behavior during deformation were analyzed, and the microstructure evolution during annealing following hot deformation were observed focusing on the subgrain formation and coarsening as well as recrystallization and grain growth.

4.1.1. Stress-strain behavior

The true-stress vs. true-strain curves (S-S curves) of various combinations of temperatures and strain rates are shown in [Figure 4.1](#). The flow stress level increased for lower temperature and higher strain rate conditions. Following initial work hardening (in the region $\varepsilon < 0.1$), the flow stress gradually increased in each conditions. The work hardening rate, $d\sigma_{\text{flow}}/d\varepsilon$, as a function of the strain is shown in [Figure 4.2](#). The scatter in these plots ([Figure 4.2](#)) is caused by the small sampling increment of data. The work hardening ratios were initially high and decreased rapidly in the region $\varepsilon < 0.1$. In the region $\varepsilon > 0.1$, the work hardening rates gradually got close to zero.

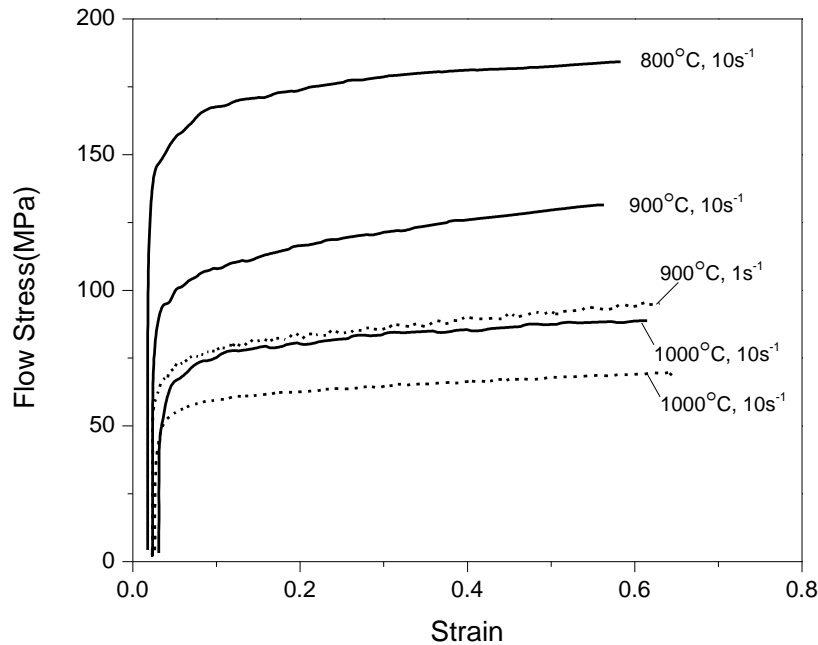
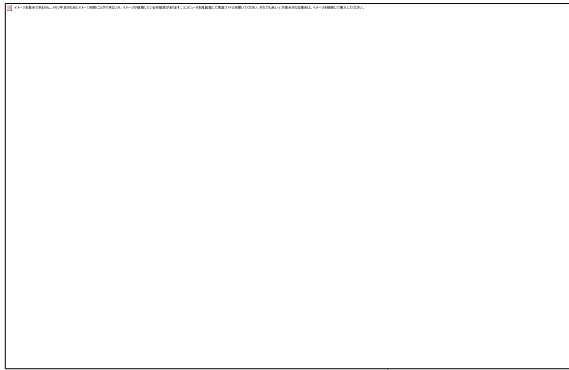
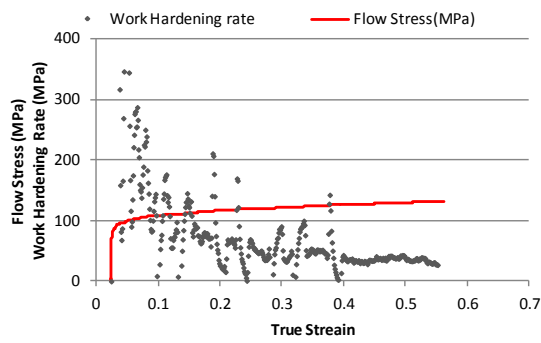


Figure 4.1 Stress Strain Curves in different combination of temperature and strain rate

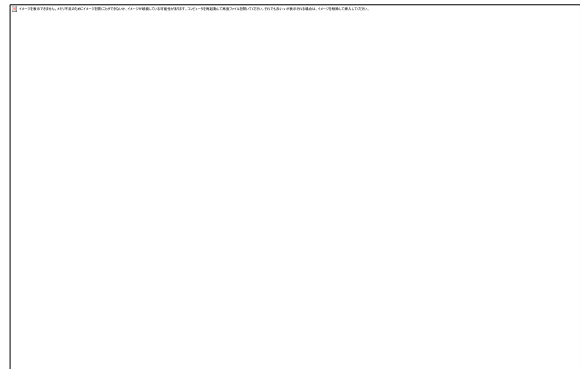
This flow stress and work hardening behavior is characteristic of dynamically recovered materials. Regarding dynamic recrystallization, the flow stress curves typically exhibit a broad peak followed by softening until the flow stress reaches a plateau. However, this behavior was not observed in the flow stress curves in [Figure 4.1](#).



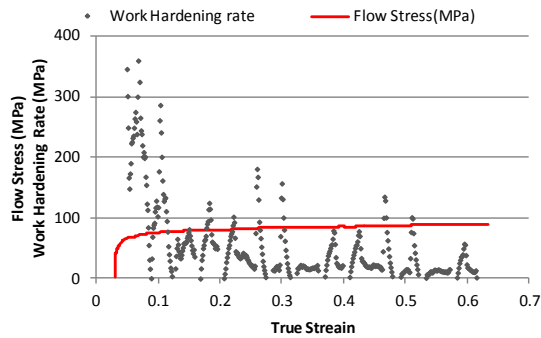
(a) 800°C, 10.0s⁻¹



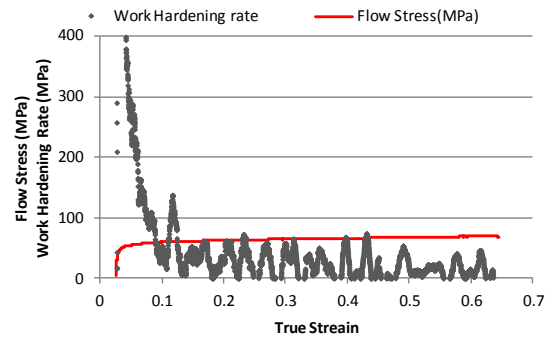
(b) 900°C, 10.0s⁻¹



(c) 900°C, 1.0s⁻¹



(d) 1000°C, 10.0s⁻¹



(a) 1000°C, 1.0s⁻¹

Figure 4.2 Work hardening ratio during deformation

Constitutive equations describing flow stress, σ_{flow} , in terms of the Zener-Hollomon parameter (Z) can be expressed as equation (2.10) - (2.12). The peak stress, σ_p , or steady state stress, σ_{st} , is used to define the constants in the constitutive equation and to determine the deformation activation energy (Ouchi and Okita, 1983). However, neither the peak stress nor the steady state stress can be defined well in the flow stress curves in this experiment. Therefore, the stress at various strain increments, σ_ε , was introduced instead of σ_{flow} to calculate the constants in the constitutive equations and average deformation activation energy. The values of σ_ε at various strain increments (0.1, 0.15, 0.2, 0.25, 0.3, 0.35, 0.4, 0.45, 0.5, 0.55, and 0.6) were employed for calculation (Mehtonen 2013).

Taking the logarithm of both sides of equation (2.10)-(2.12),

$$\ln \dot{\varepsilon} + \frac{U_{def}}{R} \left(\frac{1}{T} \right) = \ln A + n \ln [\sinh(\alpha \sigma_\varepsilon)] \quad (4.1)$$

$$\ln \dot{\varepsilon} + \frac{U_{def}}{R} \left(\frac{1}{T} \right) = \ln A' + n' \ln \sigma_\varepsilon \quad (4.2)$$

$$\ln \dot{\varepsilon} + \frac{U_{def}}{R} \left(\frac{1}{T} \right) = \ln A'' + \beta \sigma_\varepsilon \quad (4.3)$$

Under the condition of constant temperature, partially differentiate equation (4.1), (4.2) and (4.3) by $\sinh(\alpha \sigma_\varepsilon)$, $\ln(\sigma_\varepsilon)$, and, σ_ε , respectively,

$$n = \left[\frac{\partial \ln \dot{\varepsilon}}{\partial \ln(\sinh \sigma_\varepsilon)} \right]_T \quad (4.4)$$

$$n = \left[\frac{\partial \ln \dot{\epsilon}}{\partial \ln \sigma_{\epsilon}} \right]_T \quad (4.5)$$

$$\beta = \left[\frac{\partial \ln \dot{\epsilon}}{\partial \sigma_{\epsilon}} \right]_T \quad (4.6)$$

The determined value of constants by means of equation (4.4) – (4.6) and equation (2.8) are showed in Table 4.1.

Table 4.1 The calculated values of constants, β , n' , α and n at stain of 0.1-0.6

Strain	Power law	Exponential law	Hyperbolic sine law	
	n'	β	α	n
0.10	9.524	0.126	0.013	7.528
0.15	8.767	0.112	0.013	6.832
0.20	8.709	0.107	0.012	6.692
0.25	8.366	0.101	0.012	6.362
0.30	8.528	0.102	0.012	6.448
0.35	8.902	0.105	0.012	6.697
0.40	9.368	0.108	0.012	6.963
0.45	9.276	0.105	0.011	6.842
0.50	9.557	0.107	0.011	7.024
0.55	9.617	0.107	0.011	7.031
0.60	9.404	0.104	0.011	6.854
Average	8.974	0.107	0.012	6.784

Under the condition of constant strain rate, partially differentiate equation (4.1) – (4.3) by (1/T),

$$U_{def} = Rn \left[\frac{\partial \ln \{ \sinh(\alpha \sigma_{\varepsilon}) \}}{\partial (1/T)} \right]_{\dot{\varepsilon}} \quad (4.6)$$

$$U_{def} = Rn' \left[\frac{\partial \ln \sigma_{\varepsilon}}{\partial (1/T)} \right]_{\dot{\varepsilon}} \quad (4.7)$$

$$U_{def} = R\beta \left[\frac{\partial \sigma_{\varepsilon}}{\partial (1/T)} \right]_{\dot{\varepsilon}} \quad (4.8)$$

The activation energy for deformation calculated by equation (4.6) – (4.8) and constants in [Table 4.1](#) are shown in [Table 4.2](#).

The value of average activation energy was 339kJ/mol, 333kJ/mol, 334kJ/mol by the power law, the exponential law, and the hyperbolic sine law, respectively. The range of U_{def} for ferritic steel given by other researchers is from 280kJ/mol for pure iron (Glover 1973) to 397kJ/mol for 21wt%Cr stainless steel (Mehtonen 2013). The values in present work were close to the Fe-1.8wt% Al alloy, 334kJ/mol (Ouchi 1983).

Table 4.2 The calculated activation energy of deformation at strain of 0.1-0.6

strain	Power law	Exponential law	Hyperbolic sine law
	U_{def} [kJ/mol]	U_{def} [kJ/mol]	U_{def} [kJ/mol]
0.10	330.31	321.63	323.49
0.15	358.36	342.76	346.89
0.20	321.44	310.44	313.53
0.25	307.80	300.39	302.06
0.30	321.62	314.29	315.75
0.35	327.90	315.83	319.67
0.40	355.47	350.27	350.43
0.45	347.70	346.81	345.00
0.50	354.69	353.59	351.86
0.55	357.02	355.54	353.98
0.60	356.34	356.45	354.00
Average	339	333	334

4.1.2. Recovery and subgrain formation

A representative image of the low magnification microstructures in the specimens quenched immediately after hot deformation is shown in [Figure 4.3](#). The squished original ferrite grains with deformed structure can be observed. Once again, black particles are martensite. Some ferrite grains appear darker than others because the darker grains possess a more deformed structure than the others.

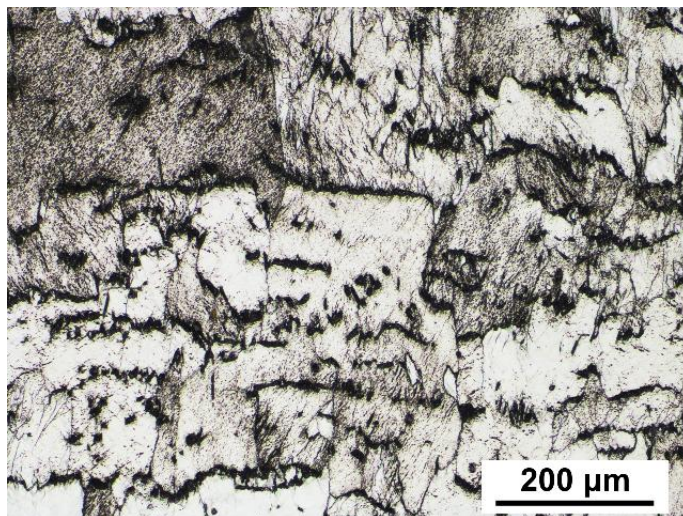


Figure 4.3 As-deformed structure in model alloy (at 800°C, $\epsilon=0.6$, $\dot{\epsilon} =10.0s^{-1}$, and 0sec holding time)

The optical image, the DIC images, and the EBSD image in same field of view are shown in [Figure 4.4](#). High angle grain boundaries (HAGB) with a misorientation of 15° or more are shown in black and low angle grain boundaries (LAGB) with a misorientation between 1 to 15° are shown in white in the EBSD image. It can be observed that

subgrains surrounded by LAGB were formed within the ferrite matrix, and a small number of recrystallized nuclei started bulging into the deformed grains. The heterogeneity of the microstructure is evident from the fact that some parts of the area in Figure 4.4 (c) contain less LAGBs than other parts. Comparing the EBSD and the optical images, it can be observed that small grains surrounded by HAGBs in the EBSD image correspond to regions which consist of small martensite grains and small ferrite grains in the optical image. This indicates that these grains are not due to subgrain formation; rather these are due to decomposition of initial austenite grains. Comparing the EBSD image and the DIC image, subgrain boundaries were well revealed by Nital etching and DIC imaging method. Therefore, subgrain size can be measured from DIC images.

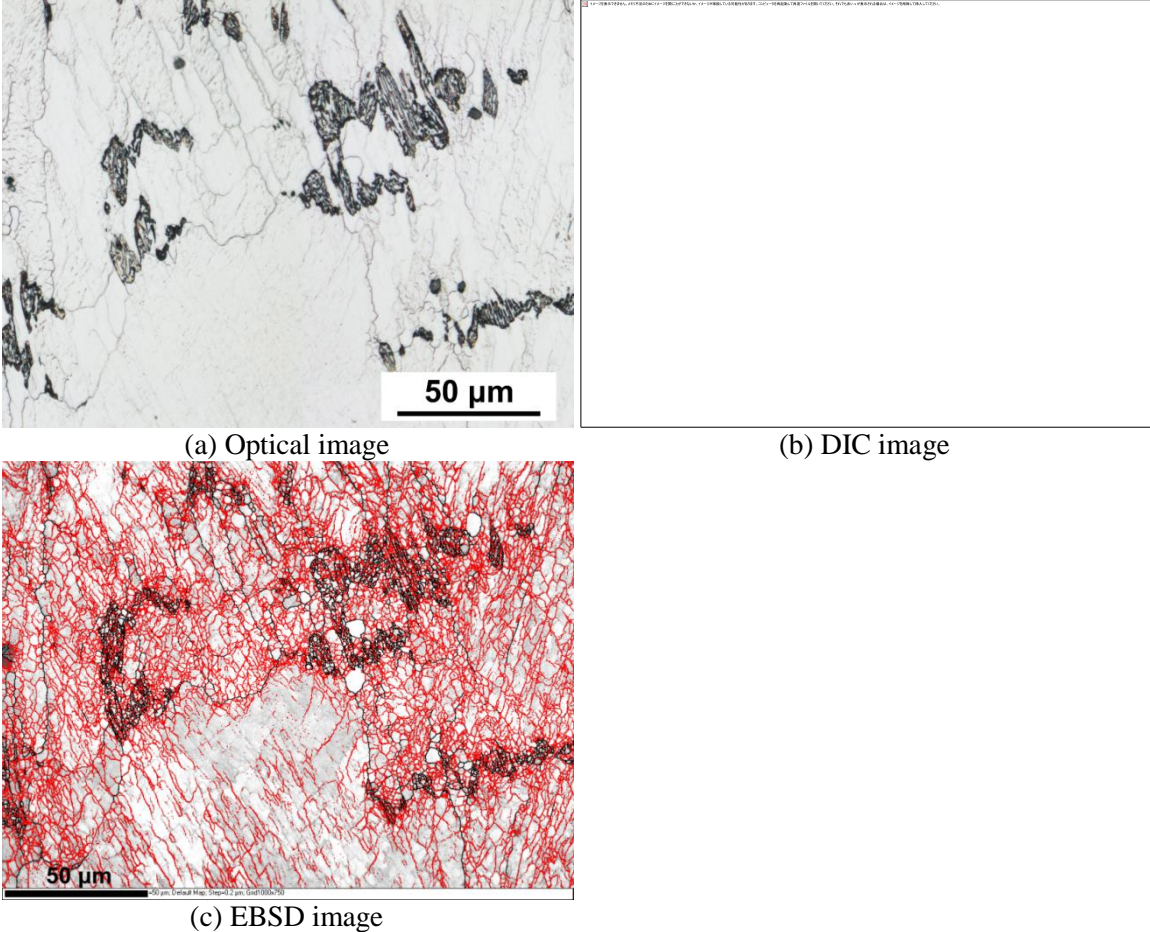


Figure 4.4 Microstructure with different imaging method (at 800°C, $\epsilon=0.6$, $\dot{\epsilon} = 10.0s^{-1}$, and 0sec holding time.)

The DIC images as a function of Z parameter are shown in [Figure 4.5](#) covering the Z parameter from $4.56 \times 10^{13} \text{s}^{-1}$ to $1.56 \times 10^{17} \text{s}^{-1}$. Subgrains coarsened, and became equiaxial with decreases of the Z parameter.

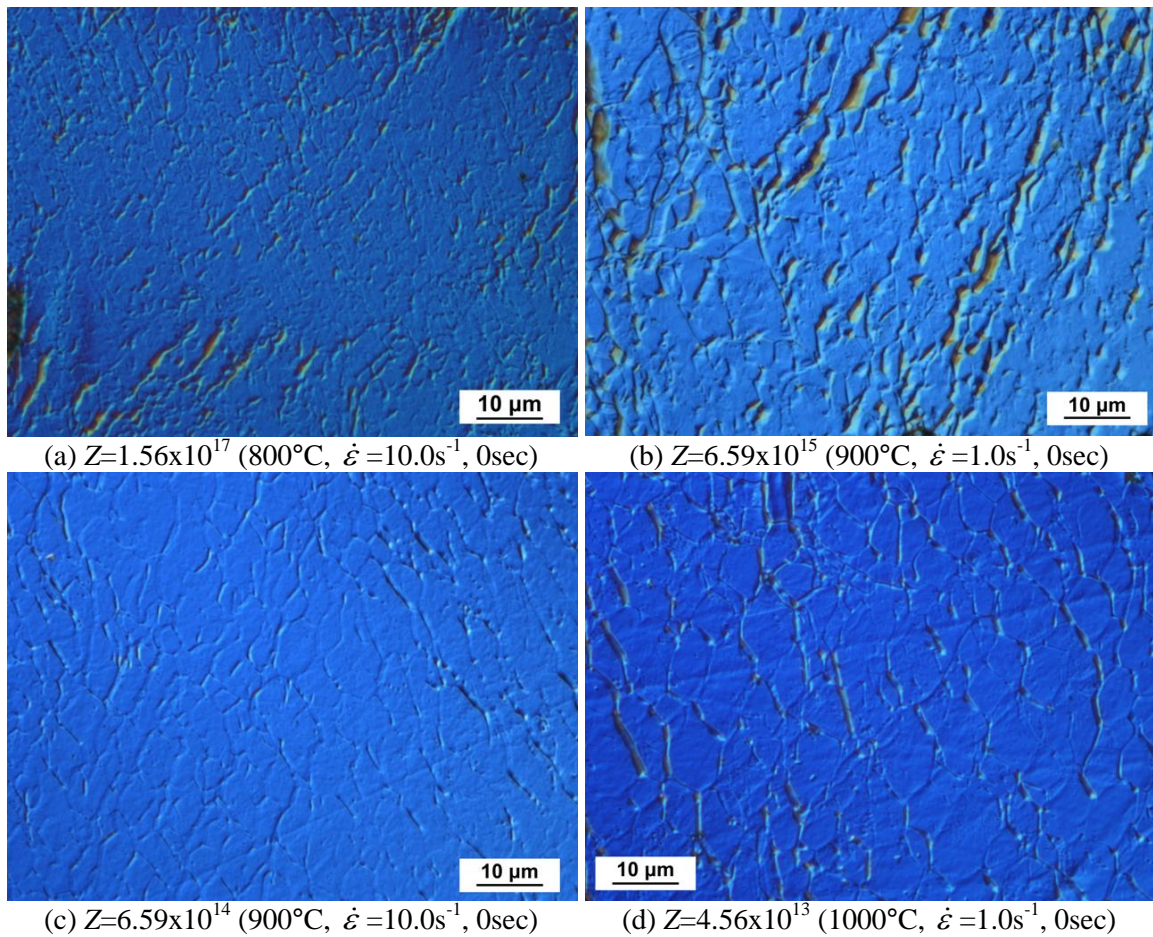


Figure 4.5 DIC images as a function of Z parameter

Subgrain size was measured in the specimens deformed to strain of 0.6 at strain rate of 1.0s^{-1} and 10.0s^{-1} , and temperature of 800°C , 900°C , and 1000°C . The subgrain size distribution at different temperature and same strain rate is shown in [Figure 4.6](#). The distribution corresponds well to the log-normal distribution. The logarithmic mean subgrain sizes are plotted as a function of flow stress in [Figure 4.7](#), where the flow stress at a strain 0.5 is selected as representative because the stress strain curves continuously increased for this level of strain. The relation between flow stress σ_{flow} and subgrain diameter d_s was expressed by

$$\sigma_{flow} = K \cdot d_s^{-N} \quad (4.9)$$

According to [Figure 4.7](#), the value of K and N are 573.49 and 1.39 as obtained by equation (4.9). This value of N was relatively large as compared with the values obtained from dynamic recovery of other metals such as pure iron, 1.2 ± 0.2 (Glover 1973), or Fe-1.8wt%Al alloy, 0.74 (Ouchi 1983).

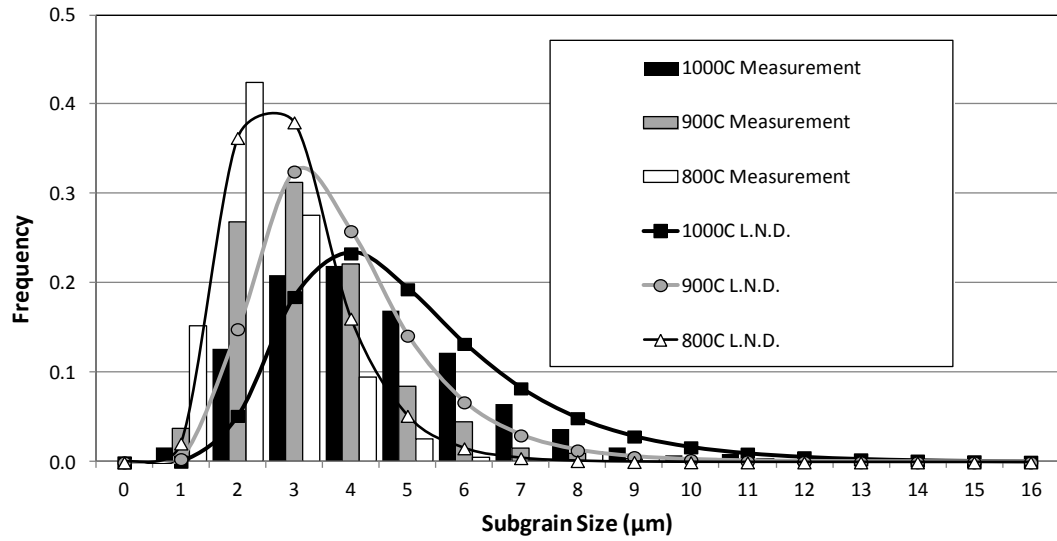


Figure 4.6 Subgrain size distribution at strain rate of 10.0s-1 in different temperature

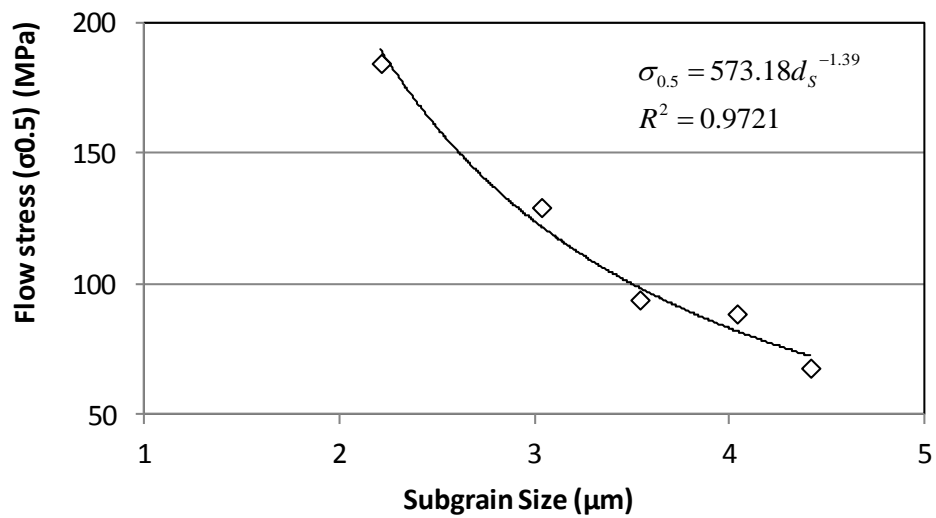


Figure 4.7 Dependence of subgrain size on flow stress

The subgrain growth was also observed for different annealing time. The logarithmic mean subgrain size at different temperature and strain rates as a function of time is shown in [Table 4.3](#) and [Figure 4.8](#). It should be mentioned that at high temperature and high strain rate the subgrain size cannot be measured since the deformed grains are eliminated by recrystallization. The arrows shown in [Figure 4.8](#) show that the first recrystallized grains were observed at 800°C and a strain rate of 10.0s⁻¹ at 900°C and a strain rate of 1.0s⁻¹. The subgrain size continuously increased with holding time and kept increasing even after the recrystallization started to take place.

Table 4.3 The logarithmic mean subgrain size change with holding time

Temperature	800°C		900°C		1000°C	
Strain rate	10.0 s ⁻¹	1.0 s ⁻¹	10.0 s ⁻¹	1.0 s ⁻¹	10.0 s ⁻¹	10.0 s ⁻¹
0sec	2.21	3.54	3.03	4.42	4.04	
60sec	5.12	5.07	REXed	REXed	REXed	
300sec	7.42	REXed	REXed	REXed	REXed	REXed

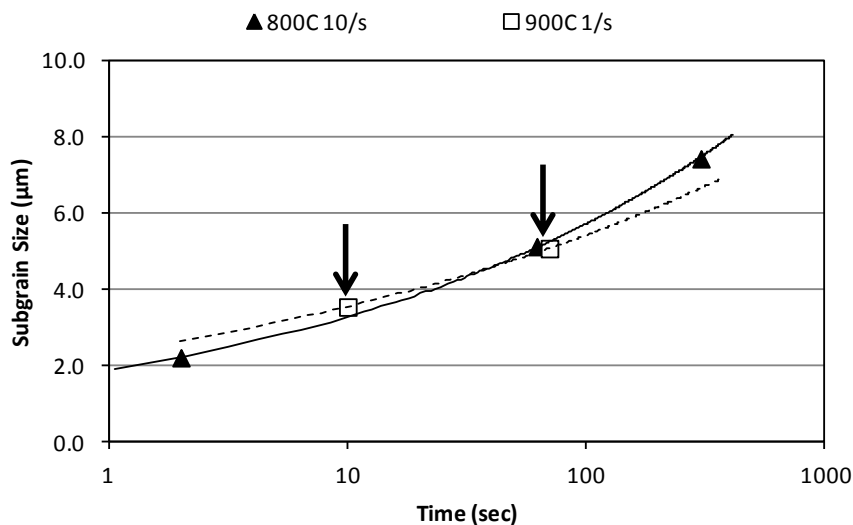
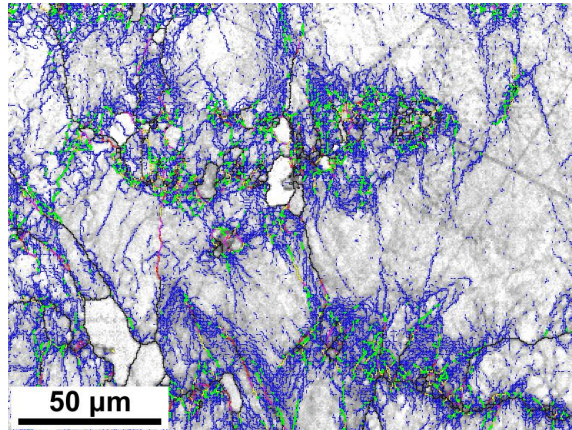


Figure 4.8 Subgrain size change with holding time

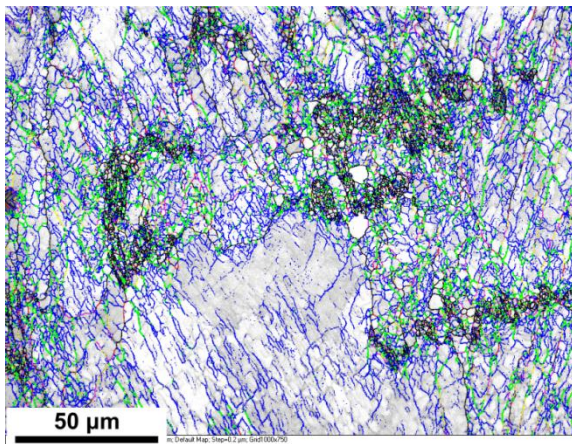
4.1.3. Interaction between Austenite and Ferrite on subgrain formation

The EBSD band slope maps with grain boundaries at different temperature, strain rate, and annealing time are shown in [Figure 4.9](#). The colors of boundaries in [Figure 4.9](#) represent different misorientation ranges. Blue, green, yellow, pink, red and black indicate, respectively, $1^\circ \leq \theta < 4^\circ$, $4^\circ \leq \theta < 7^\circ$, $7^\circ \leq \theta < 10^\circ$, $10^\circ \leq \theta < 13^\circ$, $13^\circ \leq \theta < 15^\circ$, $15^\circ \leq \theta$. Thus, black boundaries refer to HAGB, and others refer to LAGB.

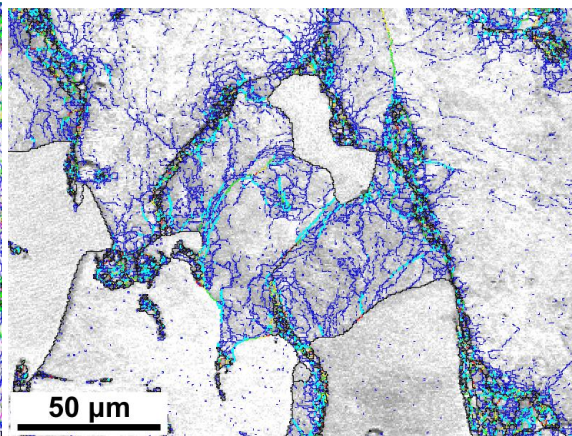
Immediately after hot deformation ([Figure 4.9 \(b\) and \(c\)](#)), it can be observed that LAGBs are located densely in the vicinity of austenite grains, while in the center of ferrite grains LAGBs are sparse. Regarding annealing time, as shown in [Figure 4.9 \(a\), \(b\) and \(c\)](#), LAGBs disappeared from the center of ferrite grains but still remained around austenite particles after annealing. As for the effect of strain rate, comparing [Figure 4.9 \(d\) and \(e\)](#), dislocation have been rearranged and subgrains were formed during deformation at lower strain rates. The subgrain size around austenite particles looked slightly smaller compared to other regions. Misorientation of LAGBs around austenite particles appeared higher compared to other regions (more green, yellow, and pink colored LAGBs appeared around austenite particles). This can be interpreted that the ferrite around austenite experienced higher deformation compared to the ferrite inside the grains due to the difference of hardness in the two phases, resulting in the more dislocations generated in the ferrite.



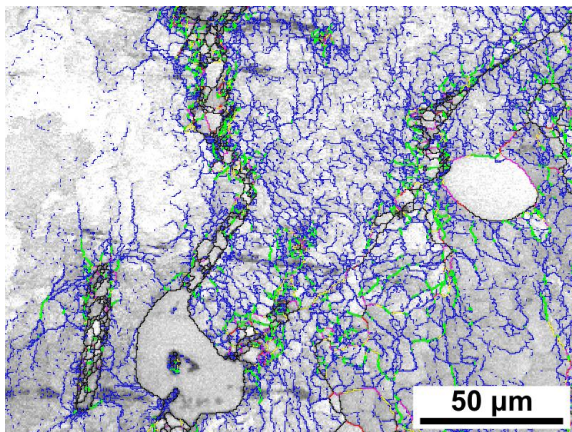
(a) 750°C, 0.6, 10.0s-1, 600sec



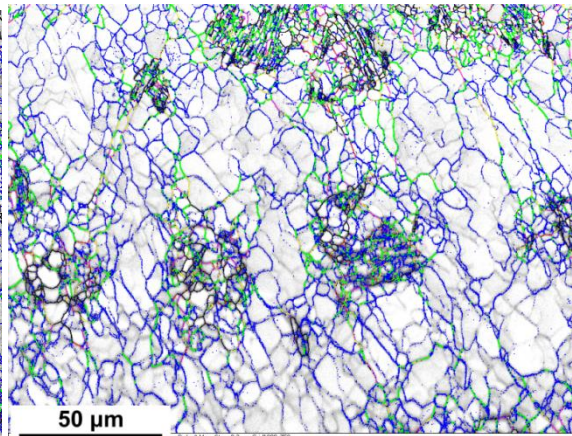
(b) 800°C, 0.6, 10.0s-1, 0sec



(c) 800°C, 0.6, 10.0s-1, 60sec



(d) 900°C, 0.6, 10.0s-1, 0sec



(e) 900°C, 0.6, 1.0s-1, 0sec

Figure 4.9 EBSD Band slope images with grain boundaries in different temperature, strain rate, and annealing time. High angle grain boundaries ($15^\circ \leq \theta$) and low angle grain boundaries ($1^\circ \leq \theta < 15^\circ$) are shown in black and red, respectively. (a) was obtained from stress relaxation test.

4.1.4. Recrystallization microstructure evolution

The microstructure evolution of specimens deformed at strain rates of 10.0s^{-1} and 1.0s^{-1} is shown in [Figure 4.10](#) and [Figure 4.11](#), respectively, as a function of the deformation temperature and holding time. The progress of recrystallization at 800°C is apparent in [Figure 4.10](#). Some recrystallized grains are present in the as-quenched structure. These probably formed during gas jet quenching. After holding for 300sec, most of the microstructure has recrystallized. At the other extreme, deformation and holding at 1000°C did not appear to lead to significant changes in the microstructure. Under the low strain rate condition recrystallization progressed more slowly than in the high strain rate condition. The grain size after 300sec holding showed no significant difference between the low and high strain rate conditions.

EBSD orientation maps for the strain rate of 10.0s^{-1} are shown in [Figure 4.12](#). High angle grain boundaries with a misorientation of 15° or more are shown in black while low angle grain boundaries with a misorientation between 2 to 15° are shown in white. The gradation of color within grains indicates the gradient of orientation, which means that those grains contain deformed structure. The uniform colored grains that contain no deformed structure are recrystallized grains. Several important observations need to be highlighted.

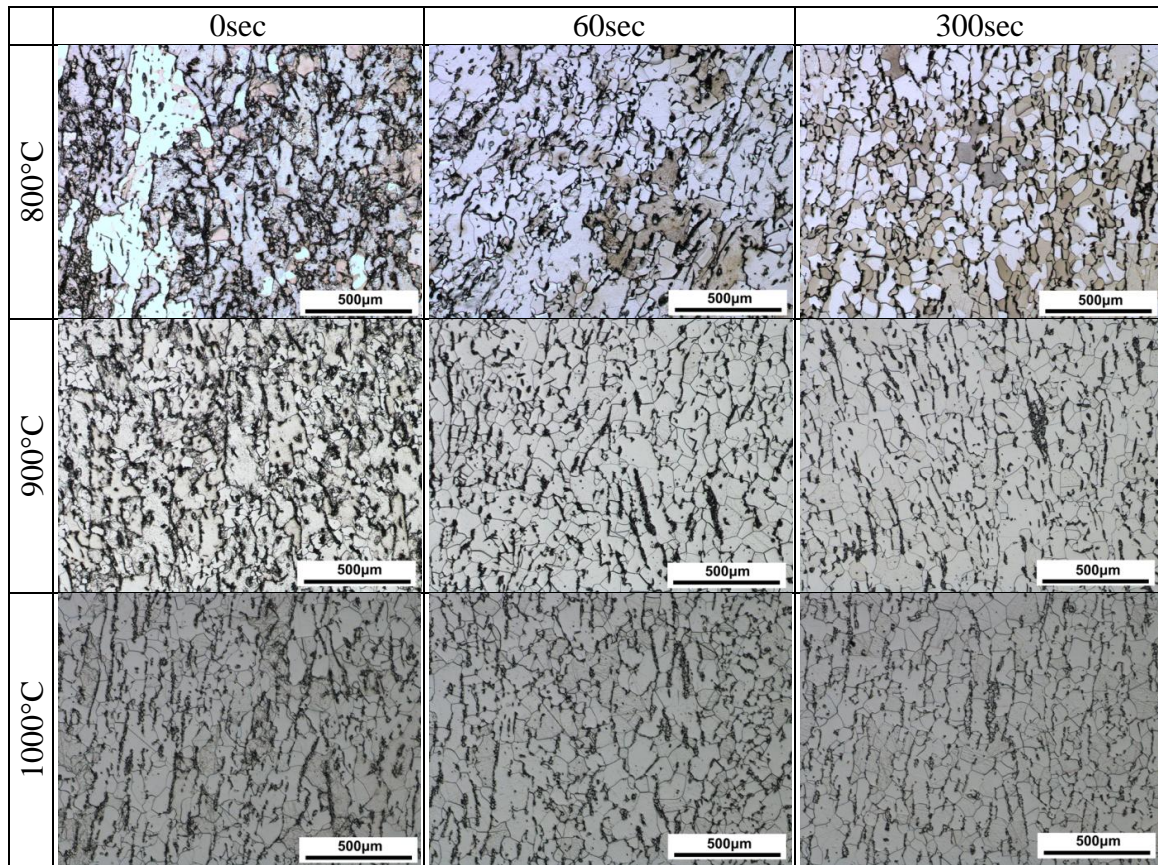


Figure 4.10 Microstructure evolution as a function of deformation temperature and holding time ($\varepsilon = 0.6$, $\dot{\varepsilon} = 10.0\text{s}^{-1}$)

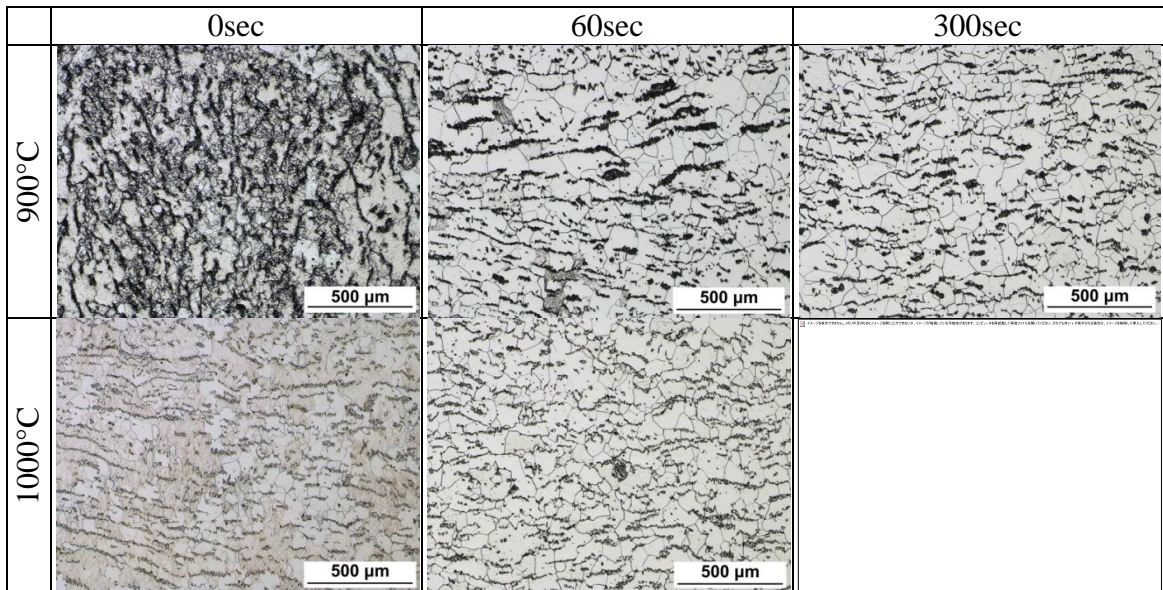


Figure 4.11 Microstructure evolution as a function of deformation temperature and holding time
($\varepsilon = 0.6$, $\dot{\varepsilon} = 1.0\text{s}^{-1}$)

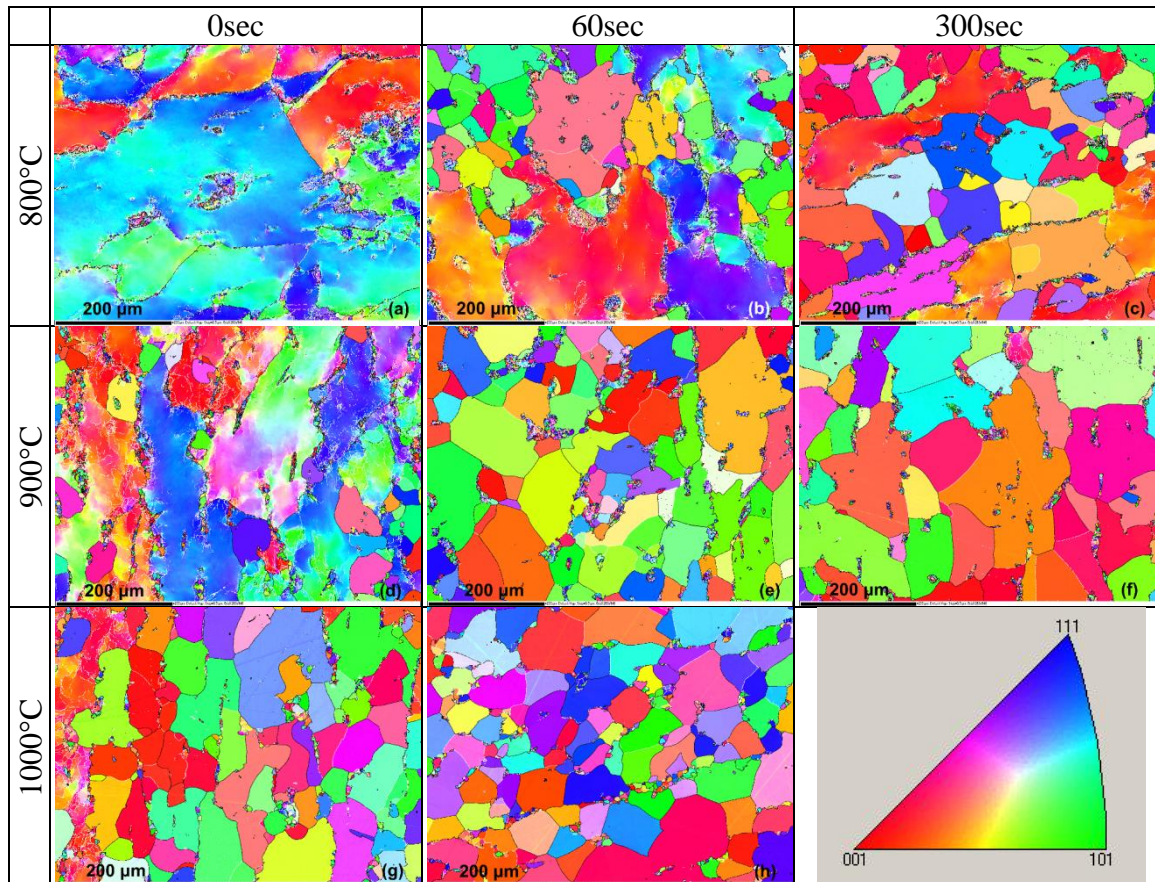


Figure 4.12 EBSD orientation maps as a function of deformation temperature and holding time ($\epsilon = 0.6$, $\dot{\epsilon} = 10.0\text{s}^{-1}$, (i): the Legend of IPF colors)

- Figure 4.12 (a) shows heterogeneity of the as-deformed microstructure. Some grains show strong misorientation gradients while others appear to have weak misorientation gradients.
- While optical images suggest that the microstructure is completely recrystallized after 300sec at 800°C, EBSD analysis suggests that some grains have not recrystallized and still show substructure.
- Some recrystallized grains are present within the as-deformed microstructure at 900°C. The as-deformed microstructure of the 1000°C sample is almost completely recrystallized.
- After 60sec holding time, the specimen fully recrystallized, and the coarsening of recrystallized grains can be observed between Figure 4.12 (e) and (f).

The small recrystallized grains found immediately after deformation at a strain rate of $10.0s^{-1}$ and a temperature of 800°C are shown in Figure 4.13 by EBSD analysis. The focused grains are indicated by arrows in the images. The Roman numerals, (i) and (ii) in Figure 4.13 indicate inverse pole figure (IPF) map and Band slope map, respectively. In Figure 4.13 (i), LAGB and HAGB are shown in white and black, respectively. In Figure 4.13 (ii), the legend of boundary colors follows that of Figure 4.9.

The grain in Figure 4.13 (a) and the grain (2) in Figure 4.13 (b) had similar characteristics. Its grain boundary consisted of HAGB and LAGB (Figure 4.13 (a-ii), (b-ii)). Its lattice orientation was close to that of adjacent grains across LAGB (Figure 4.13 (a-i), (b-i)). The bulging of its HAGB can be observed (Figure 4.13 (a-ii), (b-ii)). It can be concluded that these grains were attributed to the bulging of the HAGB with subgrain growth. The

grain (1) in [Figure 4.13 \(b\)](#) was completely surrounded by HAGB and was adjacent to a martensite particle. This grain can be considered to nucleate from phase boundaries.

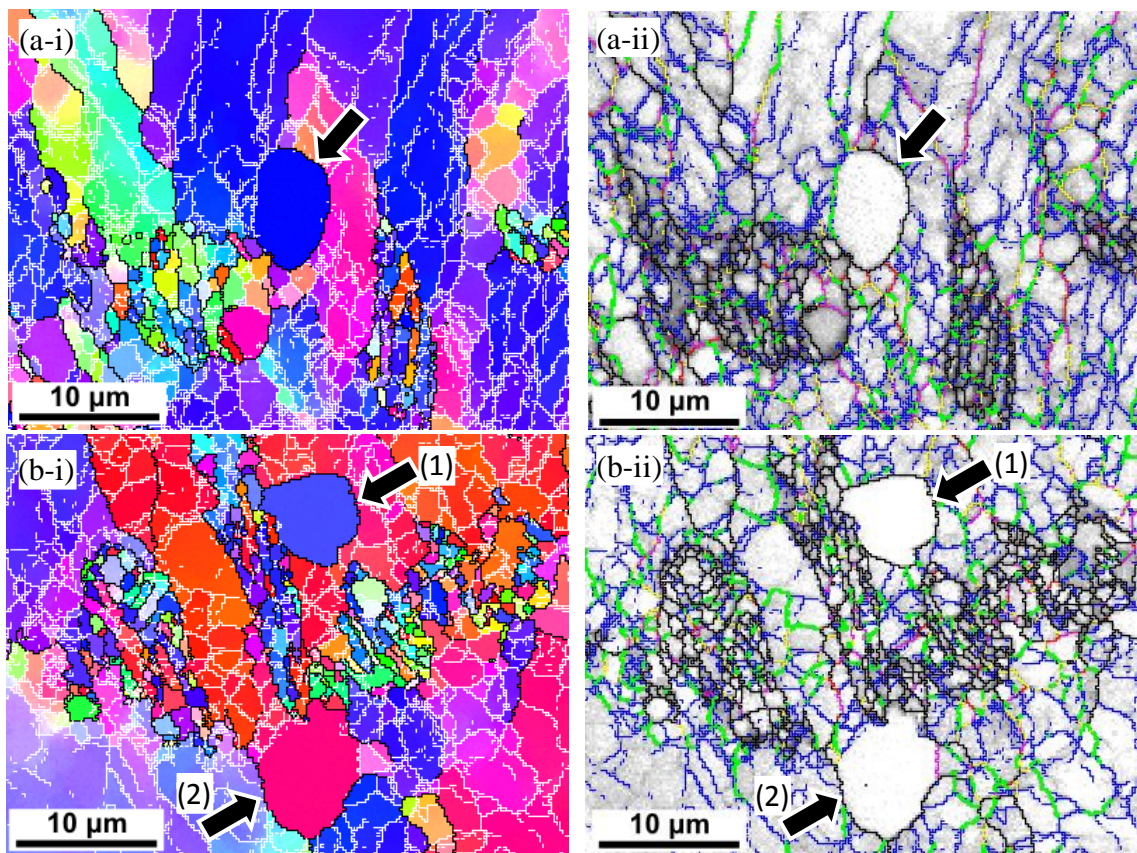


Figure 4.13 Recrystallized grain immediately after deformation at strain rate of 10.0s^{-1} , and 800°C

4.1.5. Recrystallization kinetics

The fraction of recrystallized grains for each combination of temperature and annealing time was determined by means of point counting method. The mean values of recrystallized fraction for strain rate of 10.0s^{-1} and 1.0s^{-1} are shown in [Table 4.4](#), and [Table 4.5](#), respectively.

Table 4.4 Recrystallized fraction change of strain rate of 10.0s^{-1} as a function of time

Temp.	800°C		900°C		1000°C	
Time	Optical	EBSD	Optical	EBSD	Optical	EBSD
0sec	0.01	0.02	0.17	0.16	0.86	0.92
60sec	0.25	0.31	0.85	0.97	0.95	0.99
300sec	0.81	0.77	0.97	0.99	0.97	

Table 4.5 Recrystallized fraction change of strain rate of 1.0s^{-1} as a function of time

Temp.	900°C	1000°C
Time	Optical	Optical
0sec	0.01	0.38
60sec	0.89	0.98
300sec	0.99	0.99

The isothermally recrystallized fraction, f_{REX} , as a function of time, t , can be expressed by an Avrami type empirical equation:

$$f_{REX} = 1 - \exp \left[-0.693 \left(\frac{t}{t_{0.5}} \right)^n \right] \quad (4.10)$$

where $t_{0.5}$ is the time for 50% recrystallization and n is known as the Avrami exponent.

The recrystallized fraction obtained by image analysis is plotted in [Figure 4.14](#): the open symbols are from optical images; and the close symbols are from EBSD images. The fraction can be fitted well with equation (4.10). The values of the Avrami exponent n and the 50% recrystallization time $t_{0.5}$ are shown in [Table 4.6](#).

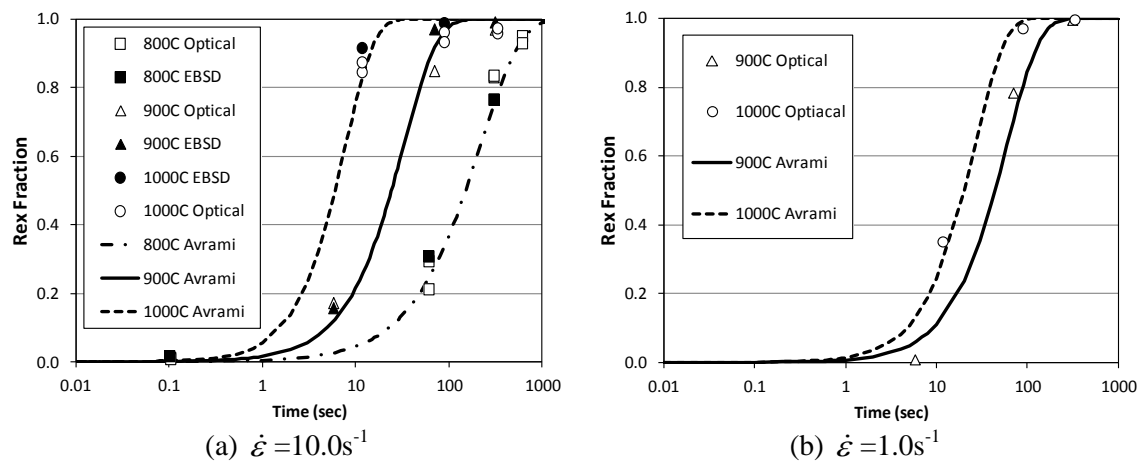


Figure 4.14 Recrystallized fraction obtained from image analysis with Avrami fits.

Table 4.6 Values of n and $t_{0.5}$ from [Figure 4.14](#)

Temperature	800°C		900°C		1000°C	
strain rate [s^{-1}]	10.0	10.0	1.0	10.0	1.0	10.0
n	1.0	1.2	1.2	1.4	1.3	1.3
$t_{0.5}$ [sec]	150	24	44	6	19	19

The Avrami exponent obtained from this experiment was between 1.0 and 1.4, which is lower than the typical value for the Avrami exponent in dynamically recovered type of materials, $n \sim 2.0$. Additionally, though, the Avrami exponent is generally independent from temperature and strain rate, its values varied with conditions. It can be presumed that this is related to the contribution of recovery by diminishing the driving force for recrystallization. On the other hand, regarding the 50% recrystallization time $t_{0.5}$, strong temperature dependence can be observed. Furthermore, the strain rate dependence of $t_{0.5}$ is also observed.

4.1.6. Austenite microstructure evolution

This section focuses on austenite microstructure evolution during hot deformation. The optical microscopy images and their corresponding volume fraction of austenite are shown in [Figure 4.15](#) to compare with before deformation and annealing and after those as a function of temperature. The volume fraction of martensite, which present as austenite in the deformed and annealing temperature state, showed the value of 10%-12%, and did not change significantly before and after deformation.

The change in the distance between adjacent austenite particles with deformation is shown in [Figure 4.16](#). The distance between particles in the direction of compression

direction decreased in proportion to the degree of deformation from approximately $90\mu\text{m}$ to $60\mu\text{m}$. On the other hand, the distance between particles in the direction normal to the compression direction became slightly larger each with deformation. These observations suggest that the austenite distribution changed simply with the degree of deformation. The kinetics behavior observed from stress behavior was mainly attributed to ferrite microstructural change under the deformation conditions employed in this work.

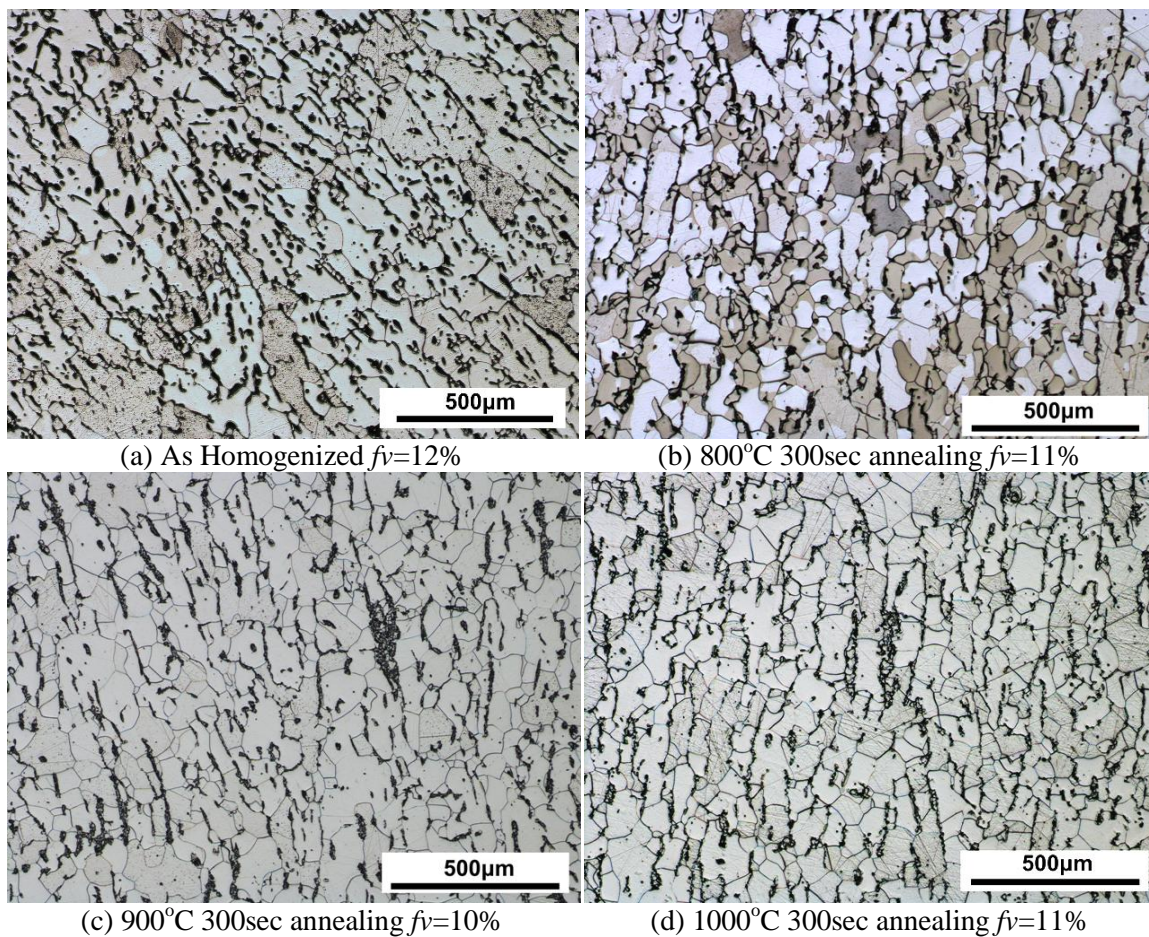


Figure 4.15 Volume fraction change of austenite as a function of temperature (deformed condition: strain of 0.6 strain rate of 10.0s^{-1})

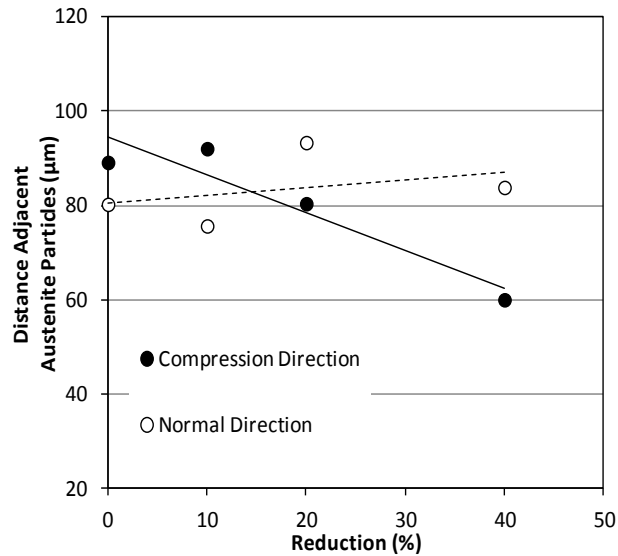


Figure 4.16 Distance change of austenite particles with deformation

4.2. Stress relaxation test

The stress relaxation test was carried out in order to continuously monitor the recovery and recrystallization kinetics of the model alloy. The softening behavior was measured during isothermal annealing after deformation. The microstructure after isothermal annealing was also observed to clarify how much recovery and recrystallization took place.

4.2.1. Microstructure observation

The microstructure after isothermal annealing for different conditions is shown in [Figure 4.17](#) and [Figure 4.18](#), and the recrystallized fraction is summarized in [Table 4.7](#). In the specimens deformed to strain of 0.12 at a strain rate of 1.0s^{-1} , the grains contained subgrains, and no equiaxed grains were observed leading to the conclusion that the

material did not recrystallize. Recovery was the only softening mechanism under this condition. On the other hand, for the strain of 0.6, clean uniaxial grains can be observed, meaning that the specimen fully recrystallized.

For a strain rate of 10.0s^{-1} and the strain of 0.12, the microstructure appeared the same as low strain rate condition. This indicates that specimens recovered under this condition as well. In contrast, for a strain of 0.12 at 700°C recrystallization nuclei can be observed in the vicinity of grain boundaries. The recrystallized fraction was 11% after 600sec annealing. At 750°C , though the recrystallized grain grew faster than at 700°C , the recrystallized fraction still remained 35% after 600sec annealing. On the other hand, in the higher temperature condition, at 800°C and 900°C , the recrystallized fraction reached more than 95%.

Based on the microstructure observation, the recovery model can be applied to all results of the strain of 0.12, and the result which is at a strain of 0.6, for a strain rate of 10.0s^{-1} and a temperature of 700°C , and for other results, the competition of recovery and recrystallization must be taken into account.

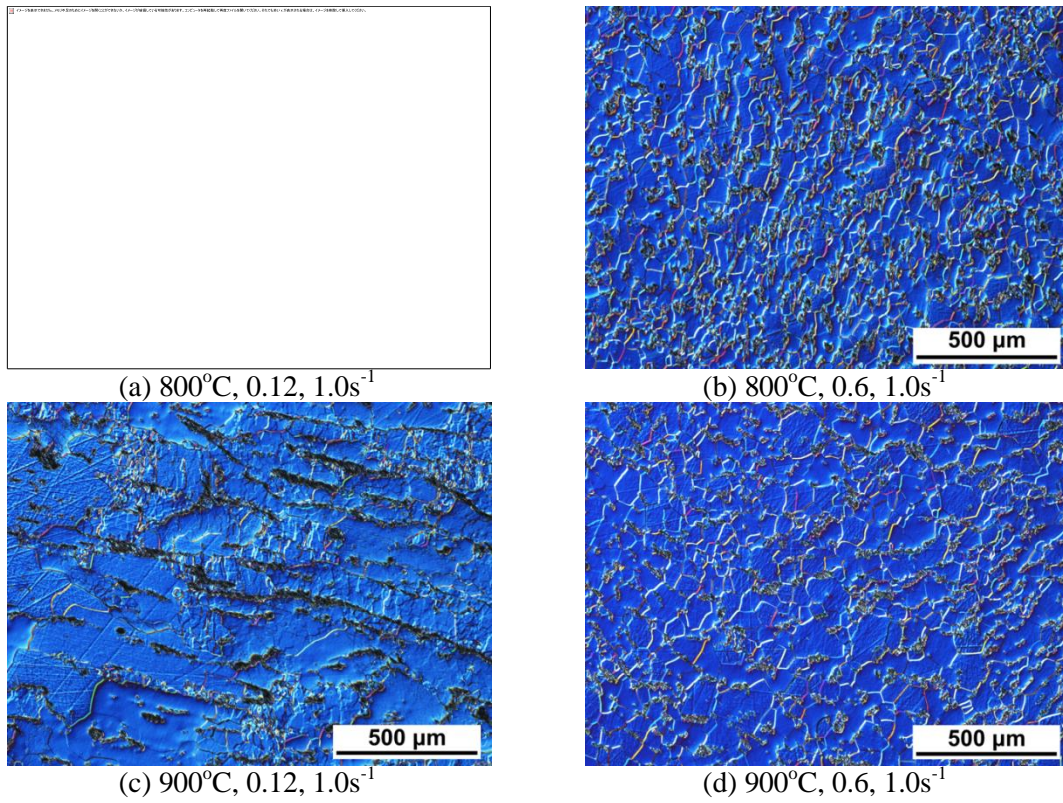
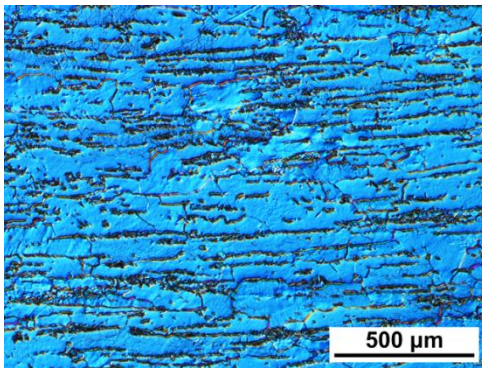
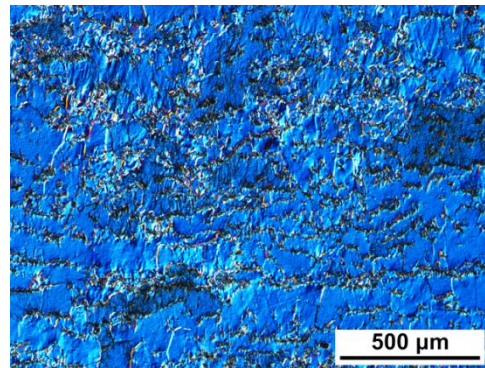


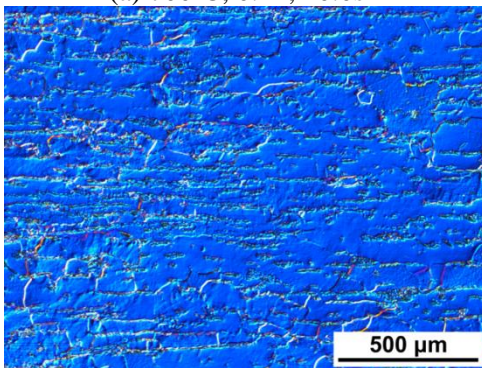
Figure 4.17 Microstructure after isothermal annealing for low strain rate



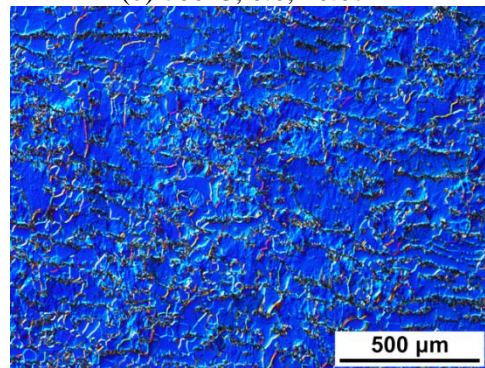
(a) 700°C, 0.12, 10.0s⁻¹



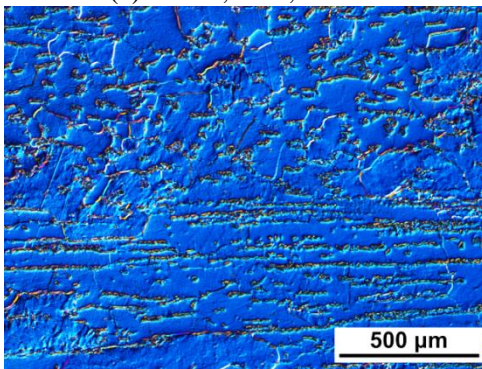
(b) 700°C, 0.6, 10.0s⁻¹



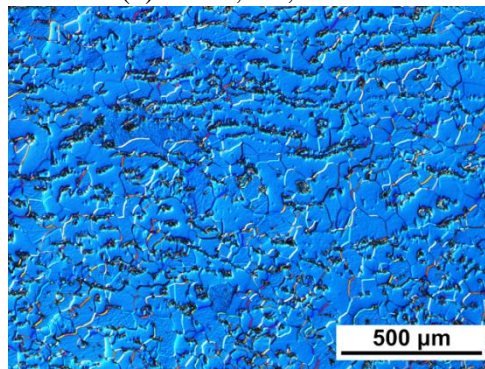
(c) 750°C, 0.12, 10.0s⁻¹



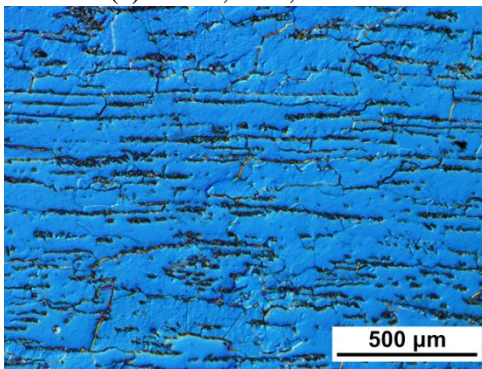
(d) 750°C, 0.6, 10.0s⁻¹



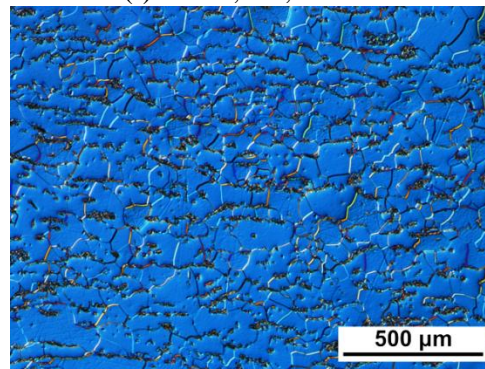
(e) 800°C, 0.12, 10.0s⁻¹



(f) 800°C, 0.6, 10.0s⁻¹



(g) 900°C, 0.12, 10.0s⁻¹



(h) 900°C, 0.6, 10.0s⁻¹

Figure 4.18 Microstructure after isothermal annealing for high strain rate

Table 4.7 Recrystallized fraction after isothermal annealing

Strain Rate	1.0s ⁻¹		10.0s ⁻¹	
	0.12	0.6	0.12	0.6
700°C	-	-	No REX	0.11
750°C	-	-	No REX	0.34
800°C	No REX	1.0	No REX	0.96
900°C	No REX	1.0	No REX	0.99

4.2.2. The stress relaxation curves

The stress relaxation curves in various combinations of temperature and strain rate are shown in [Figure 4.19](#), [Figure 4.20](#), and [Figure 4.21](#). The end point of deformation was set as the initial point of the stress relaxation curves. The initial stress increased with increasing strain, increasing strain rate, and decreasing temperature, in agreement with single hit deformation test results. The kink behavior shown in the curve at a strain rate of 1.0s⁻¹ was not attributed to material origin but to machine effect. Turbulent behavior within the first 1sec of stress-relaxation curve at a strain rate of 10.0s⁻¹ is observed. Possible causes of this turbulent behavior of stress were adiabatic heating and the machine effect.

The temperature of the specimen during deformation is determined by heat generation and heat dissipation. According to the work by Kleber and Sommitsch (Kleber 2004), in which they measured the center and surface temperature of a nickel-based alloy during deformation, the adiabatic temperature change influenced the stress relaxation behavior.

For the present work, as shown in [Figure 4.22](#), the surface temperature gradually changed and was within 10°C of the target temperature in specimens deformed at a strain rate of 1.0s⁻¹. A strain rate of 10.0s⁻¹ resulted in a temperature increase of up to 25°C. As shown in [Figure 4.23](#), the timing of non-monotonic stress variations accompanied the timing of these temperature changes. However, the temperature effect caused by the difference between the maximal and minimal temperature of 25°C seemed limited, so it cannot be concluded that the turbulent behavior was only caused by adiabatic heating.

To investigating the possibility of the variation being due to an artifact related to the equipment, the change of force, the machine stroke, and the diameter change under the high strain rate deformation conditions were plotted in [Figure 4.24](#). Though the machine stroke was well controlled for most the test, a slight oscillation behavior was observed within first second after deformation. For a stroke oscillation of about 10µm the resulting elastic stress would be at most 50MPa. This uncertainty in stress makes it impossible to extract reliable information from the data obtained during the first second. Therefore, the stress relaxation data within the first second was not taken into account for the stress relaxation analysis under high strain rate conditions.

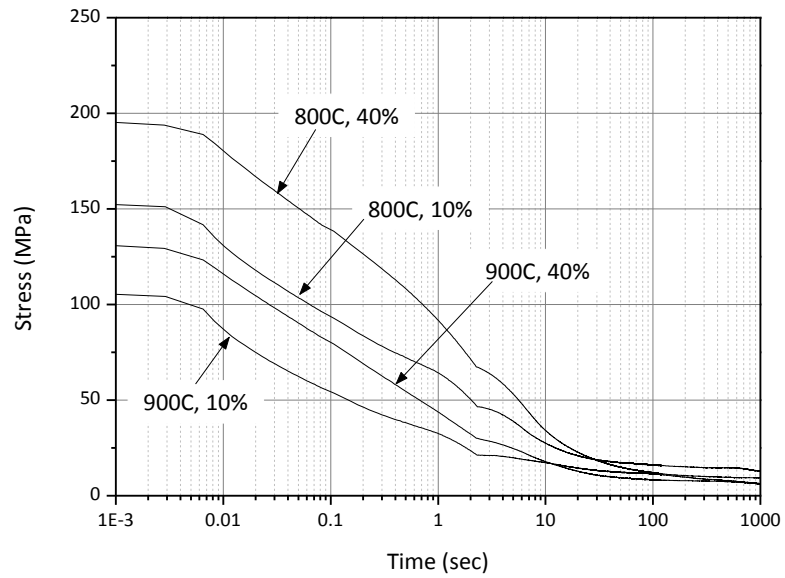


Figure 4.19 Stress relaxation curves for strain rate of $1.0s^{-1}$

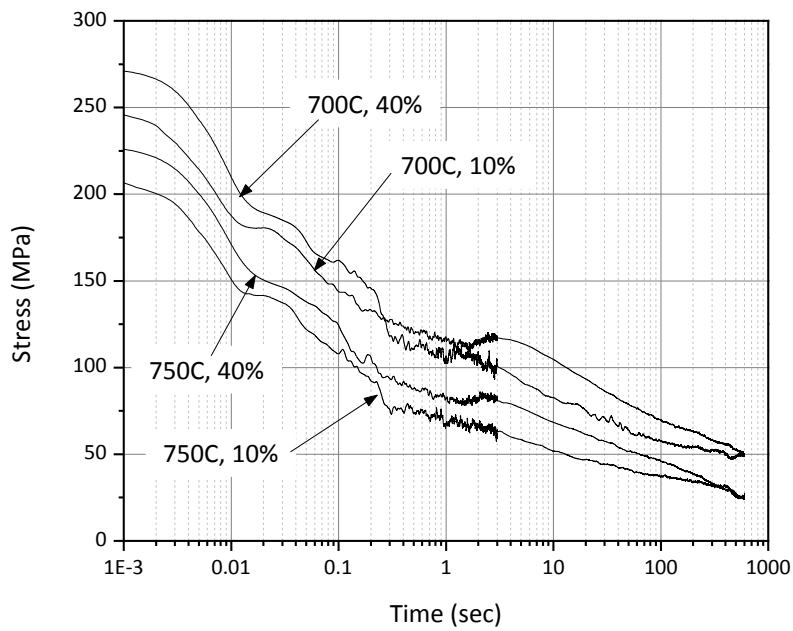


Figure 4.20 Stress relaxation curves for strain rate of $10.0s^{-1}$ at low temperature

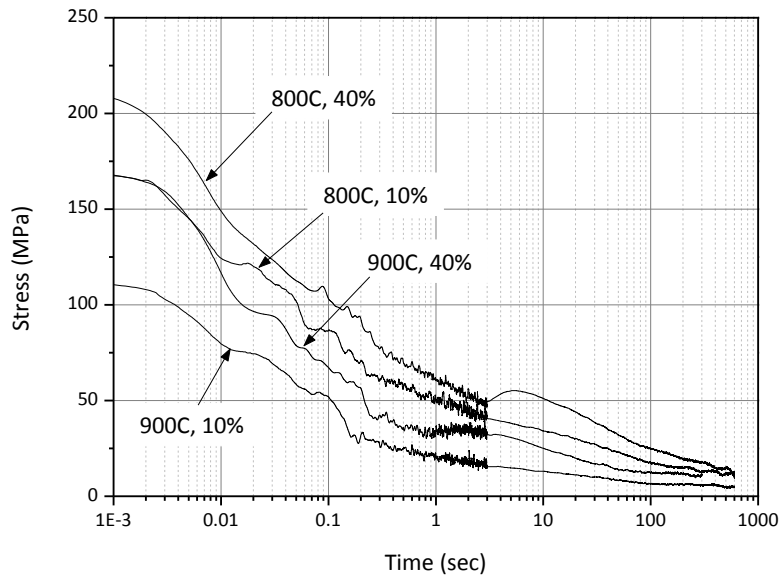


Figure 4.21 Stress relaxation curves for strain rate of $10.0s^{-1}$ at high temperature

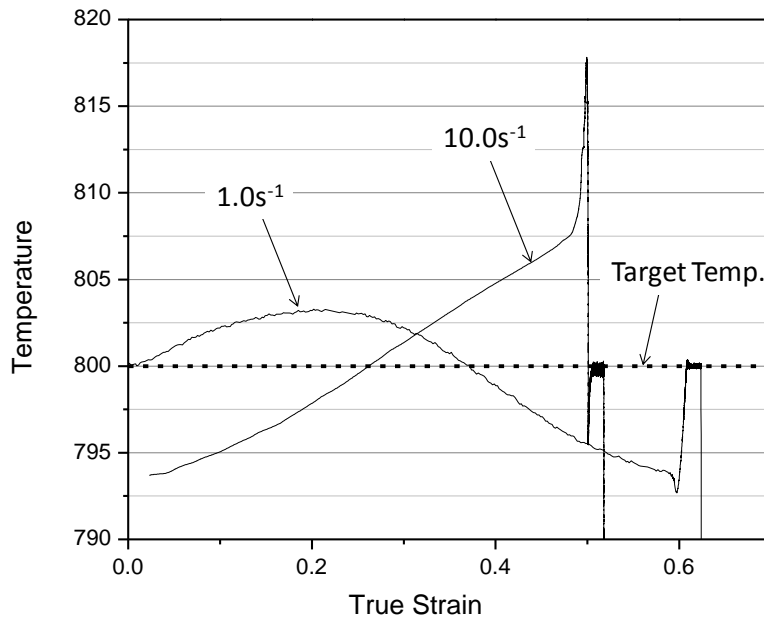


Figure 4.22 Temperature change by adiabatic heating

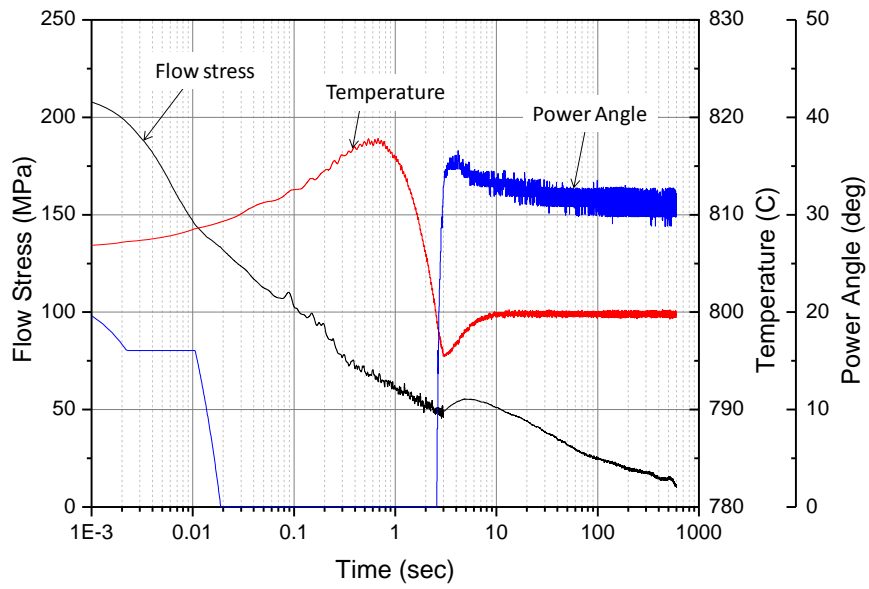


Figure 4.23 Temperature effect on stress relaxation behavior (800°C , 0.6 , 10.0s^{-1})

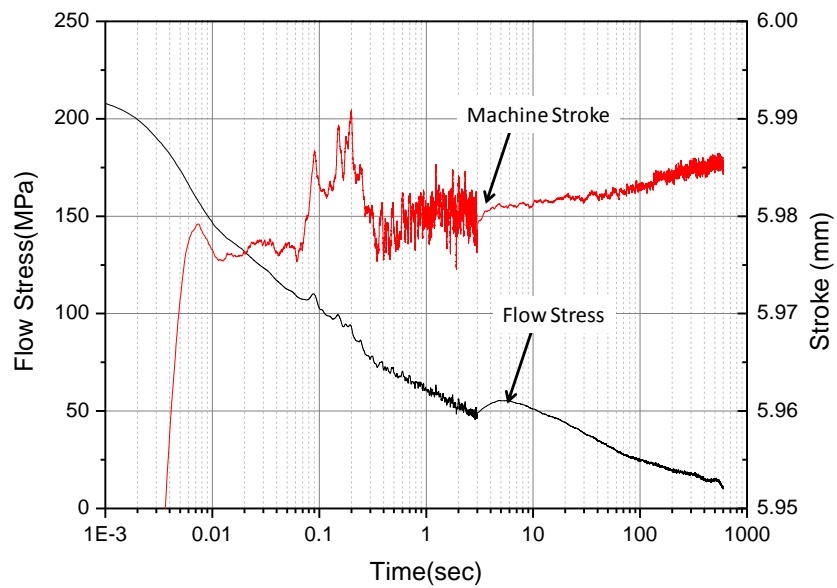


Figure 4.24 The machine effect on stress behavior (800°C , 0.6 , 10.0s^{-1})

4.2.3. Recovery kinetics

Verdier et al. determined the amount of softening by the double deformation test, in which the difference of yield stresses before and after annealing were measured. In this study, since the decrease of stress was measured directly and continuously, instead of the change of yield stress, the internal stress σ_i was described as:

$$\sigma_i = \sigma_{flow} - \sigma_{ss} \quad (4.11)$$

where, σ_{flow} , and σ_{ss} are, respectively, the measured flow stress during isothermal annealing, and the steady state stress of the fully recovered microstructure.

Based on microstructure observation after the stress relaxation test (Table 4.7), it is possible to identify those conditions under which recovery was the main mechanism of softening. Verdier's recovery model, equation (2.25), is applied to such experimental results with U_0 and v_a as parameters. The fitting results are shown in Figure 4.25. The initial part within 1.0sec was not taken into account due to the complications discussed earlier. The part of curve is shown in gray. A dashed-line is used to show the predictions of Verdier's model over the same range. The model showed reasonable agreement with the experimental results. The values of the activation energy U_0 and activation volume v_a deduced from fitting are summarized in Table 4.8. The value of the activation energy, U_0 , was constant 239kJ/mol in all calculations. The values of other constants used in the Verdier's model (equation (2.25)) are summarized in Table 4.9.

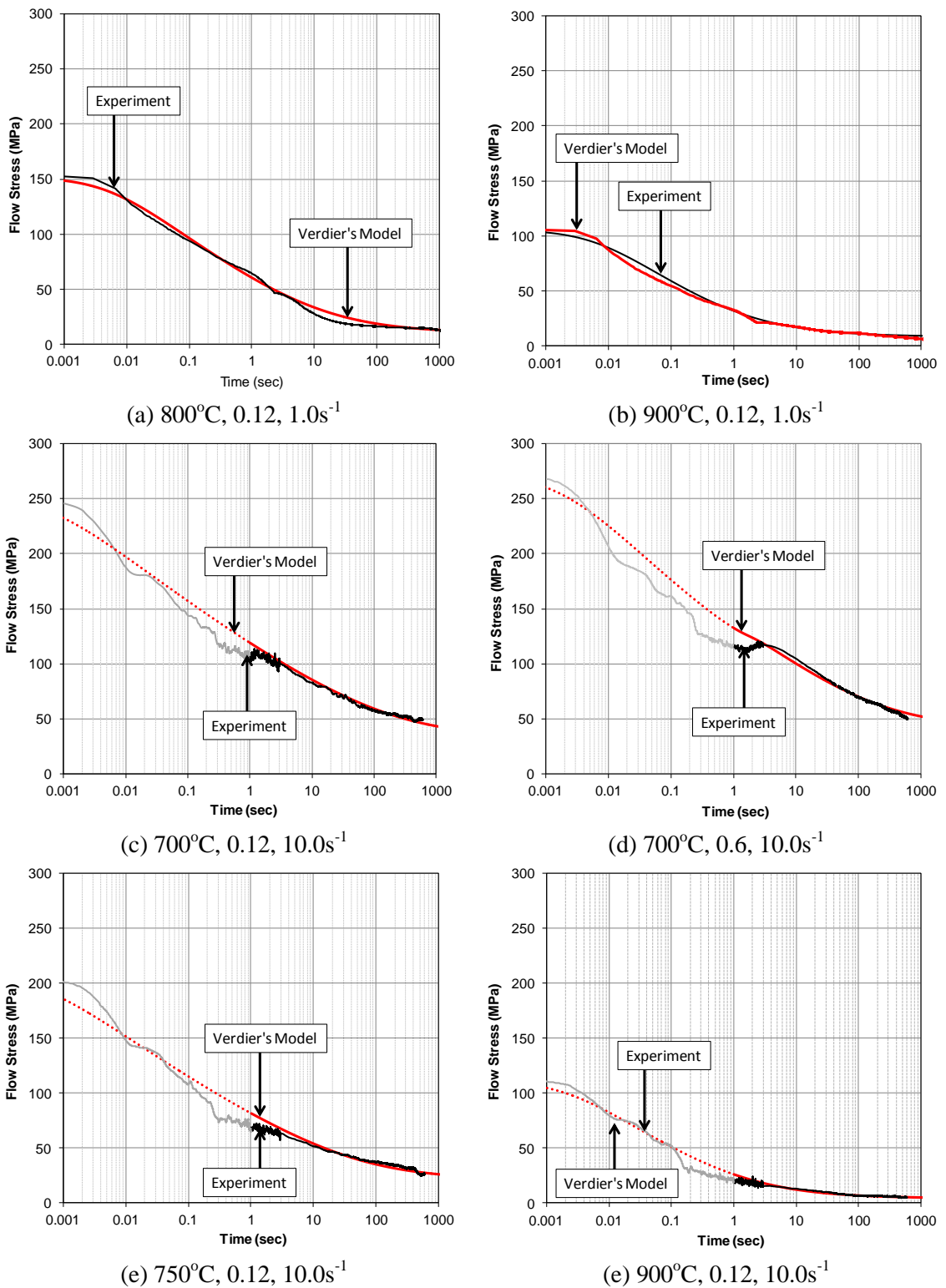


Figure 4.25 Comparison between experiment and the Verdier's model

Table 4.8 Fitted parameters for Recovery

Strain rate	1.0s ⁻¹				10.0s ⁻¹			
	0.12		0.6		0.12		0.6	
Parameter	U_0 [kJ/mol]	v_a [b ³]	U_0 [kJ/mol]	v_a [b ³]	U_0 [kJ/mol]	v_a [b ³]	U_0 [kJ/mol]	v_a [b ³]
700°C	-	-	-	-	239	25	239	21
750°C	-	-	-	-	239	28	(239)	(21)
800°C	239	26	239*	18*	239	27	(239)	(21)
900°C	239	27	239*	20*	239	28	(239)	(21)

“*” indicates that the value was obtained by fitting to the first recovery part of the stress relaxation curve of recrystallized conditions

Table 4.9 The value of constants employed for Verdier's model

α	constant	0.23	
M	Taylor factor	2.73 (for B.C.C metals)	(Rosenberg 1971)
E	Young modulus	$\frac{8}{3}G$	(Verdier 1999)
G	Shear modulus	$G = G_0 \left(1 + \frac{(T - 300) T_M}{T_M \mu_0} \frac{d\mu}{dT} \right)$, $\frac{T_M}{\mu_0} \frac{d\mu}{dT} = -0.81$ $\mu_0 = 6.4 \times 10^4$, $T_M = 1810(K)$ (for α -iron)	(Harold 1982)
k	Boltzmann constant	1.38×10^{-23}	
ν_D	Debye frequency	1.0×10^{13}	(Song 2013)

4.2.4. Recrystallization kinetics

As discussed in section 2.1.6, generally, the softening behavior during isothermal annealing after hot deformation can be divided into three stages. In the first stage, stress decreases linearly with $\log(t)$ as a result of recovery. With the onset of recrystallization, the stress decreases rapidly. This is the second stage of softening. Finally, in the third stage, the softening behavior becomes slower than former stages with the completion of recrystallization, and decreases linearly again.

As shown in [Figure 4.19](#), [Figure 4.20](#), and [Figure 4.21](#), however, the stress dropped rapidly immediately after deformation, and it is difficult to distinguish the three stages of softening behavior. Before recrystallization started, recovery was predominant in softening behavior. So, in the initial part, the recovery model must be in accordance with the experimental result. Then as the softening rate started increasing with the initiation of recrystallization, the recovery model should deviate from the experimental results. Therefore, the recrystallized volume fraction can be calculated based on the difference between the actual stress and that calculated based on the recovery model.

$$f_{rex} = \frac{\sigma_{RCV} - \sigma_{flow}}{\sigma_{RCV} - \sigma_{inf}} \quad (4.12)$$

where σ_{RCV} and σ_{inf} are, respectively, the value of calculated stress by the Verdier recovery model, and the constant value of stress after isothermal annealing.

This procedure was applied to the tests in which the microstructures recrystallized more than 30% after isothermal annealing. For the low strain rate condition, the values of

fitting parameters used in Verdie's model are shown in Table 4.8. These values are indicated by "*" in Table 4.8. On the other hand, for the condition with strain of 0.6 and strain rate of 10.0s^{-1} at high temperature, the fitting parameters for Verdie's model cannot be obtained due to the turbulent behavior of stress relaxation curve at short times. Therefore, the value of the fitting parameters obtained from deformation at a strain rate of 10s^{-1} to a strain of 0.6 at 700°C , were applied to those conditions. Those values are showed in round brackets in Table 4.8. The Avrami type empirical equation (equation (4.12)) was applied to the recrystallized fraction calculated from the experiment to obtain the Avrami exponent and 50% recrystallization time. The recrystallization curves that were calculated from the stress relaxation data are shown in Figure 4.26. The values of the Avrami exponent and 50% recrystallization time are shown in Table 4.10.

Here, the values of Avrami exponent were smaller than the typical values of $n \sim 2.0$. The values were also somewhat smaller than those obtained from optical observation. Furthermore, the values of $t_{0.5}$ and n appear to depend on temperature and strain rate.

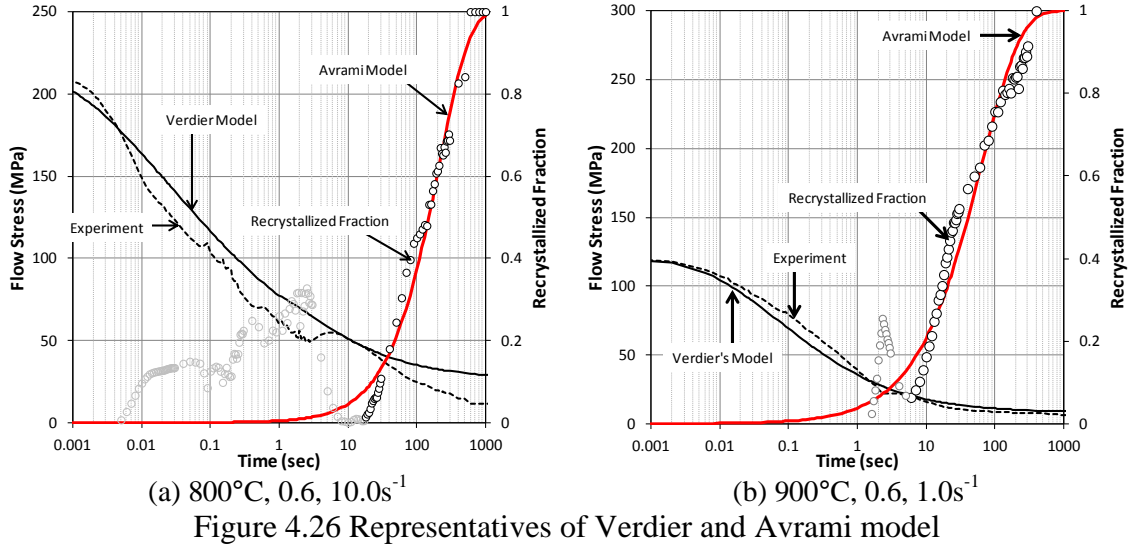


Table 4.10 Avrami exponent and 50% recrystallization time form stress relaxation test

Temperature	800°C	900°C	
Strain rate	10.0s ⁻¹	1.0 s ⁻¹	10.0 s ⁻¹
<i>t</i> _{0.5}	150	41.0	34.5
<i>n</i>	0.78	0.73	0.93

Chapter 5. Discussion

In this chapter the mechanisms and characteristics of kinetic behaviors which were observed in the experimental results are discussed. In section 5.1 the mechanism of austenite microstructural change will be discussed. Section 5.2 and 5.3 will cover the characteristics of ferrite recrystallization nucleation. The recovery kinetics of ferrite will be discussed in section 5.4. Discussion of the recrystallization kinetics will be presented in section 5.5.

5.1. Austenite microstructure evolution

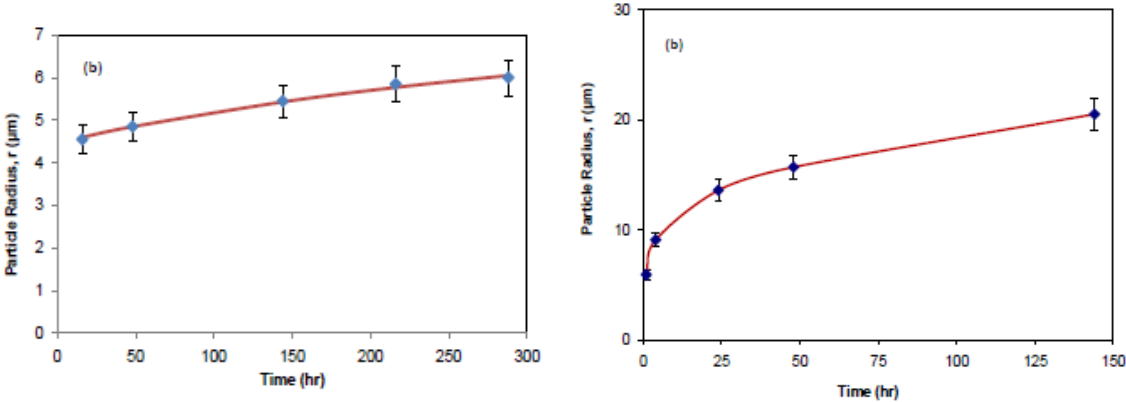
According to section 4.1.6, the austenite volume fraction in [Figure 4.15](#) corresponded well to the prediction of the Thermocalc calculation ([Figure 3.1](#)). The spatial distribution of the austenite particles was governed mainly by the solidification process and subsequent deformation as pointed out in section 4.1.6.

Zhou et al. investigated austenite particle coarsening in a material with the same chemical composition as the one used here. The alloy of this project was reheated into the delta region and the particle size and volume fraction were measured as a function of isothermal holding time (Zhou 2010, 2011). Zhou et al. observed that the volume fraction only changed during the first few minutes. After that initial period, the volume fraction was essentially constant and the only change to take place in the microstructure was the coarsening of the austenite particles ([Figure 5.2](#)). Zhou et al. concluded that the coarsening process was controlled by long range diffusion of substitutional elements, such as Mn, and Al ([Figure 5.2](#)). Given the slow kinetics of coarsening, it is reasonable

to assume that the austenite distribution doesn't change much during the time range of hot deformation and subsequent annealing used in this project.

According to Gove and Charles, the hardness of austenite at high temperature is greater than that of Ferrite in 0.2wt%C-steel and nominally pure iron (Gove 1974). Assuming this tendency can be applied to this model alloy, ferrite is more easily deformed than austenite. To a first approximation, the present system resembles an ideal system in which the soft-phase (ferrite) deforms and the hard particles (austenite) do not. This is supported by the fact that dislocations and low angle grain boundaries (LAGBs) were formed in the vicinity of austenite particles ([Figure 4.9](#)).

With this in mind, the change in austenite distribution in the single hit deformation experiment can be understood as follows. The volume fraction of austenite was determined in homogenizing process, and the fraction didn't change during subsequent coarsening. Since, the ferrite matrix bore the majority of the plastic deformation, the main change was in terms of the distribution (spacing) of the austenite particles within the ferrite matrix. Hence, the stress relaxation behavior was primarily attributed to ferrite microstructure evolution under the deformation conditions employed in this work.



(a) 850°C (b) 1060°C
Figure 5.1 Austenite particle radius change as a function of time at different holding temperature (Zhou 2010)

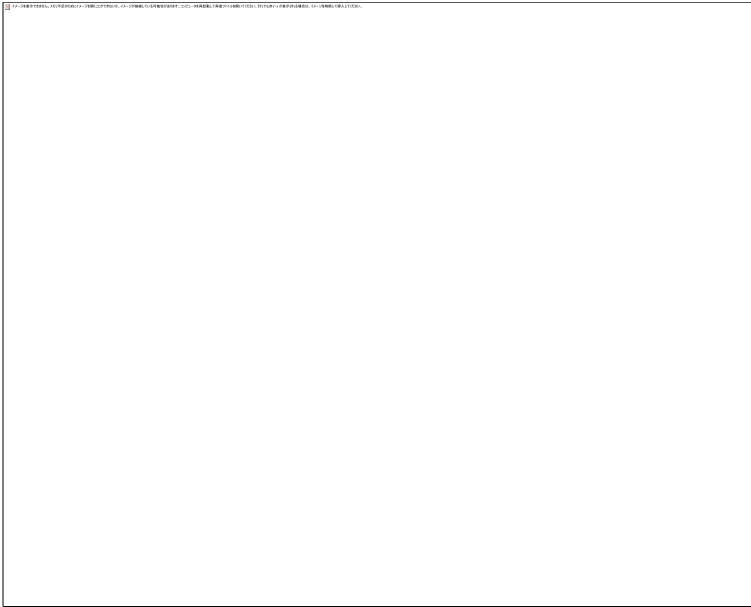


Figure 5.2 Schematic illustration of the mechanism of austenite grain growth (Zhou 2010)

5.2. Ferrite Nucleation Mechanism

According to the microstructure observations (section 4.1.4), recrystallized grains can be observed within short annealing time ([Figure 4.9](#), [Figure 4.10](#), [Figure 4.11](#), and [Figure 4.12](#)). It is necessary to clarify whether the recrystallized grains formed by dynamic recrystallization or static recrystallization. Generally, dynamic recrystallization in high stacking fault energy materials (BCC iron or Aluminum) is less likely to occur compared to low stacking fault energy materials (FCC iron or Copper). Dynamic recrystallization can take place by three different mechanisms, discontinuous dynamic recrystallization (DDRX), continuous dynamic recrystallization (CDRX), and geometric dynamic recrystallization (GDRX).

The GDRX requires very high strain level as shown for example, in the work of Kassner on high purity Aluminum where a strain of $\varepsilon > 3.0$ was needed to mechanically break the old grains into small grains surrounded by HAGB (Kassner 1989). Because the strain level in the present work ($0.1 < \varepsilon < 0.6$) was much smaller than that, it can be concluded that GDRX could not occur.

Tsuji et al. reported the occurrence of DDRX of ferrite in interstitial free iron deformed to a strain of 0.8 (Tsuji 1997, 1998a). The possible range of the Z parameter is $Z \leq 1.0 \times 10^{11}$ which is smaller than the range of the Z parameter in the present project. Yagi et al. investigated 18wt% Cr stainless steel deformed to a strain of 0.8, and concluded that the limit of the Z parameter is $Z \leq 1.0 \times 10^{14}$ for the temperatures under 800°C (Yagi 2000). For the CDRX, Mehtonen et al. reported a higher limit of the Z parameter, which is

9.0×10^{14} , for the occurrence of dynamic recrystallization in 16wt% Cr stainless steel deformed to a strain of 0.6 (Mehtonen 2013). Since the range of the Z parameter in this project is close to these suggested Z parameter ranges, dynamic recrystallization may occur.

In order to prove the occurrence of discontinuous dynamic recrystallization it is necessary to show two pieces of evidence. First, the new grain must have a different orientation from the surrounding grains, or in other words, be surrounded by HAGB. And second, the new grains must contain substructure, such as LAGBs and dislocations (Tsuji 1998b). The deformation condition at a strain rate of 1.0 s^{-1} and at 900°C in the present work was a Zener parameter of 6.6×10^{14} , which is closest to the value of the limit suggested by Mehtonen and Yagi. The optical images indicated equiaxed grains or subgrains (Figure 4.5), but those were found to be subgrains surrounded by LAGB by the EBSD analysis (Figure 4.9(e)). Small grains observed Figure 4.13 were surrounded by both HAGB and LAGB and had a clean structure. From more macro scale point of view, another characteristic of discontinuous dynamic recrystallization is that the necklace structure of recrystallized grains appears on old grain boundaries (Tsuji 1998b). However, the necklace structure was not observed in this model alloy by optical and EBSD observation. Therefore discontinuous dynamic recrystallization did not occur in the model alloy under the deformation conditions employed for this project.

The recrystallized grains shown in Figure 4.13 indicate the characteristics of SIBM. The grain boundaries of new grains consisted of LAGBs and HAGBs. The HAGBs showed bulging out into the neighboring deformed grain and a characteristic high curvature. The

orientation of the new grains is similar to that of the old grains, which are only separated from the old grains by LAGBs. Similar characteristics are observed in the newly formed grains in early stages of CDRX. However, some characteristics of CDRX grain were missed, e.g. as mentioned above, no substructure was contained in the grains in [Figure 4.13](#).

Ouchi and Okita examined recrystallization kinetics by means of microstructural observation in 1.8wt% Al steel hot-deformed under similar conditions to this work. According to their result, the new grains seemed statically recrystallized and most of recrystallized grains were observed straddling the old grain boundaries. Their result can support the result that recrystallized grains observed in our model alloy were attributed to static recrystallization. Therefore, it can be concluded that the grains observed after short annealing times were attributed to not dynamic recrystallization but static recrystallization under the deformation conditions employed in this project.

5.3. Ferrite Static Recrystallization Nucleation Kinetics

From the microstructure observation, the recrystallized grains indicated the characteristics of SIBM. Bailey and Hirsch proposed the classical SIBM recrystallization model (Bailey 1962). The SIBM takes place when the driving force due to the stored energy of dislocations is sufficient to overcome the boundary curvature, $2\gamma_{BE}/r$, where γ_{BE} is the boundary energy and r is the radius of the subgrain. This leads to a simple expression for the critical size of the recrystallization nucleus:

$$r_c = \frac{2\gamma_{BE}}{E_D(t)} \quad (5.1)$$

where r_c is the critical radius that a subgrain needs to reach before the grain boundary is able to bulge into the neighbouring grain, and $E_D(t)$ is the instantaneous value of stored energy of deformation. The critical radius will increase with time as $E_D(t)$ decrease due to recovery. Therefore, the occurrence of nucleation depends on the competition between recovery and recrystallization.

Substituting equation (2.4) and (2.24) into equation (5.1), the critical radius can be described as:

$$r_c = \frac{4\gamma_{BE}\alpha^2 M^2 G}{\sigma_i(t)^2} \quad (5.2)$$

where $\sigma_i = \sigma_{flow} - \sigma_{ss}$, σ_{flow} , and σ_{ss} are, respectively, the measured flow stress during isothermal annealing, and the steady state stress of the fully recovered microstructure. The constant α depends on the material and is, of the order of 0.2, M is the Taylor Factor, and G is the elastic shear modulus. A value of $\gamma_{BE}=0.617\text{J/m}^2$ for α -iron (Humphreys 2004) was employed for the calculation. And the values of the other parameters were the same values described in [Table 4.9](#).

The comparison between intragranular subgrain size, which was measured from single-hit deformation results (shown in [Figure 4.8](#)), and the rough estimation of critical radius by means of flow stress data obtained from stress relaxation test, is shown in [Figure 5.3](#). [Figure 5.3\(a\)](#) shows the result at 800°C , and strain rate of 10.0s^{-1} , and [\(b\)](#) shows the result

at 900°C, and strain rate of 1.0s⁻¹. The estimated critical radius rapidly increased with time due to the rapid progress of recovery. The measured subgrain size seems smaller than critical radius in both cases.

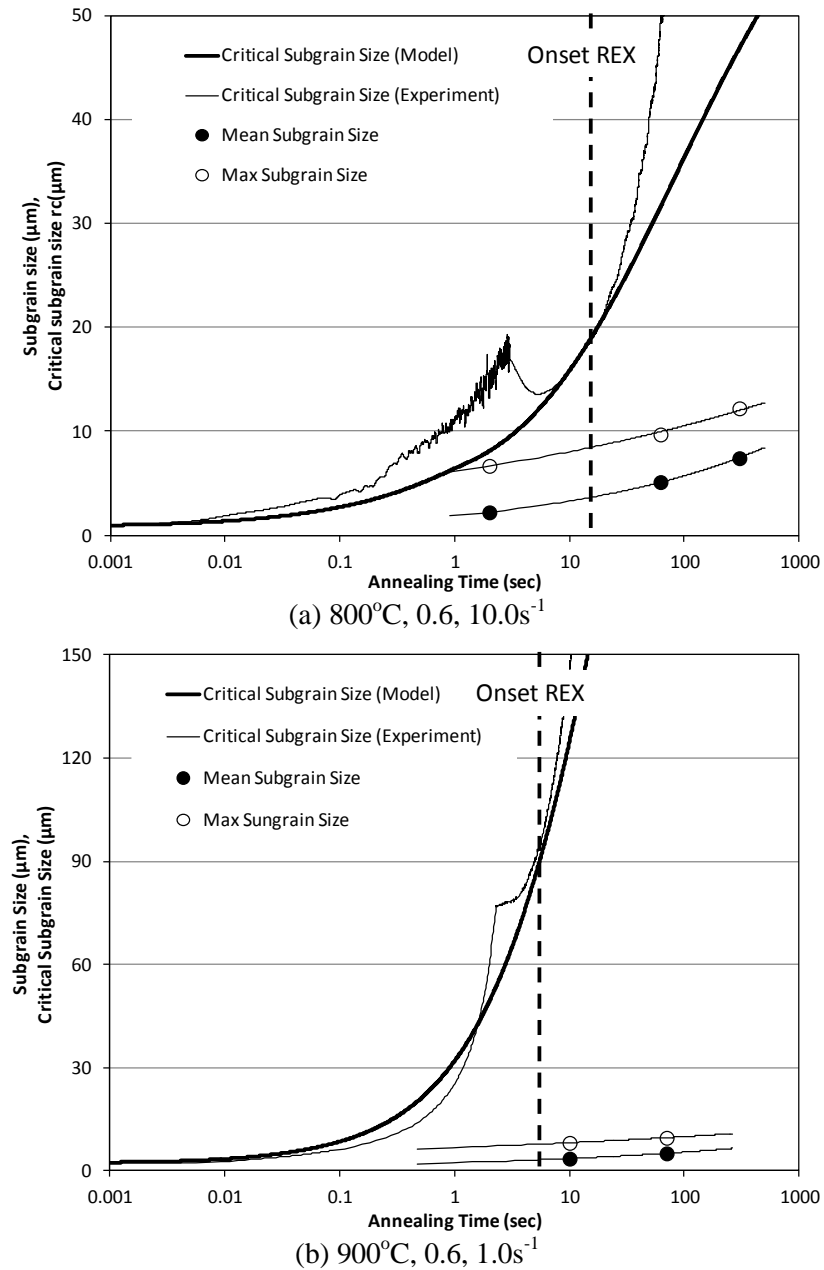


Figure 5.3 The comparison between the measured intragranular subgrain size and the estimated critical radius

The subgrain size was measured in the center of ferrite grains to avoid counting recrystallized grains and small austenite particles as subgrain boundaries. The stress relaxation behavior provided the restoration kinetics occurring in the whole specimen. Due to the large initial ferrite grain size ($\approx 200\mu\text{m}$), the fraction of grain boundary in the specimen must be limited. Hence the restoration kinetics measured in the stress relaxation test seemed to represent the dissociation and rearrangement of dislocation in the center part of ferrite grains. Therefore, [Figure 5.3](#) can be interpreted to suggest that subgrains in the center of ferrite grains could not reach the critical radius, so that recrystallization did not occur in the center part of ferrite grains. In fact, no new grains were observed to nucleate from the center of ferrite grains in either the low magnification micrographs ([Figure 4.10](#), [Figure 4.11](#), and [Figure 4.12](#)), or in the high magnification micrographs ([Figure 4.5](#), and [Figure 4.9](#)).

As discussed in section 4.2.1, new grains recrystallized in the vicinity of old grain boundaries and austenite particle. As shown in [Figure 4.9 \(b\), \(d\) and \(e\)](#), dislocations and LAGBs were denser in the vicinity of ferrite grain boundaries and austenite grains compared to the center part of ferrite grains immediately after deformation. After isothermal annealing the dislocations and LAGBs in the center of ferrite grains disappeared, while those in the vicinity of ferrite grain boundaries and austenite grains still remained ([Figure 4.9 \(a\), and \(c\)](#)). Hence the local dislocation density in the vicinity of grain boundaries and austenite grains should be high, so that the stored energy of deformation is high in those areas. Due to the local high stored energy, the critical radius in the vicinity of boundaries could be smaller than that in the center of ferrite grain.

Consequently, the subgrains around boundaries and austenite grains could reach the critical radius, so that new grains could start growing.

5.4. Ferrite Recovery Kinetics

The relationship between activation volume and hot deformation conditions, such as strain, temperature, and strain rate is shown in Figure 5.4. According to Figure 5.4 (a), the activation volume increased with increasing temperature. As mentioned in section 2.3.1, the activation volume is directly proportional to the activation length. The activation length can depend on the jog separation and on the climb and glide motion of the dislocation.

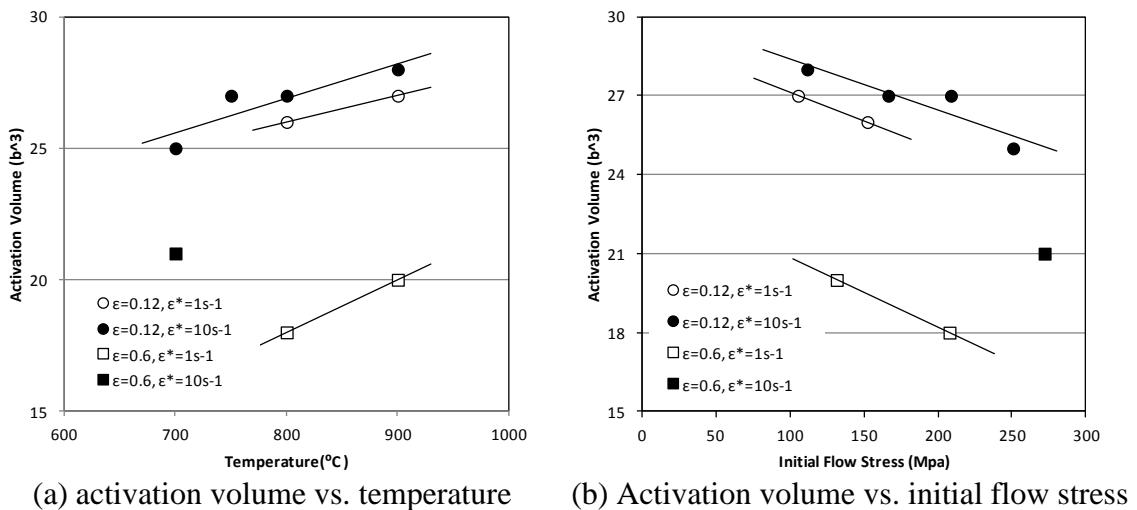


Figure 5.4 Relationship among activation volume, temperature, initial flow stress, and strain rate

It is known that the activation length has an Arrhenius type temperature dependence when the activation length is assumed to be determined due to only the jog separation (Gibbs 1971), so that the activation length will be larger at higher temperatures. Hence, the activation volume will increase with increasing temperature. If it is assumed that the glide and climb of dislocation dominate dislocation annihilation, the activation length can be formulated by (Nes 2004):

$$l_a = b \left(1 + \frac{l_g}{l_c} \right) \quad (5.3)$$

where l_g is the glide length and l_c is the climb length. The equilibrium dislocation density decreases with increasing temperature. Therefore, the activation length will increase with increasing temperature (Smith 2004). According to [Figure 5.4 \(a\)](#), it can be concluded that the relationship between activation volume and temperature agree with this tendency.

Concerning the effect of strain and strain rate, the high strain and high strain rate lead to high dislocation density, so that the activation volume should decrease with increasing strain and strain rate. This tendency for the strain is seen in [Figure 5.4](#). In contrast, the activation volume slightly decreased with increasing strain rate. One possible reason was presented by Smith (2004) who argued that the segregation of solute atoms, such as carbon, can reduce the jog velocity under low strain rate conditions. Therefore, increasing of the strain rate can change the value of the activation volume in both directions. However, the carbon content in the steel which they used was four times higher than this model steel, and the strain rates which they employed were 0.01s^{-1} - 0.6s^{-1} , while those in this project were 1.0s^{-1} and 10.0s^{-1} . It is difficult to conclude if the strain

rate effect observed here is consistent with Smith's explanation. Clarifying the effect of strain rate requires more detailed work.

In terms of the magnitude of the activation volume, typical values for BCC materials are reported in the range of 5 b^3 - 100 b^3 . And the values of the low carbon steel deformed and annealed in the ferrite region are reported in the range of 28 b^3 - 36 b^3 by Martinez-de-Guerenu, et al (Martínez-de-Guerenu 2004), and 10.5 b^3 - 17.7 b^3 (Smith 2004). The range of values of the activation volume for this model alloy was 18 b^3 - 28 b^3 . According to the discussion above, the value of activation energy can be affected by not only the deformation conditions but also the chemical composition. The experiment carried out by Martinez-de-Guerenu involved cold rolling and non-isothermal annealing with a slow heating rate; as a result it is difficult to make a direct comparison with the present results. Comparison with the data of Smith under similar conditions is shown in Table 5.1. The values of activation energy by Smith were smaller than the current work in spite of lower strain and strain rate condition in Smith's work. It can be concluded that the effects of temperature and carbon contents are stronger than those of strain and strain rate.

Table 5.1 Comparison of deformation conditions between current work and Smith's work (Smith 2004)

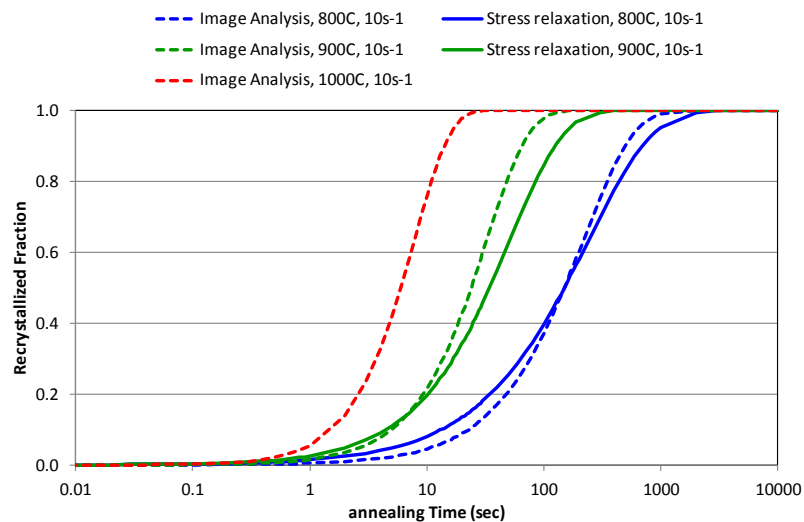
Temperature (°C)	Strain	Strain rate (s ⁻¹)	Activation Energy (kJ/mol)	Activation Volume (b ³)	
550	0.15	0.5	231	17.1	(Smith 2004)
550	0.5	0.6	226	17.7	(Smith 2004)
700	0.12	1.0	239	25.0	(Present work)
700	0.6	1.0	239	21.0	(Present work)

5.5. Ferrite Recrystallization Kinetics

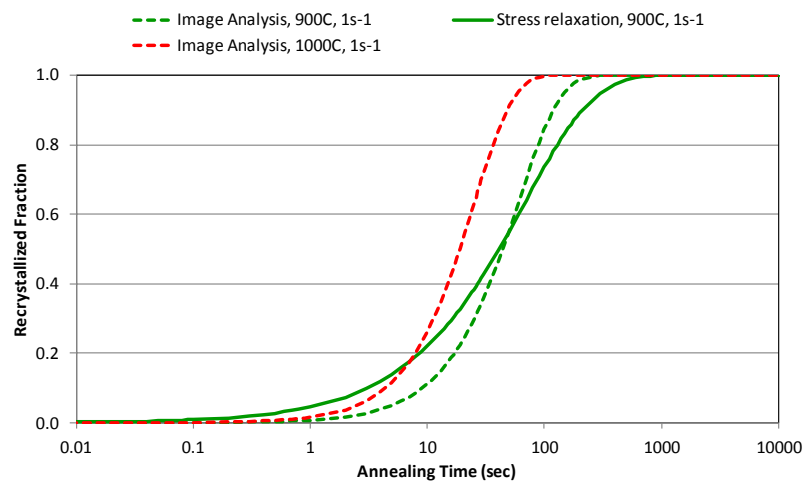
The recrystallization kinetics of the model alloy was studied by two different methodologies, microstructure observation and stress relaxation. Two important parameters for recrystallization, the 50% recrystallization time, $t_{0.5}$, and the Avrami exponent, n , were obtained by using the same Avrami type empirical equation. The values of both quantities were summarized in [Table 4.6](#) and [Table 4.10](#). Avrami plots obtained by image analysis and stress relaxation are compared in [Figure 5.5](#). The stress relaxation test showed slightly slower recrystallization kinetics than the microstructure observation. However, the range of values of the two parameters shows reasonable agreement. This justifies the slow recrystallization kinetics of the model alloy.

The values of $t_{0.5}$ and n obtained using both methods are plotted in [Figure 5.6](#) and [Figure 5.7](#). According to equation (2.29), the value of U_{REX} can be calculated from the slope of the Arrhenius plot of $t_{0.5}$ and temperature as shown in [Figure 5.6](#). The values of U_{REX} obtained from [Figure 5.6](#) are 180.9kJ/mol for a strain rate of 10.0s⁻¹, and 113.7kJ.mol for

strain rate of $1.0s^{-1}$. These values are smaller than the values reported by other authors, 221kJ/mol for high Cr ferritic stainless steel (Mehtonen 2013), 280kJ/mol for high purity ferritic iron (Glover 1973), and 290kJ/mol for 3wt% Si ferritic steel (Humphrey 2004 after Speich and Fisher 1966). This shows that recrystallization progresses much slower in this model alloy compared to other kinds of steel.



(a) Strain rate of $10s^{-1}$



(b) Strain rate of $1s^{-1}$

Figure 5.5 Recrystallized fraction by means of two different methods.

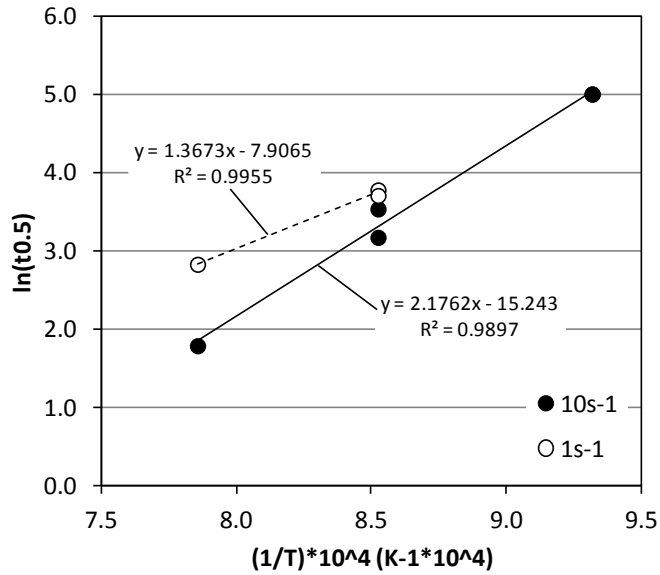


Figure 5.6 Dependence of 50% recrystallization time $t_{0.5}$ on temperature

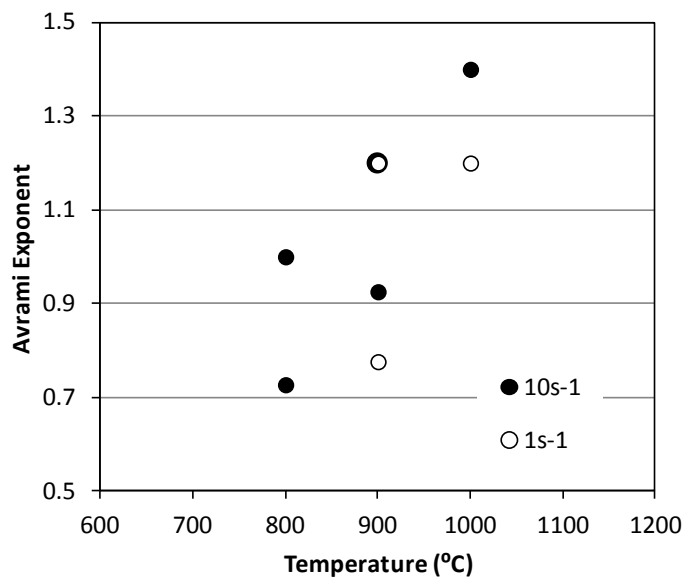


Figure 5.7 Dependence of Avrami exponent n on temperature

It is seen that the Avrami exponent increased with temperature ([Figure 5.7](#)). Generally, the value of Avrami exponent is in the range from 1.0 to 2.0. In this study, the range was slightly small, from 0.7 to 1.4. Additionally, the stress relaxation result for the specimen deformed to strain 0.6 at 900°C and strain rate of 1.0s⁻¹ ([Figure 4.26 \(b\)](#)) shows that the recrystallization rate slowed down after approximately 50% recrystallization. Therefore, it can be concluded that this model alloy has slow kinetics of recrystallization compared with other ferritic steels.

There are two possible reasons for slow kinetics of recrystallization. The first reason is heterogeneity in the microstructure and texture. Sinclair et al. and Oyarzábal et al. carried out the texture analysis of ferritic steel (12wt% Cr AISI ferritic stain less steel, and low carbon steel, respectively) cold-deformed followed by isothermal annealing (Sinclair 2005, Oyarzábal 2008). These two works reached the same conclusion that the γ -fiber grains recrystallize faster than α -fiber grains. Oyarzábal quantitatively evaluated the stored energy of these two types of texture by means of normalized image quality distribution analysis of EBSD, and presented that the γ -fiber grains contained higher stored energy than the α -fiber grains. Therefore, this heterogeneity of energy storage leads to the γ -fiber grains recrystallizing first, and then the recrystallization rate decelerates as the α -fiber grains start recrystallization. The deceleration behavior of the recrystallization rate in the current model alloy ([Figure 4.26 \(b\)](#)) may be caused by this mechanism, but more detailed investigation is required for confirmation.

Tsuji et al. examined the effect crystallographic orientation on the recrystallization by means of single crystals of 18wt% Cr ferritic stainless steel applied compression

deformation (Tsuji 1998b). The above work used a strain of 0.8 at 1273K or 1173K at a constant strain rate of 10.0s^{-1} , and specimens were isothermally annealed at 1073K. In each test, the compression direction was parallel to a given orientation in the crystal. The above work showed that the [001] and [111] crystals were hard to recrystallize. In particular, the [001] crystals showed no recrystallization. The unrecrystallized grains observed in this model alloy after annealing at 800°C for 60 sec (Figure 4.12 (b)) indicated approximately [001] and [111] orientation, and those after 300 sec annealing (Figure 4.12) indicated almost [001] orientation. Therefore, such orientation dependency of recrystallization in ferrite can retard recrystallization.

The second reason for slow recrystallization kinetics is the competition with recovery. The relative contributions of recovery and recrystallization to restoration were estimated from the results of stress relaxation test. For the comparison, all quantities were normalized with respect to their initial values after deformation:

$$\frac{E}{E_{ini}} = \frac{\rho}{\rho_{ini}} = \frac{\sigma^2}{\sigma_{ini}^2} \quad (5.4)$$

where E_{ini} , ρ_{ini} , and σ_{ini} are initial stored energy, initial dislocation density, and initial flow stress, respectively. The values of flow stress at each event shown in Figure 5.8 were substituted into a variable σ and then E/E_{ini} and ρ/ρ_{ini} were estimated. The values of σ_{srex} and σ_{inf} represent the stress at the recrystallization starting point and the constant value at stress in steady state, respectively.

The result of this comparison is shown in [Figure 5.9](#). Recovery kept progressing in unrecrystallized grains after recrystallization was initiated, so that it is difficult to separate the effect of recovery and recrystallization. Therefore, the contribution of recrystallization was shown as the maximum value. Surprisingly, the result indicated that more than 95% of the stored energy was consumed by recovery. This indicated the fact that the strong intensity kinetics of recovery can retard recrystallization. The energy consumption by recovery at 800°C is smaller than that at 900°C. This fact agrees with the temperature effect of recovery kinetics discussed in section 5.4.

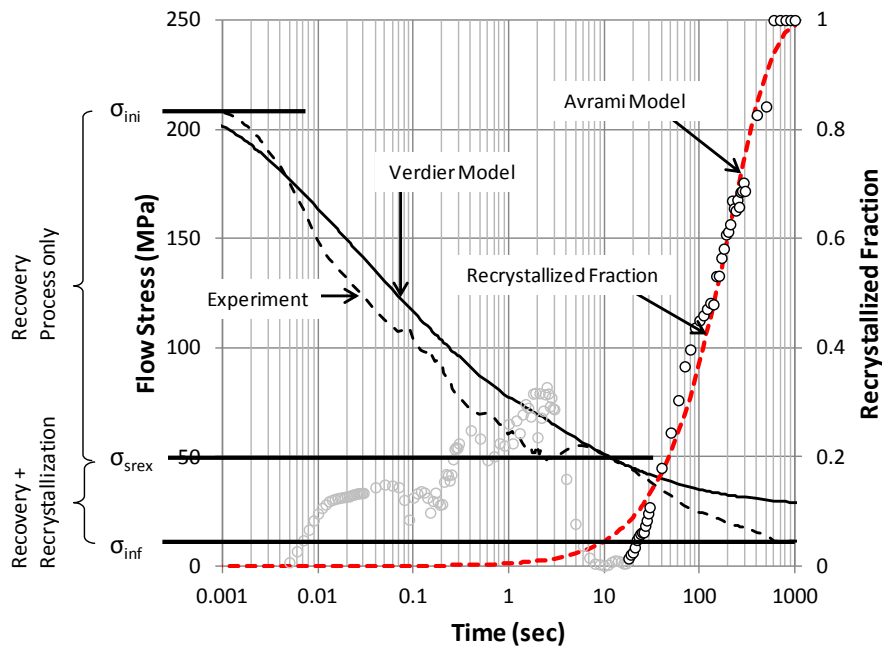


Figure 5.8 An example of the stress for the kinetics events during stress relaxation test (800°C, 0.6, 10.0s⁻¹)

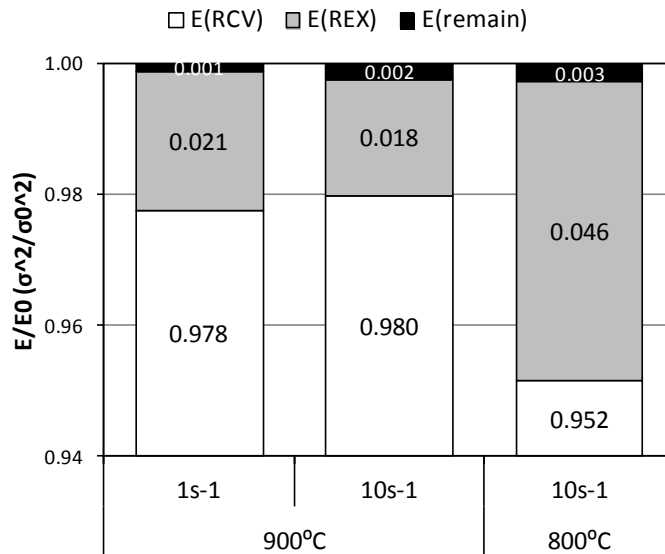


Figure 5.9 Contribution of recovery and recrystallization on restoration during stress relaxation test for different temperature and strain rate

As discussed in section 5.3, the critical radius for recrystallization increased rapidly and subgrains could not start recrystallizing in the center of grains (Figure 5.3). Therefore, the nucleation sites were limited to be in the vicinity of grain boundaries and austenite grains.

Regarding growth rate, the velocity of the recrystallization front V_{REX} can be expressed as:

$$V_{REX} = M_b \cdot P_{REX} \quad (5.5)$$

where M_b and P_{REX} are the mobility of the grain boundary and the driving pressure for recrystallization, respectively. The driving pressure can be described as

$$P_{REX} = (E_D - P_r) = \left(\alpha \rho G \mathbf{b}^2 - \frac{2\gamma_{BE}}{r} \right) \quad (5.6)$$

where E_D is the stored energy of deformation, P_r is the opposing pressure by the curvature of recrystallized grain, γ_{BE} is the boundary energy, and r is the radius of recrystallized grains. The symbols α , ρ , G , \mathbf{b} have the same meaning as before. The dislocation density decreases with the progress of recovery, so that the driving pressure for the growth of the recrystallizing grains decreases with time. As shown in Figure 4.9 (b) and (c), the dislocations in the center of the ferrite grain almost disappeared after 60sec, so that the driving pressure becomes very small. Therefore, recrystallization should be retarded.

Chapter 6. Conclusion

Two types of experiments, the single hit hot compression test and the stress relaxation test, were performed to investigate the microstructure evolution of a model steel, in which a two-phase mixture of ferrite and austenite exists over a wide temperature range including that temperature range typically used for hot-rolling. The temperature and strain rate of deformation were varied from 700°C to 1000°C, and 1.0s^{-1} to 10.0s^{-1} , respectively. The emphasis of this work was the quantification of recovery and recrystallization kinetics of the material during hot deformation and following isothermal annealing. The following results were obtained.

The volume fraction of austenite did not change during hot deformation and subsequent annealing in this work due to the slow coarsening rate of the austenite particles which is controlled by the long range diffusion of substitutional elements, such as Al and Mn. The main change of austenite microstructure was in terms of the spacing of the austenite particles within the ferrite matrix. The ferrite matrix bore the majority of plastic deformation due to the difference of hardness between ferrite and austenite and as a result, deformation reduced the spacing of the particles in the thickness direction. The kinetics behavior observed from the stress behavior was primarily attributed to ferrite microstructure evolution under the deformation conditions employed in this work.

The stress-strain curve of the model alloy behaved as a typical dynamic recovery type of material at temperatures between 800°C and 1000°C, and strain rates of 1.0s^{-1} and 10.0s^{-1} .

The activation energy of the dynamic recovery process in the model alloy was determined as 335kJ/mol.

Well-defined subgrains developed due to dynamic recovery and were clearly observed by DIC under most deformation conditions in this work. The subgrain size depended primarily on flow stress. The subgrains coarsened during the static recovery process. Recovery continued in the unrecrystallized grains even after the onset of recrystallization elsewhere in the material.

A small number of nuclei were observed in the short time after hot deformation. According to metallographic and EBSD observations, those nuclei showed the characteristics of SIBM. Those nuclei were attributed to static recrystallization rather than to dynamic recrystallization.

The recrystallization could not occur in the center of the ferrite grains, because dislocations there disappeared rapidly due to the strong rate of recovery. Ferrite grain boundaries and austenite particles provided the most potent recrystallization nucleation sites due to higher misorientation gradients and slower recovery in the vicinity of these areas.

The recovery kinetics in this model alloy was investigated using the stress relaxation test over a range of temperatures, strains, and strain rates. Verdier's recovery model has been successfully applied to the experimental stress relaxation data. The activation volume varied with temperature and strain and, to a much lesser extent, with strain rate. The

temperature effect on the activation volume was interpreted in terms of a rate controlling process involving thermally activated jog separation and glide and climb of dislocations.

The apparent activation energy of recrystallization kinetics in this model alloy was determined as 180kJ/mol for a strain rate of 10.0s^{-1} , and 114kJ/mol for a strain rate of 1.0s^{-1} . These were smaller than the reported values in other types of ferritic steels. There are two possible reasons for the slow kinetics of recrystallization. The first reason is the heterogeneity of the microstructure and texture in the material. The deceleration of the recrystallization rate observed in the stress relaxation result inferred the effect of a heterogeneous stored energy distribution associated with the texture of the present material. The EBSD analysis confirmed the fact that [111] and [001] grains, which are hard to recrystallize, remained unrecrystallized after annealing. The second reason is the competition between recrystallization and recovery. The quantitative estimation of consumed energy by recovery and recrystallization suggest a strong intensity of recovery kinetics in the model alloy. Such a strong intensity of recovery kinetics could retard recrystallization due to reduced nucleation sites and lower driving pressure for grain growth.

Chapter 7. Bibliography

Aretxabaleta, Z., Pereda, B., Parker, S. V., and Lopez, B. 2012. Static Softening Behavior in High Aluminum Steels. *Materials Science Forum*, 706-709, 2764-2769.

Bailey, J. E., and Hirsch, P. B. 1960. The Dislocation Distribution, Flow Stress, and Stored Energy in Cold-worked Polycrystalline Silver. *Philosophical Magazine Series 8*, 5, 485-497.

Burke, J. E., and Turnbull, D. 1952. Recrystallization and Grain Growth. *Progress in Metal Physics*, 3. 220-292.

Byrne, J. G. 1965. *Recovery, Recrystallization, and Grain Growth*. New York: The Macmillan Company.

Cobo S. J., and Sellars C. M. 2001. Microstructural evolution of austenite under conditions simulating thin slab casting and hot direct rolling. *Ironmaking and Steelmaking*, 28(3), 230-236.

De Meyer, M., Vanderschueren, D., and De Cooman, B. C. 1999. The Influence of the Substitution of Si by Al on the Properties of Cold Rolled C-Mn-Si Trip Steels. *ISIJ International*, 39(8), 813-822.

Friedel, J. 1964. *Dislocations* (1st English ed. --.). Oxford; New York: Pergamon Press [U.S.A. ed. distributed by Addison-Wesley Pub. Co., Reading, Mass].

Gao, F., Xu, Y., Song, B., and Xia, K. 2000. Substructural Changes during Hot Deformation of an Fe-26Cr Ferritic Stainless Steel. *Metallurgical and Materials Transactions A*, A31, 21-27.

Gao, N., and Baker, T. N., 1998. Austenite grain growth behavior of microalloyed Al-V-N and Al-V-Ti-N steels. *ISIJ International*, 38(7), 744-751.

Glover, G., and Sellars, C. M. 1973. Recovery and Recrystallization during High Temperature Deformation of α -Iron. *Metallurgical Transactions*, 4, 765-775.

Gove, K. B., and Charles, J. A. 1974. The high-temperature hardness of various phases in steel. *Metals Technology*, 1, 279-283.

Gourdet, S., and Montheillet, F. 2000. An experimental study of the recrystallization mechanism during hot deformation of aluminum. *Materials Science and Engineering A*, A283, 274-288.

Harold, F., and Ashby, M. F. 1982. *Deformation-Mechanism Maps, the Plasticity and Creep of Metals and Ceramics*. Oxford, Pergamon Press.

Hu, H. 1962. Direct observations on the annealing of a Si-Fe Crystal in the Electron Microscope. *Transactions of the metallurgical society of AIME*, 224, 75.

Humphreys, F. J., and Hatherly, M. 2004. *Recrystallization and Related Annealing Phenomena Second Edition*. Boston, Elsevier Ltd.

Jacques, P. J., Girault, E., Mertens, A., Verlinden, B., van Humbeeck, J., and Delannay, F. 2001. The Developments of Cold-rolled TRIP-assisted Multiphase Steels. Al-Alloyed TRIP-assisted Multiphase Steels. *ISIJ International*, 41(9), 1068-1074.

Jonas, J. J., Sellars, C. M., and McG. Teart, W. J. 1969 Strength and structure under hot-working conditions. *Metallurgical Reviews*, 130, 1.

Karjalainen, L. P. 1995. Stress relaxation method for investigation of softening kinetics in hot deformation steels. *Materials Science Technology*, 11, 557-565.

Karjalainen, L. P., and Perttula, J. 1996. Characteristics of Static and Metadynamic Recrystallization and Strain Accumulation in Hot-deformed Austenite as Revealed by the Stress Relaxation Method. *ISIJ international*, 36(6), 729-736.

Kassner, M. E. 1989. Large-Strain Deformation of Aluminum Single Crystals at Elevated Temperature as a Test of the Geometric-Dynamic-Recrystallization Concept. *Metallurgical Transactions A*, 20, 2182-2185.

Kleber, S., and Sommitsch, C. 2004. Stress Relaxation Measurements of Meta-dynamic and Static Recrystallization of Alloy 80A. *Materials Science Forum*, 467-470, 1237-1242.

Klinkenberg, C., and Hensger, K.-E. 2005. Processing of Niobium Microalloyed API Grade Steel on a Thin Slab Plant. *Materials Science Forum*, 500-501, 253-260.

Klinkenberg, C., Bilgen, C., Boecher, T., and Schlüter, J. 2010. 20 Years of Experience in Thin Slab Casting and Rolling State of the Art and Future Developments. *Materials Science Forum*, 638-642. 3610-3615.

Kuhlmann-Wilsdorf, D. 2000. The Connection between Recovery and Glide Type in Aluminum and Al-Mg. *Materials Science Forum*, 331-337, 689-702.

Laasraoui, A., and Jonas, J. J. 1991. Recrystallization of Austenite after Deformation at High Temperatures and Strain Rates – Analysis and Modeling. *Metallurgical Transactions A*, 22A, 151-160.

Leslie, W. C. 1981. *The physical metallurgy of steel*. Washington: New York: Hemisphere Pub. Corp..

Li, J. C. M. 1962. Possibility of Subgrain Rotation during Recrystallization. *Journal of Applied Physics*, 33, 2958.

Li, G., Maccagno, T. M., Bai, D.Q., and Jonas, J. J. 1996. Effect of Initial Grain Size on the Static Recrystallization Kinetics of Nb Microalloyed steel. *ISIJ International*, 36(12) 1479-1485.

Liu, W. J. 2012. A Review of the Stress-relaxation Method for Following the Kinetics of Precipitation, Recovery, and Recrystallization. *Materials Science Forum*, 706-709, 2758-2763.

Liu, W. J., and Jonas, J. J. 1988. A Stress Relaxation Method for Following Carbonitride Precipitation in Austenite at Hot Working Temperature. *Metallurgical Transactions A*, 19A, 1403-1413.

Luo, H., Sietsma, J., and Van der Zwaag, S. 2004. A Metallurgical Interpretation of the Static Recrystallization Kinetics of an Intercritically Deformed C-Mn Steel. *Metallurgical and Materials Transaction A*, 35A, 1889-1898.

Luton, M. J., and Sellars, C. M. 1969. Dynamic Recrystallization in Nickel and Nickel-Iron Alloys during High Temperature Deformation. *Acta Metallurgica*, 17, 1033-1043.

Martínez-de-Guerenu, A., Arizti, F., Díaz-Fuentes, M., and Gutiérrez, I. 2004. Recovery during annealing in a cold rolled low carbon steel. Part I: Kinetics and microstructural characterization. *Acta Materialia*, 52, 3657-3664.

Martínez-de-Guerenu, A., Arizti, F., Díaz-Fuentes, M., and Gutiérrez, I. 2004. Recovery during annealing in a cold rolled low carbon steel. Part II: Modelling the kinetics. *Acta Materialia*, 52, 3665-3570.

Mehtonen, S. V., Karjalainen, L. P., and Porter, D. A. 2013. Hot deformation behavior and microstructure evolution of a stabilized high-Cr ferritic stainless steel. *Materials Science and Engineering A*, 571, 1-12.

Mehtonen, S., Karjalainen, P., and Porter, D. 2013. Effect of Hot Deformation Temperature on the Recrystallization Mechanisms and Texture in a High-Cr Ferritic Stainless Steel. *Material Science Forum*, 762, 705-710.

Mullar, J., Henning, W., and Bilgen, C. 2005. Advanced CSP casting technology for high-quality steels grades. *Proceedings of 33rd McMaster Symposium on Iron & Steelmaking, Hamilton, Ont., Canada, McMaster University*, 240-250.

Nagata, M. T., Speer, J. G., and Matlock, D. K. 2002. Titanium nitride precipitation behavior in thin-slab cast high-strength low-alloy steels. *Metallurgical and Materials Transactions A*, 33A, 3099-3110.

Nes, E. 1995. Recovery Revisited. *Acta Metallurgica et Materialia*, 43(6), 2189-2207.

Nes, E. 1998. Modeling of Work Hardening and Stress Saturation in FCC Metals. *Progress in Materials Science*, 41. 129-193.

Ouchi, C. and Okita, T. 1983. Dynamic Recovery and Static Recrystallization of 1.8% Al Steel in Hot deformation. *Transactions of the Iron and Steel Institution of Japan*, 23, 128-136.

Pettula, J. S., and Karjalainen, L. P. 1998. Recrystallization rates in austenite measured by double compression and stress relaxation methods. *Materials Science and Technology*, 14, 626-630.

Pottore N. S., Garcia, C. I., and DeArdo A. J. 1991. Interrupted and Isothermal Solidification Studies of Low and Medium Carbon Steels. *Metallurgical Transactions A*, 22A, 1871-1880.

Priestner, R., Microstructural Change during the Hot Working of As-Cast Austenite. *Materials Science Forum*, 284-286, 95-104.

Rodriguez-Ibabe, J. M. 2005. Thin Slab Direct Rolling of Microalloyed Steels. *Materials Science Forum*, 500-501, 49-62.

Rodriguez-Ibabe, J. M. 2007. *Thin Slab Direct Rolling of Microalloyed Steels*. Stafa-Zuerich, Trans Tech Publication Ltd.

Rosenberg, J. M., and Piehler, H. R. 1971. Calculation of the Taylor Factor and Lattice Rotations for Bcc Metals Deforming by Pencil Glide. *Metallurgical Transactions*, 2, 257-259.

Roucoules, C., Hodgson, P. D., Yue, S., and Jonas, J. J. 1994. Softening and Microstructural Change Following the Dynamic Recrystallization of Austenite. *Metallurgical and Materials Transactions A*, 25A, 389-400.

Samek, L. De Moor, E., Penning, J., and De Cooman, B. C. 2006. Influence of Alloying Elements on the Kinetics of Strain-Induced Martensitic Nucleation in Low-Alloy, Multiphase High Strength Steels. *Metallurgical and Materials Transactions A*, 37A, 109-123.

Sha, Q., and Sun, Z. 2009. Grain growth behavior of coarse-grained austenite in a Nb-V-Ti microalloyed steel. *Materials Science and Engineering A*, A523, 77-84.

Schmidt, C. G., Young, C. M., Walser, B., Klundt, R. H., and Sherby, O. D. 1982. The Influence of Substructure on the Elevated and Room Temperature Strength of a 26Cr-1Mo Ferritic Stainless Steel. *Metallurgical Transactions A*, 13A, 447-456.

Sellars, C. M., and Whiteman, J. A. 1979. Recrystallization and grain growth in hot rolling. *Metal Science*, 13(3-4), 187-194.

Sinclair, C. W., Mithieux, J.-D., Schumitt, J.-H., and Bréchet, Y. 2005. Recrystallization of Stabilized Ferritic Stainless Steel Sheet. *Metallurgical and Materials Transactions A*, 36A, 3205-3215.

Smith, A., Luo, H., Hanlon, D. N., Sietsma, J., and Van der Zwaag, S. 2004. Recovery Processes in the Ferrite Phase in C-Mn. *ISIJ international*, 44(7), 1188-1194.

Song, E. J., Suh, D.-W., and Bhadeshia, K. H. D. H. 2013. Theory for hydrogen desorption in ferritic steel. *Computational Materials Science*, 79, 36-44.

Speich, G. R. and Fisher, R. M. 1996. in Recrystallization, *Grain Growth and Textures*, ASM, Ohio, 563.

Suito, H., Ohta, H., and Morioka, 2006. Refinement of solidification microstructure and austenite grain by fine inclusion particles. *ISIJ International*, 46(6), 840-846.

Tsuji, N., Matsubara, Y., and Saito, Y. 1997. Dynamic recrystallization of Ferrite in Interstitial Free Steel. *Scripta Materialia*. 37(4). 477-484.

Tsuji, N., Matsubara, Y., Saito, Y., and Maki, T. 1998a. Occurrence of Dynamic Recrystallization in Ferritic Iron. *Journal of the Japan Institute of Metals*, 62(10), 967-976.

Tsuji, N., Shinmiya, T., Saito, Y., and Muraki, M. 1998b. Deformation Microstructure and Nucleation of Recrystallization in Hot-deformed Single Crystals of 18% Cr Ferritic Steel. *ISIJ International*, 38(4), 380-389.

Verdier, M., Brechet, Y., and Guyot, P. 1999. RECOVERY OF AlMg ALLOYS: FLOW STRESS AND STRAIN-HARDENING PROPERTIES. *Acta Materialia*, 47(1), 127-134.

Wang, R., Garcia, C. I., Hua, M., Zhang, H., and DeArdo, A. J. 2005. The Microstructure Evolution of Nb, Ti Complex Microalloyed Steel during the CSP Process. *Materials Science Forum*, 500-501, 229-236.

Yagi, H., Tsuji, N., and Saito, Y. 2000 Dynamic Recrystallization in 18% Cr Ferritic Steel. *Tetsu- to-Hagané*, 86(5), 349-356.

Yamagata, H. 1992a. Multipeak stress oscillations of five-nine-purity aluminum during a hot compression test. *Scripta Metallurgica et Materialia*, 27(2), 201-203.

Yamagata, H. 1992b. Dynamic recrystallization of single-crystalline aluminum during compression tests. *Scripta Metallurgica et Materialia*, 27(6), 727-732.

Yamagata, H. 1992c. Microstructural evolution of single-crystalline aluminum during multipeak stress oscillation at 623K. *Scripta Metallurgica et Materialia*, 27(9), 1157-1160.

Yamagata, H. 1994. In situ observation of dynamic recrystallization in five-nine aluminum by transmission Laue method. *Scripta Metallurgica et Materialia*, 27(6), 727-732.

Yanagida, A., and Yanagimoto, J. 2008. Formulation of softening fractions and related kinetics for static recrystallization using inverse analysis of double compression test. *Materials Science and Engineering A*, 487, 510-517.

Zener, C., and Hollomon, J. H. 1944. Effect of Strain Rate upon Plastic Flow of Steel. *Journal of Applied Physics*, 15, 22-32.

Zhou, T. H. 2010a. *Control of Microstructure during Solidification & Homogenization of Thin-Slab Cast Direct-Rolling (TSCDR) Microalloyed Steels*. Ph. D. theses McMaster University, Hamilton, ON., Canada.

Zhou, T., O'Malley, R. J., and Zurob H. S. 2010b. Study of Grain-Growth Kinetics in Delta-Ferrite and Austenite with Application to Thin-Slab Cast Direct-Rolling Microalloyed Steels. *Metallurgical and Materials Transactions A*, 41A, 2112-2120.

Zhou, T. H., Zurob, H. S., Essadiqi, E., and Voyzelle, B. 2011. Kinetics of Delta-Ferrite to Austenite Phase Transformation in a Two-Phase Fe-Al-C Alloy. *Metallurgical and Materials Transaction A*, 42A, 3349-3357.

Zhou, T. H., Gheribi, A. E., and Zurob, H. S. 2013. Austenite particle coarsening and delta-ferrite grain growth in model Fe-Al alloy. *Canadian Metallurgical Quarterly*, 52(1), 90-97.